SEMI-EMPIRICAL MODELING AND OPTIMIZATION OF METAL SPUTTERING PROCESSES

A THESIS SUBMITTED TO

THE GRADUATE SCHOOL OF NATURAL AND APPLIED SCIENCES

OF

MIDDLE EAST TECHNICAL UNIVERSITY

BY

ÖZGE ÇİMEN

IN PARTIAL FULFILLMENT OF THE REQUIREMENTS

FOR

THE DEGREE OF MASTER OF SCIENCE

IN

CHEMICAL ENGINEERING

JULY 2015

Approval of the thesis:

SEMI-EMPIRICAL MODELING AND OPTIMIZATION OF METAL SPUTTERING PROCESSES

submitted by **ÖZGE ÇİMEN** in partial fulfillment of the requirements for the degree of **Master of Science in Chemical Engineering Department, Middle East Technical University** by,

Prof. Dr. Gülbin Dural Ünver _____
Dean, Graduate School of **Natural and Applied Sciences**

Prof. Dr. Halil Kalıpçılar _____
Head of Department, **Chemical Engineering**

Assoc. Prof. Dr. Serkan Kıncal _____
Supervisor, **Chemical Engineering Dept., METU**

Examining Committee Members:

Prof. Dr. İnci Eroğlu _____
Chemical Engineering Dept., METU

Assoc. Prof. Dr. Serkan Kıncal _____
Chemical Engineering Dept., METU

Prof. Dr. Göknur Bayram _____
Chemical Engineering Dept., METU

Asst. Prof. Dr. Harun Koku _____
Chemical Engineering Dept., METU

Asst. Prof. Dr. Yılser Devrim _____
Energy Systems Engineering Dept., Atılım University

Date: 13.07.2015

I hereby declare that all information in this document has been obtained and presented in accordance with academic rules and ethical conduct. I also declare that, as required by these rules and conduct, I have fully cited and referenced all material and results that are not original to this work.

Name, Last name: Özge Çimen

Signature:

ABSTRACT

SEMI-EMPIRICAL MODELING AND OPTIMIZATION OF METAL SPUTTERING PROCESSES

Çimen, Özge

M.S, Department of Chemical Engineering

Supervisor: Assoc. Prof. Dr. Serkan Kıncal

July 2015, 121 pages

Continuous miniaturization of thin film based electronic devices is the major motivator for research in physical vapor deposition (PVD) applications especially in military and aerospace applications. The challenges in the good quality thin film is the requirement for good mechanical, optical and electrical properties and high thickness uniformity across wafer. In this study, the magnetron sputtering system was investigated which is a commonly used technique to deposit thin films. Deposition and heat transfer mechanism of this deposition system is the main focus of this thesis in which both modeling and experimental approaches were used.

In this study, a modeling approach was used to understand and characterize the operation conditions of the PVD system. A model was implemented to eliminate the geometrical factor to decrease the number of experiments. Using the theoretical knowledge and the findings from the model, experiments were designed for the operational conditions including sputtering power, argon flow and system pressure interactions. Produced thin films were evaluated by means of thickness, deposition

rate, resistivity and thickness uniformity. Then, a thermal model was described to estimate the substrate temperature during the sputtering and heating processes. Since plasma interactions create significant complexity in the model, experiments were designed to complete the modeling studies. The heater model includes detailed energy balances for conduction and radiation mechanisms. Thermal model for the sputtering process uses the energy balances for conduction mechanism and heat flux input obtained from the experiments. For the data analysis and design of experiments (DOE) study JMP software and for the modeling studies MATLAB and ANSYS tools were used.

Keywords: Thin film, PVD, magnetron sputtering, thermal modeling

ÖZ

METAL İLE SAÇTIRMA SÜREÇLERİNİN YARI AMPİRİK MODELLENMESİ VE OPTİMİZASYONU

Çimen, Özge

Yüksek Lisans, Kimya Mühendisliği Bölümü

Tez Yöneticisi: Doç. Dr. Serkan Kıncal

Temmuz 2015, 121 sayfa

Özellikle askeri ve havacılık uygulamalarında ince film tabanlı elektronik aygıtların sürekli küçülmesi, fiziksel buhar biriktirme (PVD) araştırmaları için önemli bir motivasyon olmuştur. İyi kalitede ince filmler üretebilmenin zorlukları üretilen filmin iyi mekanik, optik, elektriksel özelliklere ve kalınlık dağılımına sahip olması gerekliliğidir. Bu çalışma, ince film üretmek için yaygın olarak kullanılan bir teknik olan magnetron saçtırma sistemi üzerinedir. Bu çalışmanın ana hedefi olan sistemin biriktirme ve ısı aktarım mekanizmalarının anlaşılmasında, modelleme ve deneysel yaklaşımlar kullanılmıştır.

Bu çalışmada, PVD sisteminin çalışma koşullarını anlamak ve tanımlamak için modelleme yaklaşımı kullanılmıştır. Bu nedenle, modelleme deneylerinin sayısını azaltmak, böylece geometrik faktörleri ortadan kaldırmak için uygulanmaktadır. Teorik bilgi ve modelin bulguları kullanarak deneyler güç, argon akışı ve sistem basıncı etkileşimlerini içeren çalışma koşulları için tasarlanmıştır. Üretilen filmler kalınlık, biriktirme hızı, direnç ve kalınlık homojenliği açısından değerlendirilmiştir. Daha sonra, bir ısıl model, biriktirme ve ısıtma işlemleri

esnasında alt-taş sıcaklığını tahmin etmek için tasarlanmıştır. Plazma etkileşimleri modelleme açısından zor olması nedeniyle modelleme çalışmalarını tamamlamak üzere deneysel planlar tasarlanmıştır. Isıtıcı modeli iletim ve radyasyon mekanizmalarının detaylı enerji denkliklerini içermektedir. Biriktirme işlemi esnası için tanımlanan termal model enerji denkliklerinde iletim mekanizması ve deneylerden elde edilen ısı akışı bilgileri kullanılmıştır. Veri analizi ve deney tasarımı (DOE) çalışmaları için JMP yazılımı ve modelleme çalışmaları için MATLAB ve ANSYS programları kullanılmıştır.

Anahtar Kelimeler: İnce film, PVD, magnetron saçtırma, ısıl modelleme

To my family

ACKNOWLEDGEMENTS

First and foremost, I'm deeply grateful to my supervisor Dr. Serkan Kıncal. He provided me with an exciting thesis project that greatly enriched my skills in both experimental and theoretical research. Even the times that I make mistakes, he has always supported and helped me with his wisdom. I would also like to thank him for his great guidance and encouragements throughout my graduate years that I will always remember.

I would like to acknowledge ASELSAN for providing the financial support and experimental setup for this study. I would like to express my gratitude to Elif Apaydın and the rest of the "Thin Film Laboratory" team: Berkay Atabay, Reşat Tüzün, Türker Sarıtaş, İlay Akdoğan, Başar Bölükbaşı and Erkan Kök from ASELSAN for helping me with the experiments and supporting me with their valuable ideas all the time.

Since I have finished this study without a study group, my colleagues at this department become my study group through almost three years. I greatly appreciated the support of Cihan Ateş and Elif İrem Şenyurt for all contribution to finish this thesis and their friendship. I would like to thank Bilgenur Keskin for the support since we were undergraduate students at this department. Without Merve Özkutlu and Berrak Erkmen, C-building would be a tedious place to study. I am grateful to have them in METU and thanks for all the good times spent and will be spent together. Thanks for Burcu Şahin, Necip Berker Üner, Mustafa Yasin Aslan, Melis Kargılı, Elif Topçuoğlu, Dilara Çağlayan, Fatma Şahin for sharing their experiences and friendship through years.

I would like to extend my gratitude to my lovely friends Buse Altunay, Pınar Uz and Elif Altuntop for their endless friendship through all those years and their trust to me. I also want to thank Gencay Yıldız who became like a brother to me for his

patience during our long hours of conversations. Thanks to my friends Bahadır Aslandoğan, Halilcan Toksöz, Tuğçe Topaloğlu, Oğuz Tikenoğulları, Belinda Gökbulut, and all “Planlar Planlar” members for providing motivation in my life with many organizations.

I am also grateful for the endless love and unconditional support of my family. My deepest appreciation is to my brother Özgür Çimen. Without his help I would be lost during difficult times. Special thanks to my love Ahmet Boslu, standing right beside me and sharing my dreams for five years. I am happy to have you in my life and I heartily thank you for your great patience and love.

TABLE OF CONTENTS

ABSTRACT v

ÖZ vii

ACKNOWLEDGEMENTS x

TABLE OF CONTENTS xii

LIST OF TABLES xv

LIST OF FIGURES xvi

FIGURES xvi

NOMENCLATURE xix

CHAPTERS

1. INTRODUCTION 1

1.1 Objectives of the Study 1

1.2 Thin Film Properties and Application 2

1.3 Thin Film Production Line 3

1.3.1 Surface Preparation 4

1.3.2 Thin Film Deposition 5

1.3.2.1 Chemical Vapor Deposition 6

1.3.2.2 Physical Vapor Deposition 7

1.3.3 Film Patterning 10

1.4 Magnetron sputtering 13

1.4.1 Film Growth Process 15

2. EXPERIMENTAL 19

2.1 Experimental Setup 19
2.2 Experimental Procedure 21
2.3 Thickness Characterization 24
2.4 Resistivity Characterization 25
2.4.1 Resistivity Model 26
2.4.2 Resistivity Experiments 27
2.4.3 Resistivity Model Fitting 28
2.5 Temperature Characterization 31
3. MODELING 33
3.1 Theoretical Modeling 33
3.1.1 Flux Model 34
3.1.2 Thermal Model 37
3.1.2.1 ANSYS Model 38
3.1.2.2 MATLAB Model 45
3.2 Empirical Modeling 49
3.2.1 Experimental Design Approach- Model Based Design-How to Eliminate Geometrical Factors 49
3.2.1.1 Effect of Geometrical Factors 52
3.2.2 Experimental Plan 55
3.2.2.1 Flux Model Experimental Plan 56
3.2.2.2 Thermal Model Experimental Plan 59
4. RESULTS AND DISCUSSION 64
4.1 Empirical Modeling 64
4.1.1 Target 1 Results 64
4.1.2 Target 2 Results 70

4.1.3 Stationary Substrate Experiments 76
4.1.4 Thermal Analysis-Substrate Temperature Measurements..... 78
4.2 Modeling Results..... 80
4.2.1 Flux Model 80
4.2.1.1 Target 1 Modeling Results 80
4.2.1.2 Target 2 Modeling Results 83
4.2.2 Thermal Model 87
4.2.2.1 ANSYS Heater Results 87
4.2.2.2 MATLAB Dynamic Simulation Results 90
5. CONCLUSION AND FUTURE WORK..... 91
5.1 Conclusion..... 91
5.2 Future Work 92
REFERENCES..... 93
APPENDICES
A. MATLAB CODES 97
A.1 Flux Model M-Files..... 97
A.1.1 Main Program..... 97
A.1.2 Function Flux..... 100
A.2 Thermal Dynamic Model M-Files..... 100
A.2.1 Main Program..... 100
A.2.2 Function qflux 102
B. OUTPUT OF ANSYS SIMULATIONS 103
B.1 Large Heater Result 103
B.2 Small Heater Results..... 112

LIST OF TABLES

TABLES

Table 1.1 Material characteristics of thin films. 2
Table 2.1 Recipe parameters 22
Table 2.2 Deposition parameters for sputtered thin films 23
Table 2.3 Runcard of resistivity characterization experiments. 27
Table 2.4 Literature and fitted data for resistivity characterization of Cu. 30
Table 3.1 Material data of the parts 41
Table 3.2 Energy balance terms for the representative nodes. 48
Table 3.3 Simulation factors and levels. 50
Table 3.4 Sputtering process factors and responses. 55
Table 3.5 Target 1 experimental plan (DOE1). 56
Table 3.6 Target 2 experimental plan (DOE2). 58
Table 3.7 Runcard of stationary substrate experiments. 59
Table 3.8 Experimental conditions for the substrate temperature characterization during sputtering process. 60
Table 3.9 Experimental conditions for the substrate temperature characterization during heating process. 60
Table 4.1 Parameter estimates - Growth rate 67
Table 4.2 Parameter Estimates - % Standard deviation 68
Table 4.3 Parameter estimates - Growth rate. 73
Table 4.4 Parameter estimates- % standard deviation. 74
Table 4.6 Results of substrate surface temperature experiments. 79
Table 4.7 MATLAB Simulation parameters and outputs for target 1 83
Table 4.8 MATLAB Simulation parameters and outputs for target 2. 85
Table 4.9 Surface temperature of small heaters. 89
Table 4.10 Surface temperatures of large heaters. 90

LIST OF FIGURES

FIGURES

Figure 1.1 Thin film production line process steps. 4
Figure 1.2 Outline of deposition methods of thin films. 5
Figure 1.3 CVD reaction chamber..... 6
Figure 1.4 Sputtering of atoms from a target due to energetic particles 8
Figure 1.5 Typical DC sputtering system..... 8
Figure 1.6 RF sputter deposition system. 9
Figure 1.7 Photolithography process steps..... 11
Figure 1.8 Plating process steps. 13
Figure 1.9 Magnetic field lines of magnetron sputtering 14
Figure 1.10 Representation of magnetron sputtering system 14
Figure 2.1 Multi-source magnetron sputtering equipment..... 20
Figure 2.2 Magnetron, substrate and target arrangement in the system..... 21
Figure 2.3 Mask design for the stylus profiler measurements. 24
Figure 2.4 Coated alumina substrate and metal mask with patterns. 25
Figure 2.5 Four point probe system..... 28
Figure 2.6 Change in thickness of the films as a function of number of pass..... 29
Figure 2.7 Change in resistivity of the films as a function of number of pass..... 29
Figure 2.8 Comparison of experimental and modeled sheet resistivity with respect to thickness for Cu thin films. 30
Figure 2.9 Thermocouple distribution for the temperature characterization experiments and the real setup. 31
Figure 3.1 Surface fluxes in physical vapor deposition systems used in simulation models 34
Figure 3.2 Target-substrate configuration. 35
Figure 3.3 MATLAB flux distribution code sequence..... 37

Figure 3.4 Schematic drawing of magnetron sputtering system. 39
Figure 3.5 Exterior view of the system for large heater-substrate model. 41
Figure 3.6 Geometry of the system revealing the large heater geometry and parabolic reflector. 42
Figure 3.7 The boundary conditions for large heater system. 42
Figure 3.8 Exterior view of the system for small heater-substrate model..... 43
Figure 3.9 Geometry of the system revealing the small heater geometry. 43
Figure 3.10 The boundary conditions for small heater system. 44
Figure 3.11 Representative node distribution. 48
Figure 3.12 Variation of simulation time and average deposition with respect to mesh size at 30 mm target to substrate separation. 52
Figure 3.13 Effect of target-to-substrate separation and movement limit on thickness uniformity, target usage and deposition rate for target 1. 54
Figure 3.14 Effect of target-to-substrate separation and movement limit on thickness uniformity, target usage and deposition rate for target 2. 54
Figure 3.15 Typical power (%) input profile for the heater characterization experiments. 61
Figure 4.1 Thickness and resistivity profile for DOE1-Run3 64
Figure 4.2 Change of growth rate (nm/pass) of films sputtered with large Cu target for different experimental conditions 65
Figure 4.3 %Standard deviation of films sputtered with large Cu target for different experimental conditions..... 66
Figure 4.4 Actual by predicted plot of mean growth rate for large Cu target 67
Figure 4.5 Actual by predicted plot of % standard deviation for large Cu target 68
Figure 4.6 Prediction profiler to estimate the mean thickness and % standard deviation for films sputtered with large Cu targets 69
Figure 4.7 Thickness and resistivity profile for DOE2-Run1. 71
Figure 4.8 Change of growth rate (nm/pass) of films sputtered with target 2 for different experimental conditions..... 71
Figure 4.9 Change of percent standard deviation of thickness of the films. 72
Figure 4.10 Actual by predicted plot of mean growth rate (nm/pass) for the films sputtered with target 2. 73

Figure 4.11 Actual by predicted plot of %standard deviation for target 2. 74
Figure 4.12 Prediction profiler to estimate the mean thickness and % standard deviation for films sputtered with target 2. 75
Figure 4.13 Thickness profile for films coated with target 1 at baseline conditions 76
Figure 4.14 Thickness profile for the films coated with target 2 at baseline conditions. 77
Figure 4.15 Race track formation on the target 1 (left) and target 2 (right) surface. 77
Figure 4.16 Temperature profile during deposition under target 1 at baseline conditions. 78
Figure 4.17 Temperature profile during deposition under target 2 at baseline conditions. 79
Figure 4.18 Static flux distribution from the target 1. 81
Figure 4.19 Comparison of normalized experimental and MATLAB thickness distribution..... 81
Figure 4.20 Predicted contour plot for the deposition under target 1. 82
Figure 4.21 Static flux distribution from the target 2. 84
Figure 4.22 Predicted contour plot for the deposition under target 2. 84
Figure 4.23 Comparison of normalized experimental thickness with model predictions for target 1. 86
Figure 4.24 Comparison of normalized experimental thickness with model predictions for target 2. 86
Figure 4.25 ANSYS vs experiments (small heaters). 87
Figure 4.26 ANSYS vs experiments (large heater 1). 88
Figure 4.27 ANSYS vs experiments (large heater 6). 88
Figure 4.28 MATLAB vs experiments. 90

NOMENCLATURE

Symbols

A	Area (cm^2)
C_p	Heat Capacity (J/kg.K)
k	Thermal Conductivity (W/m.K)
P	Pressure (mTorr)
q"	Heat Flux (W/cm^2)
T	Temperature (°C)
t	Time (s)
V	Volume (cm^3)

Abbreviations

Ar	Argon
Au	Gold
BL	Baseline
Cu	Copper
CVD	Chemical Vapor Deposition
DC	Direct Current
DOE	Design of Experiment
DOE1	Design of Experiment Target 1

DOE2	Design of Experiment Target 2
MEMS	Micro Electro Mechanical Systems
PVD	Physical Vapor Deposition
RF	Radio Frequency
UV	Ultraviolet

Greek Letters

ε	Emissivity
σ	Stefan-Boltzmann Constant
α	Absorptivity
ρ	Density (kg/m^3)
ρ_0	Bulk Resistivity ($\mu\Omega.cm$)

Subscripts

i	Surface i
j	surface j
s	Substrate
t	Target

CHAPTER 1

INTRODUCTION

1.1 Objectives of the Study

Thin film production facility is an emerging facility at ASELSAN. Development of the deposition process in this production line is the main focus of this study. Therefore this research was conducted by financial support from and in collaboration with ASELSAN. Among the possible deposition techniques to manufacture required products, magnetron sputtering is chosen. The reason to choose magnetron sputtering equipment is that it is not only suitable for the fabrication of metal thin films but is also easy to achieve high deposition rates and can be used for large area applications. The objective of this study is by means of modeling and experiments to find out how DC magnetron sputtering deposition system parameters influence the uniformity, and growth rate of thin films and to characterize the thermal behavior of the substrate surface. Eventually combining modeling and experimental results develop a suitable process to achieve a qualified thin films with the requisite properties. For the characterization and optimization purposes, Copper (Cu) targets were chosen by considering its lower cost and high sputtering rate.

1.2 Thin Film Properties and Application

Thin films are very thin coatings in which thickness varies nanometers to a few micrometers. Thin film technology has been used for long time in plenty of applications such as microelectronic integrated circuits, magnetic information storage systems, optical coatings, wear resistant coatings and corrosion resistant coatings [1]. Although, the technology has been used for decades, there is growing research activity in this field since it is still an evolving technology with new applications, materials and deposition processes [2].

The challenges in the manufacture of good quality thin film is the requirement for good mechanical, thermal, optical, chemical and electrical properties. Each application requires different material properties so the deposition method of the films are chosen considering these properties. The main properties of the thin films can be summarized as in Table 1.1 [3].

Table 1.1 Material characteristics of thin films.

Electrical	Conductivity Resistivity Dielectric constant Dielectric loss
Thermal	Coefficient of expansion Thermal conductivity Temperature Variation of all properties
Mechanical	Intrinsic, residual and composite stress Adhesion Hardness Density
Morphology	Crystalline or amorphous Structural defect density Conformity / step coverage

Table 1.1 (continued)

Optical	Refractive index Absorption
Chemical	Composition Impurities Etch Rate Reactivity

The properties of the deposited film are affected by four main factors, which are substrate surface conditions, deposition system and conditions, film growth process on the substrate surface and the reactions and processes from the deposition.

Among these parameters, the major interest of this study is the effects of the choice deposition system and the process conditions on the thickness, deposition rate and thickness uniformity of the films. Properties of the thin films will be characterized by using resistivity and thickness measurements. Details of these characterizations will be described in Chapter 2.

1.3 Thin Film Production Line

The production line starts with substrate preparation. Then, thin film layers are deposited on the substrate by means of the chosen deposition process. It is followed by photo resist coating and pattern transfer with UV exposure. After this, development process is carried out to remove remaining photoresist. Finally with etching and striping processes the production of one layer ends and these operations are repeated for many times for complex circuit applications. The microelectronic production line sequence is shown in Figure 1.1. In this section thin film production steps will be briefly summarized while focusing on the thin film deposition processes and primarily sputtering deposition.

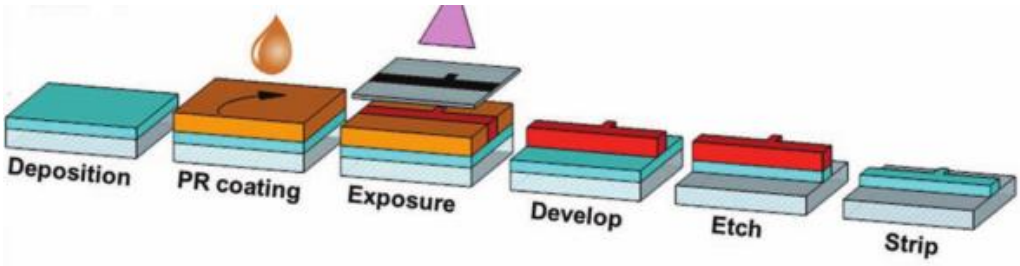

Figure 1.1 Thin film production line process steps [4].

1.3.1 Surface Preparation

Thin films and devices are created on surfaces called substrates or wafers. The stability of the products depend on the condition of the substrate surfaces. Thus, surfaces are generally treated prior to deposition processes in order to satisfy the necessary conditions. The mechanical, morphological and chemical properties of the wafers are crucial for adhesion, film growth and final coating. Therefore, depending on the applications, wafers are cleaned or changed by means of chemicals, mechanical systems and thermal processes. The aim of the cleaning is removing the contaminants and residue from the substrate surfaces. Smoothing the surface in order to obtain more dense coatings, roughening surfaces to increase adhesion of films and ion implantation to reduce the fracturing of wafers under load are the common methods used for surface modification purposes [5].

The full cleaning procedure of the wafers includes three steps which are removal of organic contaminants, thin oxide layer and ionic contamination. If the only source of contamination is organic material, O_2 plasma cleaning is sufficient. Submerging the substrates in heated mixtures of HCl or HF with DI water for 10 minutes is the commonly used cleaning method. Then wafers are rinsed with DI water, and dried with N_2 gas [6].

1.3.2 Thin Film Deposition

Thin film deposition methods can be divided into two main categories; chemical vapor deposition (CVD) and physical vapor deposition (PVD) and the methods are summarized in Figure 1.2.

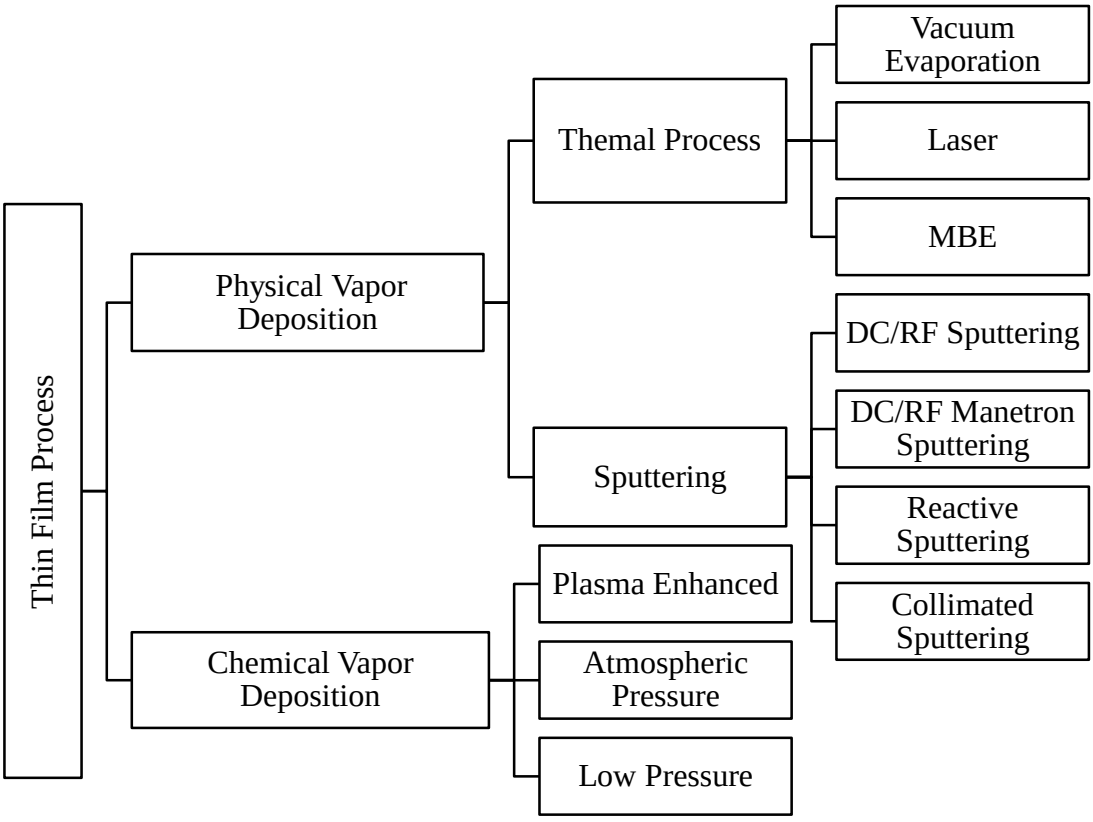

Figure 1.2 Outline of deposition methods of thin films [7 - 9].

This section aims to give general information about thin film deposition methods.

1.3.2.1 Chemical Vapor Deposition

A simple thermal CVD process consists of several steps. Firstly, precursor gas is introduced to the deposition chamber, and these gases react to form other compounds, then these compounds are transferred to the surface of the substrate. On substrate, surface reactions and desorption of gaseous by-products occur and finally these gases are removed from the reactor and deposition process is completed [8]. The schematic of a commonly used CVD reaction chamber is shown in Figure 1.3.

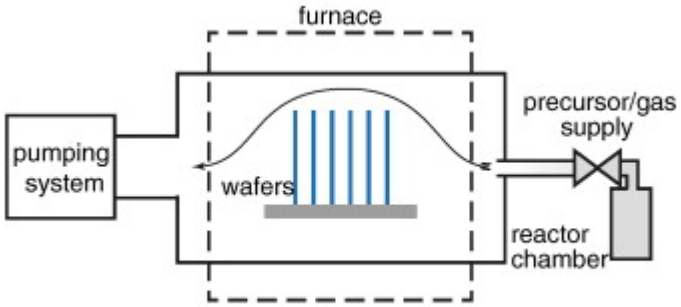

Figure 1.3 CVD reaction chamber [9].

The CVD method is used in the production of high-end goods like solid state electronic device, rocket engines, nuclear reactor components and for numerous applications. Use of CVD process enables to produce films with different stoichiometry with low equipment cost and operating expenses, moreover, the method can be used to produce various coating of metals semiconductor and compounds [10]. Besides the advantages, CVD has a number of disadvantages, as by-products of the processes can be dangerous and the cost of come precursors are highly expensive.

The major disadvantage of this method is the need for the high temperature to deposit films. In order to eliminate the need for high temperature, CVD methods are supported by different techniques as in the case of plasma enhanced chemical vapor deposition (PECVD). Use of ion bombardment decreases the need for elevated temperatures.

Atmospheric pressure CVD (APCVD), low pressure CVD (LPCVD) are the other CVD methods used commonly [8].

1.3.2.2 Physical Vapor Deposition

The main difference between CVD and PVD processes is that CVD processes involving chemical reactions to produce thin films, however, in PVD processes materials are vaporized from a solid or molten target, and deposited on the substrate [11]. Unlike to CVD processes PVD processes do not need elevated temperatures so that they can be used to deposit wide variety of materials like metals, ceramics, alloys and polymers on to different type of substrates. Moreover, dangerous chemicals are eliminated with this method. This makes PVD processes attractive for many industries, especially in microelectronic industry. As circuits are miniaturized continuously, there is always need to improve the PVD processes [12]. There are many type of PVD processes as shown in Figure 1.2, thermal processes and sputtering are the two main category of PVD techniques. However, main focus of this study is the magnetron sputtering, therefore, the following parts will be dedicated to the sputtering processes.

In a typical DC sputter system an inert gas is fed into the sputtering chamber at a regulated flow rate, commonly at low pressure. Then, plasma is formed by applying voltage across anode and cathode. The plasma contains neutral atoms, positive ions, neutrons, photons and free electrons. Sputtering of these atoms from the surface of the target is represented in Figure 1.4. Target material is placed on the cathode and the substrates are placed on the anode. The positive ions in the plasma are accelerated towards the target. These energetic ions dislodge the target atoms and these target atoms create a flux. The substrate is placed in the path of this flux and film deposition is achieved. Schematic representation of a direct current (DC) sputtering system is demonstrated in Figure 1.5. The process occur in a vacuum environment.

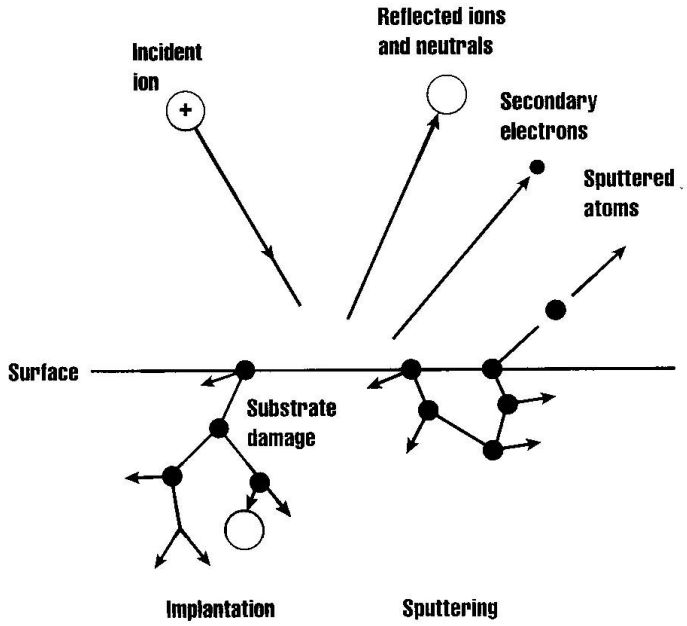

Figure 1.4 Sputtering of atoms from a target due to energetic particles [11].

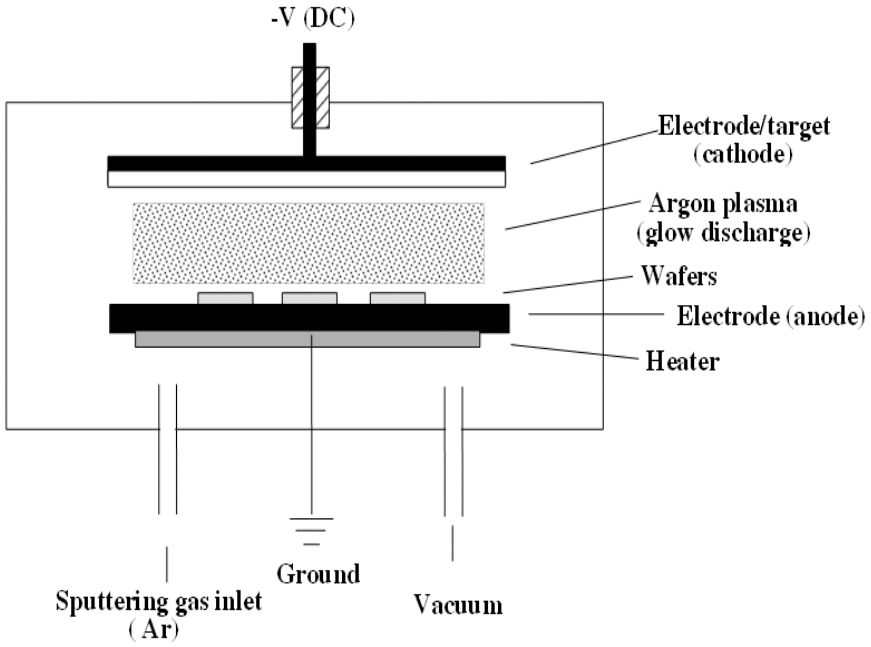

Figure 1.5 Typical DC sputtering system [11].

The DC sputtering method has several advantages including coating of large areas uniformly, high target utilization compared to other sputtering methods on the other hand low sputtering rate is the main disadvantage of those systems [5].

DC sputtering methods are used for conductive materials, however, sputtering of insulating material is also essential in many applications. If an insulating material is sputtered with a DC sputtering system, positive charges accumulate on the target surface and plasma cannot sustain. Therefore, alternating potential can eliminate the charge buildup on target so that radio frequency (RF) sputtering method is used. Since electrons increases their energy by this alternating RF field, secondary electrons to sustain plasma is not necessary for this systems that allows sputtering at lower pressures. In order to sustain the plasma a frequency above 1MHz is necessary and generally 13.56 MHz is used. The issues that need to be considered while sputtering with the RF systems is that target materials have low thermal conductivity, high thermal expansion and brittle structure. This can lead to high temperature gradients inside the target. Therefore, using higher power rates causes failure of the target. Since lower power rates are used, it takes long time get insulating films [11].

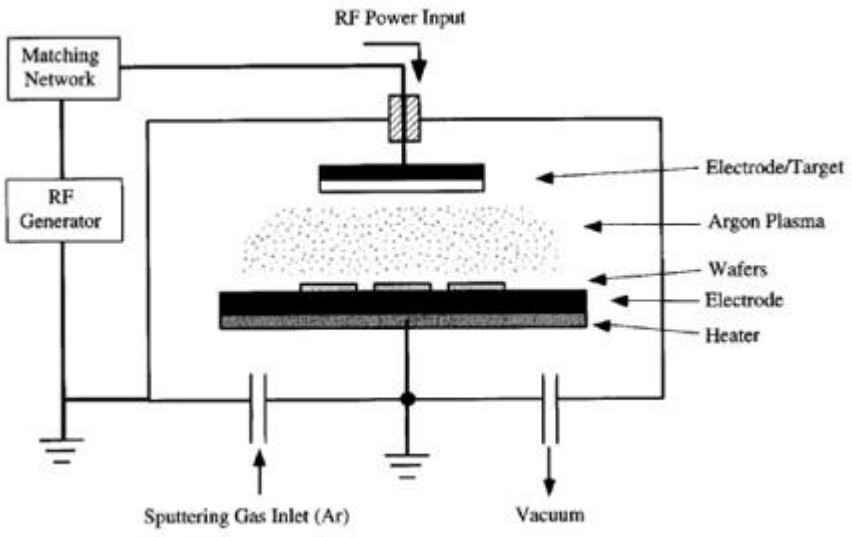

Figure 1.6 RF sputter deposition system [11].

In reactive sputtering, as in the process of CVD, sputtering occurs in the existence of a reactive gas like oxygen, nitrogen. This gas reacts with the sputtered atoms and creates compounds and deposit on to the wafer. In addition to the typical DC sputtering system, reactive sputter system includes reactive gas inlet to the system. For decades, reactive sputtering was used in the production of Tantalum Nitride (TaN) films for hybrid circuits and for micro electro mechanical systems (MEMS) [13]. In the reactive deposition of materials, the control of pressure of reactive gas is extremely important. Because higher reactive gas pressures result in target poisoning and low sputtering rates and low pressures causes improper film stoichiometry. Thus, there is a complex relationship between film composition and reactive gas pressure in reactive sputtering systems [14].

1.3.3 Film Patterning

In thin film coating step, geometrical consideration of the film was the thickness and uniformity of the deposited film, however, circuits involve parts like conductors, capacitors and insulators with very small feature sizes and these devices are created in the patterning (lithography) process. Therefore, deposition steps are critical since whole structure is built on these deposited layers. There is a direct relation between the difficulty of the patterning process and the feature size of the parts. Lithography process involves four steps which are resist coating, UV exposure under a mask, etching and developing and these steps are applied after the thin film deposition process is completed [10].

Firstly, film deposited wafers are spin-coated with the photoresist with a thickness of less than 1μm and this is followed by the exposure process. The UV exposure step is done with the help of a specially designed mask that contains the desired pattern. The pattern on the mask designates the zones that are opaque and transparent. Masks contain the pattern of the devices and commonly manufactured from Cr and FeO deposited film on glass substrates. The reason to use masks is that photoresists are the

chemicals that undergo changes after exposed to light. There are two type of photoresists called negative and positive. In positive photoresist, the regions exposed to light results in under scission of polymerized chains, this means exposed regions become soluble in the developer chemical. On the other hand, in negative resist, exposed patterns stay strong until the developing and etching processes are completed. Desired pattern is transferred to the photoresist after development which causes the partial removal of the photoresist. The lithography process is summarized in Figure 1.7. Thus, the aim of the photoresist is to resist etching during the transfer of pattern to the deposited film [10], [15].

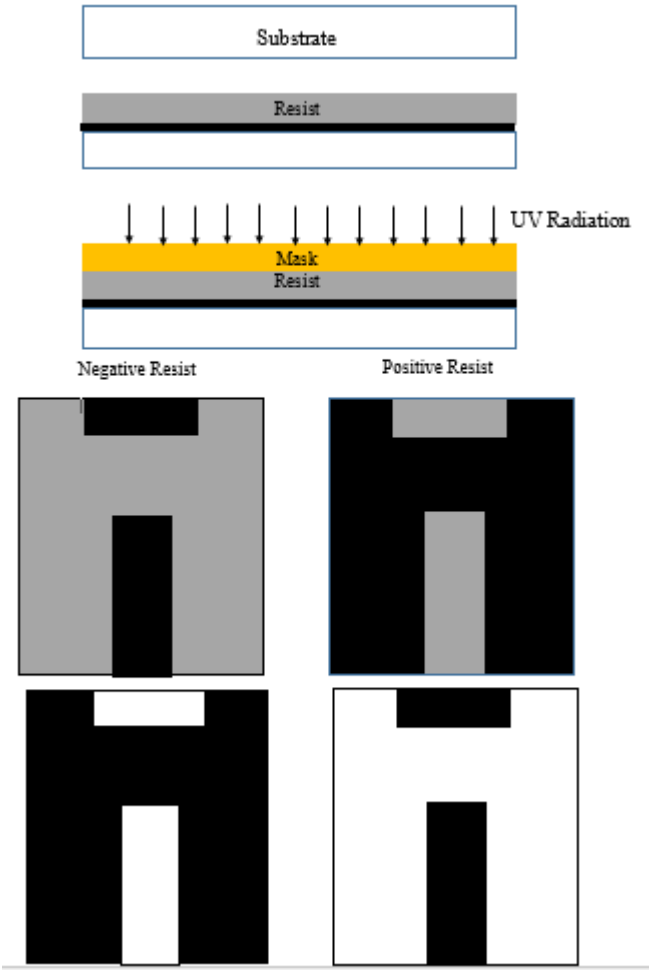

Figure 1.7 Photolithography process steps.

After exposure and development steps, substrate is etched by using special chemicals in order to transfer the pattern to the deposited film. The regions not protected by the resist are dissolved by the chemical etchants. Although, the etchants are designed to attack unprotected regions, there is also lateral removal of the films. The reduction in the etching resolution causes problems with small features. For this purpose for some processes dry etching is preferred, because its directionality is good for the features. However, poor etch selectivity is the main disadvantage of the dry etch. In order to solve the selectivity problem, reactive ion etching is used for many industries. The properties of the photoresist are very important for the success of the etching process. The thickness of the resist is determined by considering the coating thickness and etch selectivity. Ideally, the desired photoresist shape to define patterns is vertical walls [15].

At the end of the etching process, the pattern is transferred to the thin film under photoresist. There is a need for final step called striping that removes the remaining resist and finishes the patterning process [10].

The additive patterning process is called electroplating. Before going into electroplating process, there is a need for a seed layer. This seed layer is mainly deposited by using the thin film deposition methods. As in the case of lithography, electroplating also uses masking materials to transfer the pattern to the thin film. Thus, after the deposition of seed layer, mask material deposited and patterned on the film. Then, desired metal is plated up and masking material removed [6]. This process scheme is shown in Figure 1.8.

.

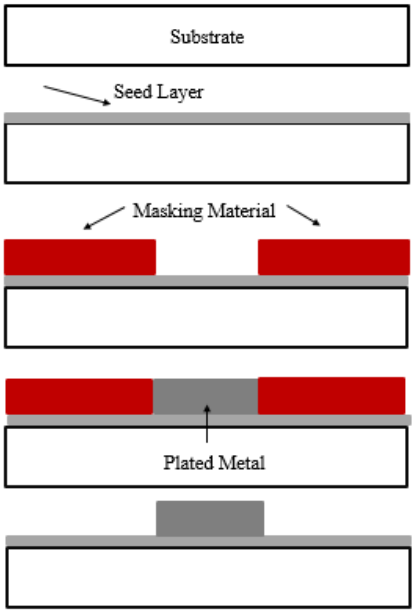

Figure 1.8 Plating process steps.

Electroplating process involves the reduction of metal ions from aqueous organic or fused-salt electrolytes. Deposition process is carried out in a bath that contains metal salt, wetting agent, weak acid, complexing agent, salt, brightener and leveler. Electroplated metal properties highly dependent on the bath composition (e.g., concentration of ions, type of additives, pH), also the process parameters (e.g., bath temperature, current), pattern of the devices and characteristics of wafer. Therefore, bath composition must be checked periodically [16].

1.4 Magnetron sputtering

Magnetron sputtering is a technique in which magnets from rare earth elements are used to trap electrons near the surface. This is provided by the magnetic field lines created by the magnets. After the dislocation of electrons from the source material, electric field accelerates these electrons to move towards the anode, in addition to the electric fields, presence of magnetic fields causes electrons to make spiral movements

around the target which is demonstrated in Figure 1.9 and magnetron sputtering system is represented in Figure 1.10. Since displaced electrons stay in proximity of the wafer, plasma can sustain at lower pressures. Due to this condition, collision probability decreases, higher sputtering rates at low powers are achieved [5].

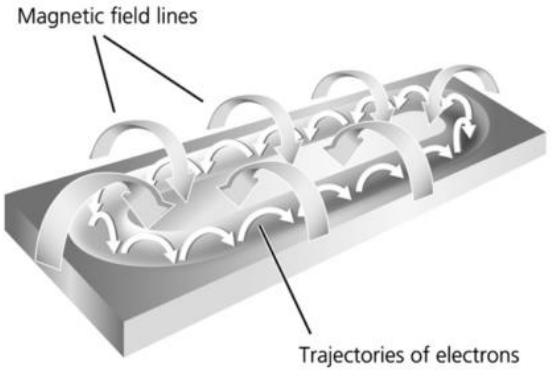

Figure 1.9 Magnetic field lines of magnetron sputtering [17].

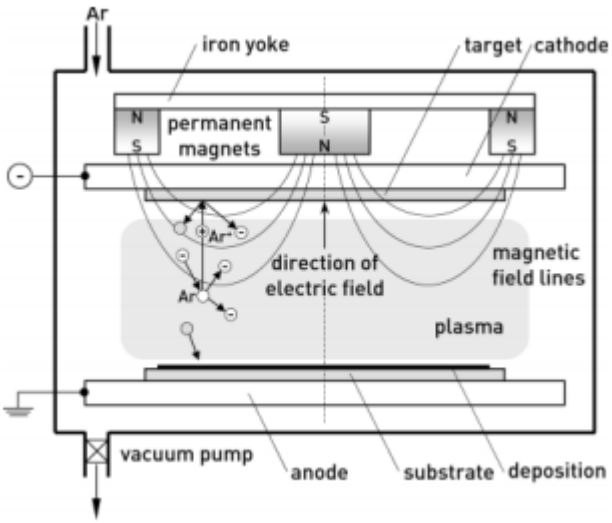

Figure 1.10 Representation of magnetron sputtering system.

In addition to this significance of using magnets, there are many advantages of magnetron sputtering among other sputtering methods which can be summarized as followed [17], [18];

- Lower substrate temperatures
- Improved adhesion of films on substrates
- Sputtering of variety of materials
- Higher sputtering rates
- Relatively stable processes
- Integration to large area applications
- Better uniformity in films
- Adjustable film properties

1.4.1 Film Growth Process

The film growth process starts with the transportation of atoms ejected from the target surface to the substrate surface, then these atoms are adsorbed on the wafer surface and diffused over the surface and involved in the film structure. Growth process is finished by the transportation of these atoms to their last location by bulk diffusion mechanism. The film growth process plays an important role on the final quality of the sputtered film so the parameters that affect this process need to be taken into consideration. Sputtering mechanism, sputtering gas pressure and the substrate temperature are the most important factors, in addition to these factors substrate surface morphology, target material, magnetic field, cathode bias are also a crucial factor that affect the film properties [5,19,20].

In order to have stable and controlled film structures, magnetron sputtering deposition conditions must be known and controlled properly. These important parameters are;

- System geometry
- Sputtering rate

- Gas pressure
- Sputtering target voltage/power
- Sputtering plasma uniformity
- Substrate temperature

Some of the factors like gas pressure, power can be tracked instantaneously, and however some parameters cannot be tracked that easy like plasma uniformity. First of all, a magnetron sputtering system must have proper vacuum. Contamination in the chamber and inadequate vacuum level directly affect coating. Then, effect of important parameters on the properties of the thin films can be examined.

Determination of substrate temperature distribution and characterization of film thickness by using resistivity of the films are critical part of this study. Therefore, effect of power, argon flow rate and pressure on resistivity, substrate temperature and growth rate are given in detail in following parts.

Film Resistivity

Grain size of the films are affected from the gas pressure. Chan et al. states in their experimental study that grain size increases with decreasing pressure. They explain this by decrease in collision probability of adsorbed atoms (adatoms) at low pressure levels. Decrease in collisions leads to increase in the movement of these atoms and bulk diffusion so crystallinity of the films increases. Improved crystalline structure also decreases the resistivity of the films, therefore there is an inverse relation between resistivity and working gas pressure [21].

Substrate temperature also affects electrical and structural properties of the sputtered films. Tou et al. performed experiments at different thicknesses and substrate temperatures and observed the effects on grain size and resistivity. They found out that substrate temperature improves the surface and bulk diffusion of atoms therefore increases the grain size and decreases the resistivity of the films. However, for

relatively thick films, substrate temperature was not effective on grain size significantly [22]. According to the study of Beaulieu et al. grain size decreases with increasing sputtering rate, target-to-substrate distance and gas flow rate, therefore resistivity decreases [23]. In their study Lee et al. investigate the effect of sputtering power on resistivity and they found out that there is inverse relation between resistivity and power as shown in [24].

Substrate Temperature

Substrate temperature is also an important parameter that influences the film properties. As in the case of resistivity, working gas pressure, deposition time and sputtering power affects the substrate temperature. In their study Krishnasamy et al. performed experiments by changing these factors at different levels. They found that sputtering power increases substrate temperature since increasing power causes increase in the number of energetic atoms that strike to wafer surface. Increase in deposition time also causes continuous striking of atoms to the surface so that substrate temperature increases. They also stated that working gas pressure increases the substrate temperature significantly and explained that increasing the gas pressure causes decrease in discharge voltage and increase in discharge current, which leads to increase in flux density so that the temperature increases [25].

Growth Rate

Growth rate is also an important parameter that is affected by operational and geometrical parameters of the system. Operational parameters are power, pressure, and substrate temperature and argon flow rate. For the deposition system used in this study, substrate is moving under the target so that geometrical parameters are substrate speed, substrate movement limit and the distance between target and substrate. In their article Chan et al. showed that as expected thickness of the films increases with the deposition time [26]. They explained the relation between power and growth rate by performing

experiments in which the argon pressure and deposition time were fixed and only changing parameter was sputtering power. Since increasing power causes increase in the number of energetic atoms that strike to wafer surface, film thickness is directly proportional to power. Chan et al. also investigated the influence of argon pressure on copper thin films and they found out that show that the lateral size of the Cu grains inversely proportional to Ar pressure. They explained that mobility of the Cu adatoms decrease in the surface due to increased collisions and number of collisions increases by increase in Ar flow rate. Moreover, low mobility Cu atoms on the growing film at higher working gas pressures decrease the probability of formation of large grain structure with high film crystallinity [27]. So that one should use high sputtering power with a low argon pressure for a copper thin film with low resistivity.

CHAPTER 2

EXPERIMENTAL

2.1 Experimental Setup

Within the scope of this research, a custom designed multi-source magnetron sputtering tool is used. Experimental setup is demonstrated in Figure 2.1. The sputtering takes place in a single vacuum chamber and there is a separate load-lock mechanism. Moreover, there is separate pumping systems to evacuate chamber and load–lock part. Having a load-lock mechanism with separate pumping system allows the transfer of substrates in an out of the deposition chamber without breaking vacuum of the chamber. It is important because the pressure in the chamber is less than 10^{-6} Torr and reaching over such low pressure takes long time for a big chamber like this. The system has five rectangular cathodes with the capabilities of DC and RF magnetron sputtering that allows the multilayer depositions. Moreover, substrate movement in the direction perpendicular to the long axis of the target is possible. Also, substrate heating before and during the experiments is possible through heaters between the sources. There are two size of heaters used in the system, large heaters are used to heat substrate prior to deposition and small heaters are used to minimize heat loss while substrate is oscillating under the target. Substrates used in this system can be 4 and 6 inch alumina wafers.

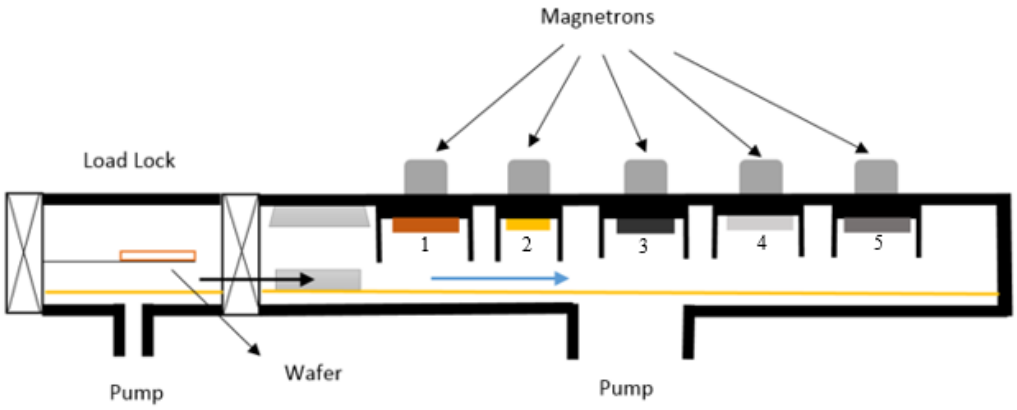

Figure 2.1 Multi-source magnetron sputtering equipment.

Although there are 5 sputtering magnetrons available in the system, in this study all films for this research were deposited with this DC magnetron sputtering system using copper (Cu) rectangular targets with the size of 125mm x 250mm (Target 1) and 75mm x 125mm (Target 2). Target 2 is designed to sputter gold (Au) material, so that all targets have the same dimensions except target 2. Au is a precious metal used in many metal sputtering processes therefore using smaller target for Au material was important to minimize the Au target cost and material lost during processes and experiments. For this reason, in order to minimize experimental cost with gold material, Cu target with the same size of the target 2 was used to predict behavior of the Au target. Working gas was Argon (Ar) for all the experiments, and Ar is fed to the system by using a tubing system resembles to shower head. Since argon was available on the vicinity of the substrate, this increase the probability of collisions. During deposition, substrate oscillates under the target to ensure uniformity on large substrate. Besides, the distance between target and substrate is an adjustable parameter for this system and also an optimization parameter for a sputtering process. Magnetron, target and substrate arrangement is shown in Figure 2.2.

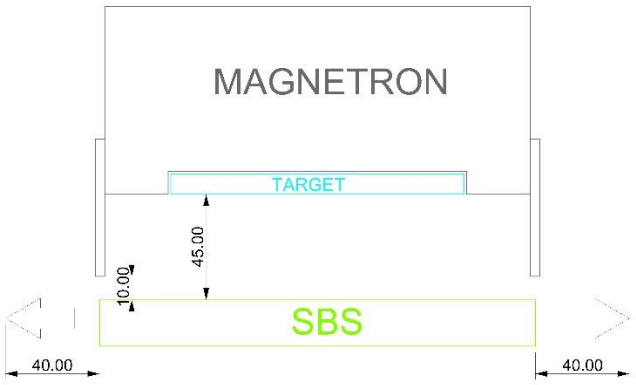

Figure 2.2 Magnetron, substrate and target arrangement in the system.

Moreover, heater temperature, substrate velocity, sputtering power, argon flow, and chamber pressure can be changed by means of a user interface.

2.2 Experimental Procedure

All the experiments were done in a clean room environment to ensure the pureness of the sputtered films. Before starting experiments, the main chamber was vacuumed until the base pressure was less than 5 x 10^{-6} Torr. Once this pressure was reached, system was ready for the coating process. Then, substrates were prepared and placed on a substrate holder and this time load lock part was vacuumed until 1 x 10^{-3} Torr. After this, substrate was transferred to the main chamber for the deposition process. Due to transfer procedure main chamber pressure decreases, thus before starting experiments it was waited until main chamber pressure gets to base pressure.

Then process parameters were set by using the user interface of the system, adjustable parameters of the system are given in Table 2.1. Once this parameters were set, system automatically starts the procedure and completes the coating.

Table 2.1 Recipe parameters

Recipe name:
Substrate material:
Coating type:
DC Coating:
RF Coating:
Magnetron selection:
Magnetron I- II- III- IV- V:
Heating parameters:
Preheating:
Heating while coating:
DCPS Parameters:
Target material:
Mode selection:
Ignition power:
Target clean:
Coating power:
Substrate bias:
Pressure Control Parameters:
Argon flow:
Nitrogen flow:
Set pressure:
Substrate Movement Parameters:
Oscillation number:
Oscillation speed:

For some experiments, using automatic mode of the system was not possible and semi-automatic mode was used for such conditions.

Semi-automatic process steps are summarized in below;

When substrate preparation and transportation to main chamber was finished, by using substrate "movement control" menu, substrate was moved under to the target that will be used in the sputtering process. When substrate heating was necessary, "heater control" menu was used to set temperature to the heaters. Then, magnetron to use was activated from the "magnetron selection" menu and gas inlet valve of the target was opened from the "shut off valves control" tab. Then by using "pressure control parameters" menu, argon flow rate and process pressure was set. Power supply (DC or RF) to be used during coating was activated from related menus. Finally, substrate speed and number of oscillations were set and coating procedure was initialized. When the oscillations were finished, the same steps were done in the reverse order.

Throughout the experiments, the target to substrate distance was 45 mm and the substrates were 4 and 6 inch square polished alumina. For the resistivity characterization purposes 4 inch and for the designed process experiments 6 inch substrates were used. The base pressure was lower than 5×10^{-6} Torr and substrate speed was 3.33 mm/s. Sputtering conditions were changed at 3 levels for DC power, argon (Ar) gas flow rate and pressure which is shown in Table 2.2. Details of the experiments is given in the empirical modeling, experimental plan part.

Table 2.2 Deposition parameters for sputtered thin films.

Factors	**Levels**
Power (W)	100-300-500
Argon Flow (cm^3/min)	30-115-200
Pressure (mTorr)	2-6-10

2.3 Thickness Characterization

Thickness measurement techniques can be categorized as contact and noncontact techniques. Contact measurement method measures a defined step height. On the other hand non-contact method do not touch to the wafer surface. Most common non-contact technique is an optical techniques based on interferometry. Thicknesses of sputtered films were measured by using that stylus profiler (BRUKER). Therefore, a specially designed mask is used to get step heights in the film to be able to use a stylus profiler. Recessed patterns are used to minimize shadowing effect in the coating. The reason of shadowing effect is that obliquely incident particles and the preferential deposition on the hill causing the different height measurements near the edges. Therefore, minimizing the shadowing effect leads to more accurate thickness measurements. The schematic of the mask is shown in Figure 2.3 and the films coated with this mask and manufactured mask is shown in Figure 2.4.

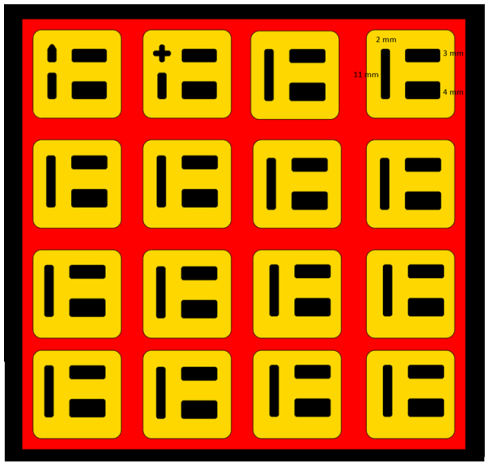

Figure 2.3 Mask design for the stylus profiler measurements.

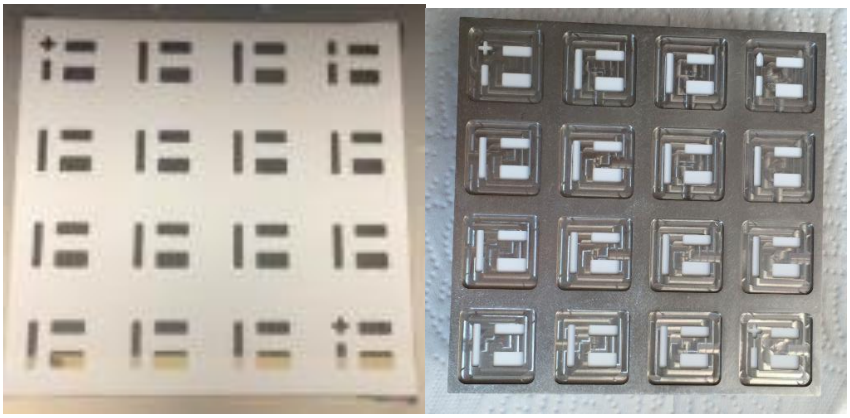

Figure 2.4 Coated alumina substrate and metal mask with patterns.

2.4 Resistivity Characterization

The electrical resistivity is defined as $\frac{\rho L}{A}$, where ρ is the bulk resistivity of the material, L is the length of the conductor and A is the cross-sectional area. For a square of thin film of thickness d, side lengths of L, the cross-sectional area becomes L x d. Sheet resistivity that is used commonly in the thin film evaluation is arisen as R_s which is defined as ohms/□.

In this study, resistivity measurements are used to get thickness data measurements quicker. Once thickness and resistivity relation is obtained, it can be used to measure the thickness of a thin film by only measuring its resistivity so that the results of the experiments can be observed after a very short time. Moreover, resistivity measurements does not require a mask for the deposition process so that it is possible to produce thin films without patterns. This allows taking measurements from all points on the wafer which is important to track within wafer uniformity. Therefore in order to use resistivity measurements to reach thickness measurements of a thin film, relation between thickness and sheet resistivity for a specific material and process must be known or obtained. For this purpose, theoretical knowledge of resistivity models

and experimental works are utilized to predict thickness from the sheet resistivity. Theoretical background used in this characterization are given in the next part.

2.4.1 Resistivity Model

Surface roughness and grain size are the two important parameters that affect the electron conduction in fine grained thin metal films when the film thickness is sufficiently small to impact the conduction of electrons [28]. All materials have a bulk resistivity, ρ_0, which contains the intrinsic resistivity of the material. Bulk resistivity can change with the impurities in the film and usually fixed by the deposition process. The bulk resistivity is degraded by two more mechanisms in thin films;

$$\rho = \rho_o \cdot \alpha_{F-S} \cdot \alpha_{M-S} \tag{2.1}$$

Grain boundary scattering (α_{M-S}) is captured by the Mayadas and Schatzkes models [29] and the surface scattering (α_{F-S}) is captured by the Fuchs-Sondheimer and Namba models [28].

The degradation due to the grain boundaries is given by;

$$\alpha_{M-S} = \frac{1}{3}\left[\frac{1}{3} - \frac{\alpha}{2} + \alpha^2 - \alpha^3 \ln\left(1 + \frac{1}{\alpha}\right)\right]^{-1} \tag{2.2}$$

$$\alpha = \frac{\lambda}{D} \cdot \frac{R}{1 - R} \tag{2.3}$$

where;

λ, mean free path of electrons

D, average grain size

R characterizes the impact of the grain boundary on scattering with R=1.0 corresponding to complete elastic scattering and R=0.0 corresponding to total loss of electrons and α quantifies the importance of grain boundary scattering.

The degradation due to high surface roughness and scattering is separately modeled and given by;

$$\alpha_{F-S} = \left[1 - \left(\frac{h}{d}\right)^2\right]^{-1/2} + \frac{3\lambda(1-P)}{8d}\left[1 - \left(\frac{h}{d}\right)^2\right]^{-3/2} \quad (2.4)$$

where;

h, the surface roughness

d, film thickness

P is the coefficient that characterizes the reflection at the surface with P=1.0 capturing complete elastic scattering and P=0.0 corresponding to total loss of electrons.

2.4.2 Resistivity Experiments

An experimental plan for the initial resistivity calibration of Cu was designed which is shown in Table 2.3. Four experiments with different number of passes were done as planned. The reason of this was to get a resistivity data for different thicknesses.

Table 2.3 Runcard of resistivity characterization experiments.

Run Order	Number of Pass	Power (W)	Argon Flow (cm^3/min)	Pressure (mTorr)
1	1	500	100	3
2	2	500	100	3
3	4	500	100	3

Table 2.3 (continued)

4	6	500	100	3

During sputtering process, a specially designed mask shown in Figure 2.4 was used to create patterns on the films and measurements were taken from these points. In order to minimize shadowing effect 4 mm strips were used to measure both thickness and resistivity on 16 sites. These runs were carried out on 4'' substrates and sheet resistivity of the sputtered films were analyzed by using four point probe (Signatone Quadpro-Figure 2.5). The resulting measurements are in ohm per square to indicate resistance of one square of material in horizontal plane. The system measures the voltage, V, while forcing a current, I. The sheet resistance and resistivity of the layer are calculated from that V/I measurements.

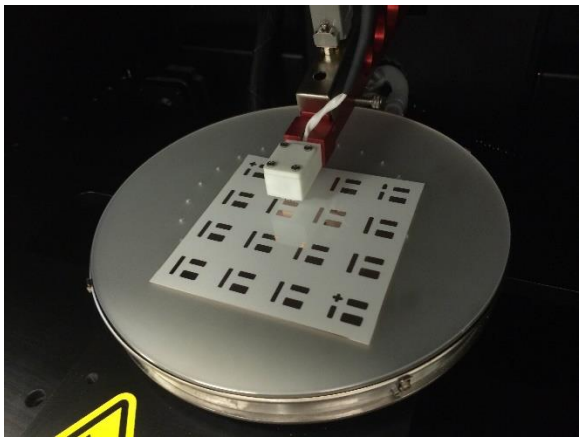

Figure 2.5 Four point probe system.

2.4.3 Resistivity Model Fitting

For the sheet resistivity characterization, resistivity and thickness data taken from the same points of substrates were used to tune the fitting parameters of the model.

Thickness measurements of the experiments for sputtered Cu film can be seen in Figure 2.6. This relation indicates that thickness increases linearly as number of pass increases.

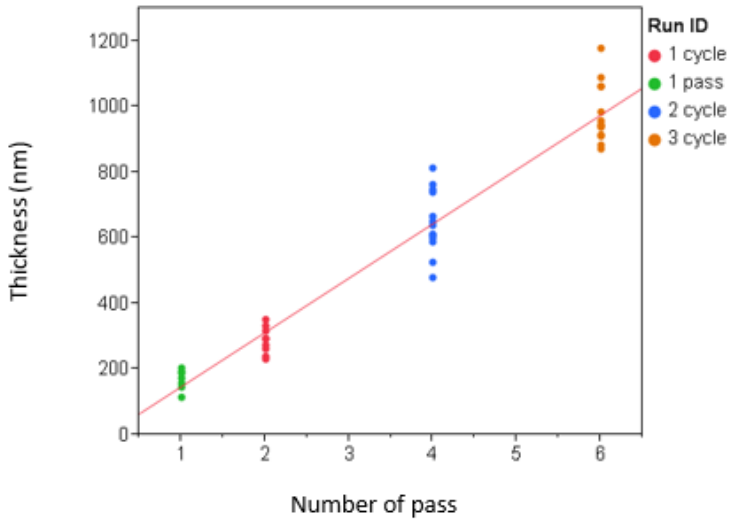

Figure 2.6 Change in thickness of the films as a function of number of pass.

Resistivity measurements taken from the same points can be seen in Figure 2.7. As expected, there is exponential rise in resistivity for thinner films and resistivity range of thinner films is larger because thickness variations in thinner films impact resistivity more significantly.

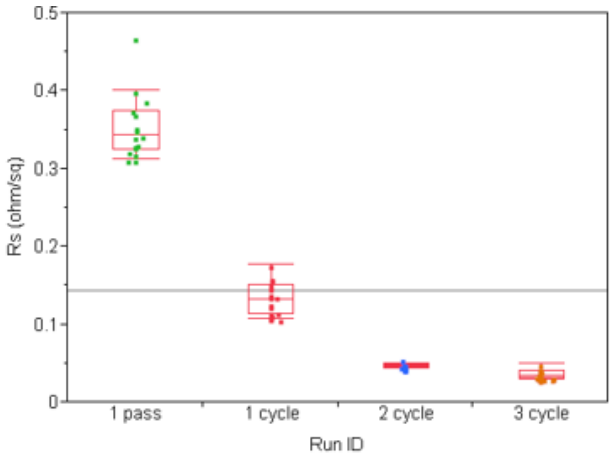

Figure 2.7 Change in resistivity of the films as a function of number of pass.

Figure 2.8 shows the thickness and sheet resistivity relationship based on these experiments and theoretical background. The literature values of R, P and ρ_0 values explained in previous part were changed to have a better agreement with the experimental data as shown in Table 2.4. Since properties of the films change with the operation conditions, sputtering systems, geometrical configuration, these parameters can be adjusted to have a better fit the experimental data. Different R values indicates that more elastic collisions on grain boundaries. The reason of change in bulk resistivity can be the impurities inside the film.

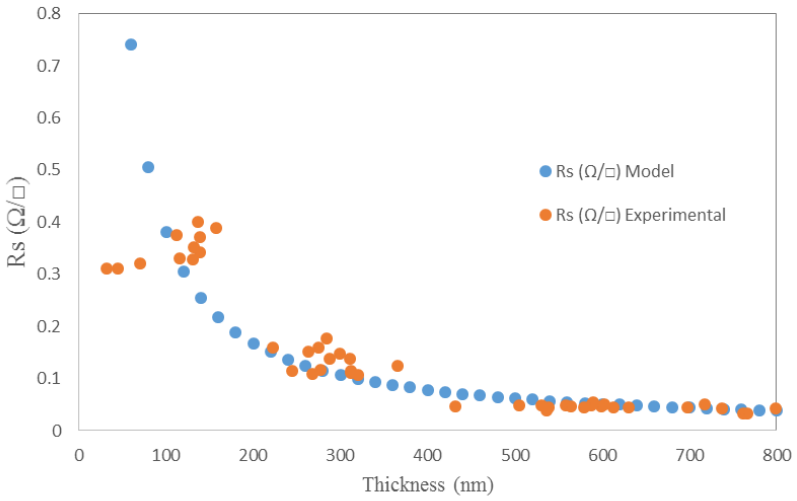

Figure 2.8 Comparison of experimental and modeled sheet resistivity with respect to thickness for Cu thin films.

Table 2.4 Literature and fitted data for resistivity characterization of Cu.

Parameter	**Literature Data**	**Fitted Data**
λ (nm)	39	39
P	0.96	0.95
R	0.05	0.35
ρ_0(μΩ.cm)	2.5 (for sputtered Cu)	2.9

2.5 Temperature Characterization

Temperature characterization experiments were done to find out the temperature distribution within the substrate during coating process and under the heaters. For this purpose, seven K type thermocouples were attached to a 6” substrate as shown in Figure 2.9. High conductivity paste were used for the bonding of thermocouples in order not to disrupt the heat transfer process within the substrate.

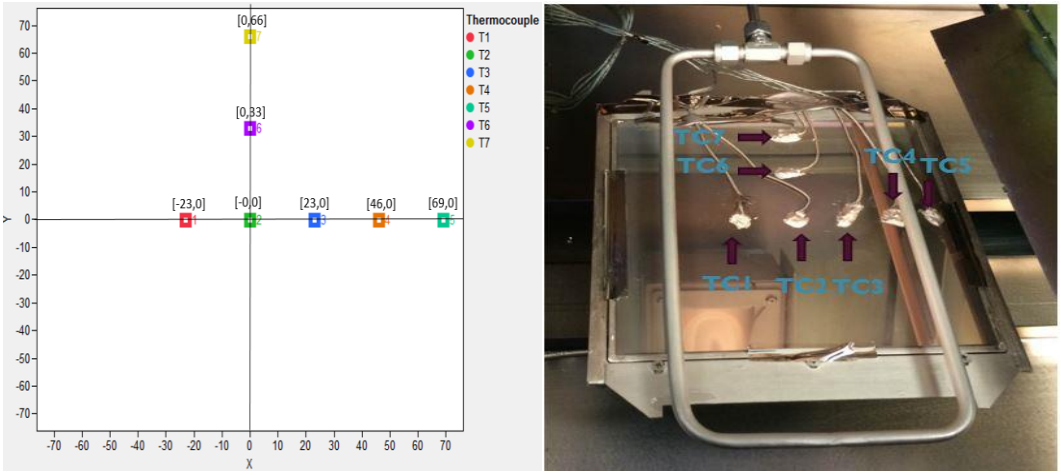

Figure 2.9 Thermocouple distribution for the temperature characterization experiments and the real setup.

Since deposition takes place in a vacuum chamber, a feed through fitting was used to put the wires out of the chamber. Temperature data of seven thermocouples was taken instantaneously by means of a data acquisition equipment. Temperature measurements were performed when the substrate was stationary due to the wires of thermocouples. Because while moving the substrate, there is always a risk of wires to interfere with the target shields and lose connection with the substrate. Two sets of experiments were done with these setup, measuring the substrate temperature during deposition at different conditions and under different heaters. Details of these experiments is also given in empirical modeling section.

CHAPTER 3

MODELING

3.1 Theoretical Modeling

The modeling part of this study has two side, one side is theoretical modelling approach and the other side is empirical approach. The main goal of this modeling studies is the sputtering system used in the thin film laboratory of ASELSAN. In this section the structure and approach of deposition and thermal models will be described. Flux model will be used to predict the flux distribution on substrate and the thermal model will be used to estimate the temperature distribution of the substrate during deposition processes. Primary goal of the flux model is to understand the effect of geometrical factors and based on these findings to set the optimum geometrical parameters for the real experiments. Based on these models, it is possible to observe the behavior of the system under various conditions and allows to estimate some process conditions at an early stage. The two model of the process was also built to reduce the number of the experiments and by doing so to decrease the cost in other words to support the empirical model. Moreover, the models can be used to optimize the system performance at a later stage.

3.1.1 Flux Model

Main objective of the thin film deposition research is to reach good quality thin films in terms of both chemical and physical characteristics. In addition to this, properties like film uniformity, surface covering and filling the spaces is equally important for the cases involving layers above the thin film coatings. There are many modeling studies to predict the angular distributions of target atoms on substrate.

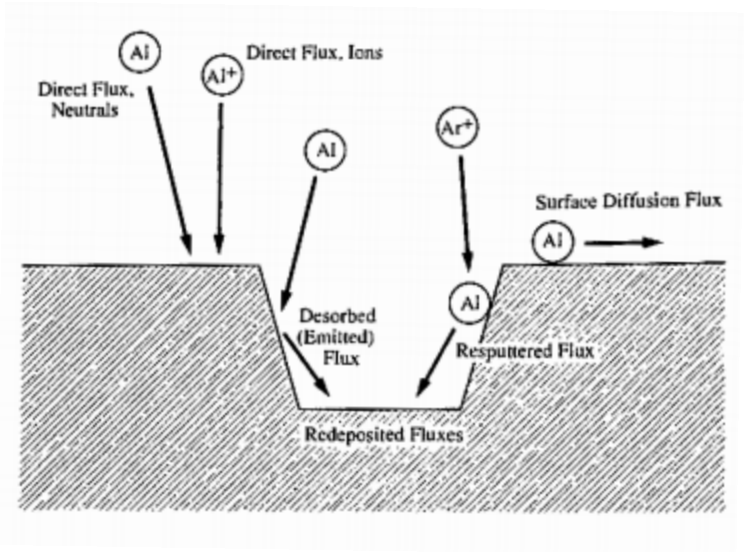

Figure 3.1 Surface fluxes in physical vapor deposition systems used in simulation models [11]

$$F_{net}^{i} = F_{direct(neutrals)}^{i} + F_{direct(ions)}^{i} + F_{redep}^{i} + F_{diff.in}^{i} - F_{emitted}^{i} - F_{sputtered}^{i} - F_{diff.out}^{i} \quad (3.1)$$

One of the modeling approach is to account direct fluxes for emitted angle distributions at each source point and combine this with gas-phase collisions and geometry of the system. Surface fluxes in sputtering processes is given in Figure 3.1 and total flux equation is given in Equation 3.1. Drawbacks of this method are the complexity of the system and need for the additional data to obtain proper solution [11]. This complex approach involves a computational fluid dynamic (CFD) finite element method to

predict velocity and pressure distribution of working gas, plasma model to predict flux and energy of Ar ions, Monte Carlo simulations to follow the energy loss of sputtered atoms while being transferred from source to substrate and also molecular dynamics studies to reach angle distribution of and sputter yield of atoms [30].

In this thesis study simplified approach was utilized to model the flux distribution on substrate in order to understand the effect of geometrical parameters. For the ideal case of deposition from a clean, uniformly emitting point source on a substrate, the rate of deposition varies with respect to cosine law.

In this model, system is modeled by considering the target as a summation of multiple point sources. These points generate a flux that is distributed according to the cosine law. The incident ions break off materials from the surface and form a cosine distribution from the target. Since the system is planar magnetron system, target and substrate are parallel to each other as shown in Figure 3.2.

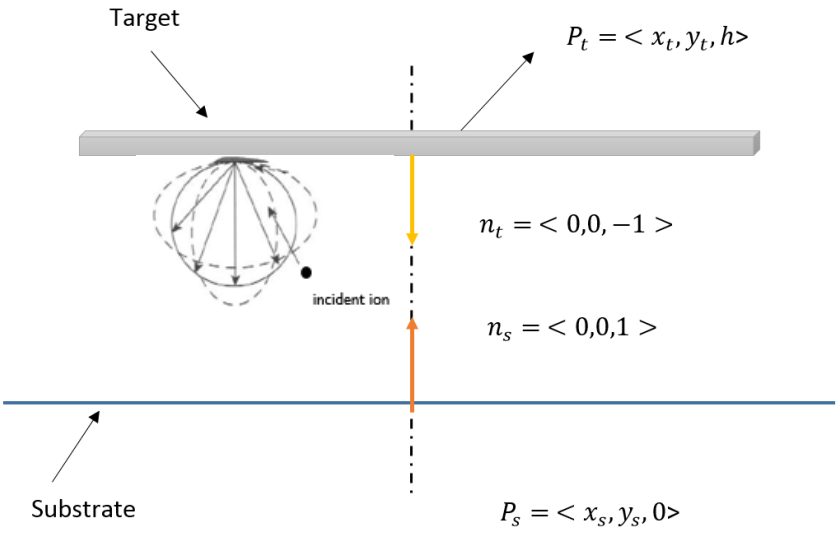

Figure 3.2 Target-substrate configuration.

If one defines a point on the target as P_t and a point on the substrate as P_s, then the differential flux incident on P_s, denoted by dF is related to the flux originating from P_t, with differential surface area dA_t, denoted by F_t is given in Equation 3.2,

$$dF = \frac{F_t}{\pi}\frac{cos\theta_t cos\theta_s}{r^2}dA_t \tag{3.2}$$

where Θ denote the angle between the target P_t and substrate P_s, and r is the distance between the two points. The above equation can be written in vector form as follows.

$$dF = \frac{F_t}{\pi}\frac{(n_t \cdot \vartheta).(-n_s \cdot \vartheta)}{(\vartheta \cdot \vartheta)^2}dA_t \tag{3.3}$$

For the case of a rectangular target which is located a distance of h from the substrate, definitions that need to go into the model equation are defined below;

$$n_t = < 0,0,-1 > \tag{3.4}$$

$$P_t = < x_t, y_t, h > \tag{3.5}$$

$$n_s = < 0,0,1 > \tag{3.6}$$

$$P_s = < x_s, y_s, 0 > \tag{3.7}$$

$$\vartheta = \mathrm{P_s} - \mathrm{P_t} = < \mathrm{x_s} - \mathrm{x_t}, \mathrm{y_s} - \mathrm{y_t}, -\mathrm{h} > \tag{3.8}$$

$$dA_t = dx_t dy_t \tag{3.9}$$

F_t relates the flux on the substrate at location (x_s, y_s) as a function of target geometry and the target to substrate distance. For the model, the equation in vector form is used. The code for this model was written in MATLAB. The code written is given in APPENDIX A.1.1. The code calculates the flux incident on substrate, which moves in the direction perpendicular to the long axis of the cathode, from a point source.

The sequence of code used in the simulations is shown in Figure 3.3. Firstly, the code is generated for static flux distribution where there is no substrate movement, then model is improved by taking substrate movement and substrate speed into account. In addition to these factors, geometrical parameters (target and substrate sizes) and target-to-substrate separation are critical for the simulations.

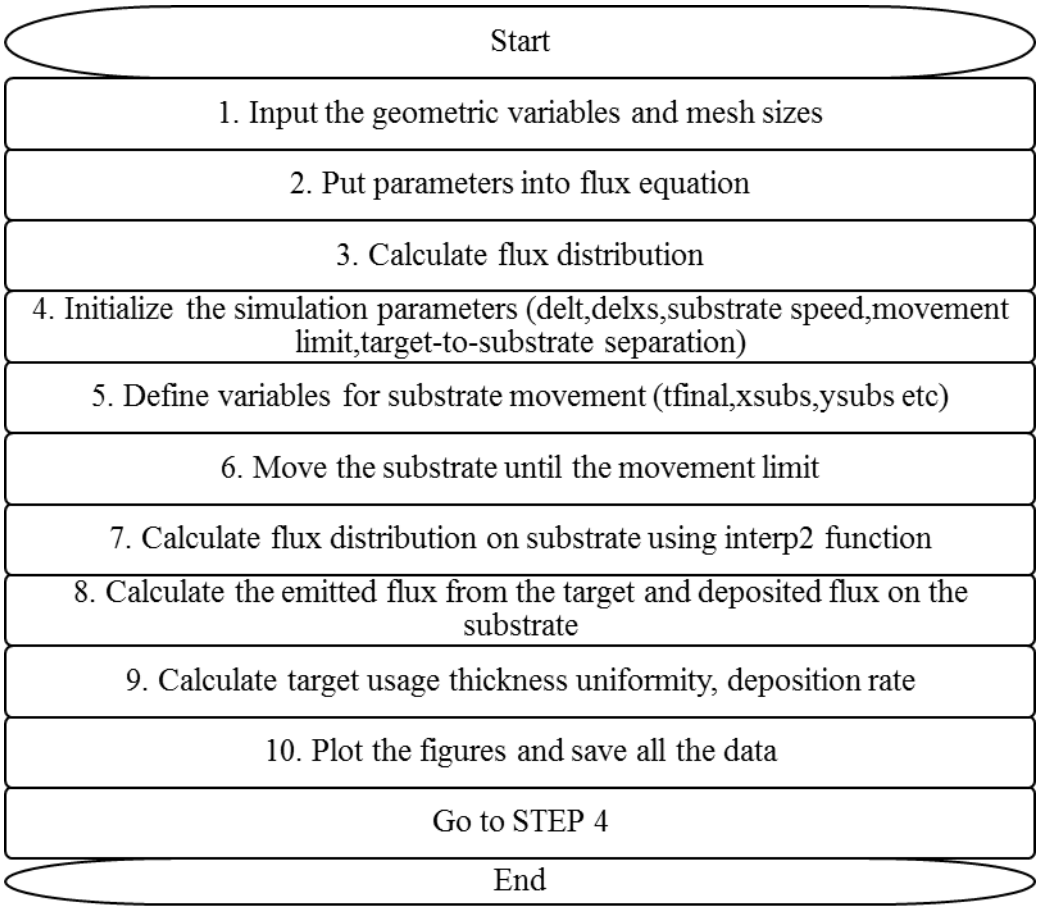

Figure 3.3 MATLAB flux distribution code sequence.

3.1.2 Thermal Model

In this part, the development of thermal model is described that predicts the substrate temperature which is affected by the sputtering conditions and the heaters. Substrate temperature is important factor that impacts electrical and structural properties of the

sputtered films. Therefore, predicting the temperature is essential to ensure the reproducibility of the films. This study uses two approaches to model temperature distribution within the moving substrate during deposition and under the heaters. For both approaches, substrate movement adds extra complexity to the system. Therefore we designed the models to support each other.

First approach to thermal modeling was to use a finite element solvers, in this case ANSYS 15. Finite element solvers have many advantages including solving problems for complex geometries, easily describing the boundary conditions and user friendly interface at latest versions. However it is not easy to integrate substrate movement into finite element solver. Therefore, a simplified approach is designed in MATLAB by using finite difference method. Firstly, finite element solver approach will be explained and then MATLAB model will be given with the simplifications.

3.1.2.1 ANSYS Model

In the system two main heat source is available, one is heaters and the other is plasma. There are 6 heaters (4 small, 2 large) in the system to provide substrate heating. Large heaters are designed to heat substrate prior to deposition so that there are two of them at two side of the chamber. Heater 1 is used with magnetron 1-2-3 and heater 6 is used with magnetron 4-5 so that heat loss from the substrate during transfer procedure to selected magnetron is reduced. Heater 2 to 5 are used to eliminate heat loss at time of deposition when the substrates moves out of the limits of the target shields. Schematic diagram of the whole magnetron sputtering system is shown in Figure 3.4. As it is seen, it is difficult to create whole geometry in to the ANSYS software and solve the complex heat transfer problem. Therefore, simplifications are necessary for both geometry and heat transfer mechanisms.

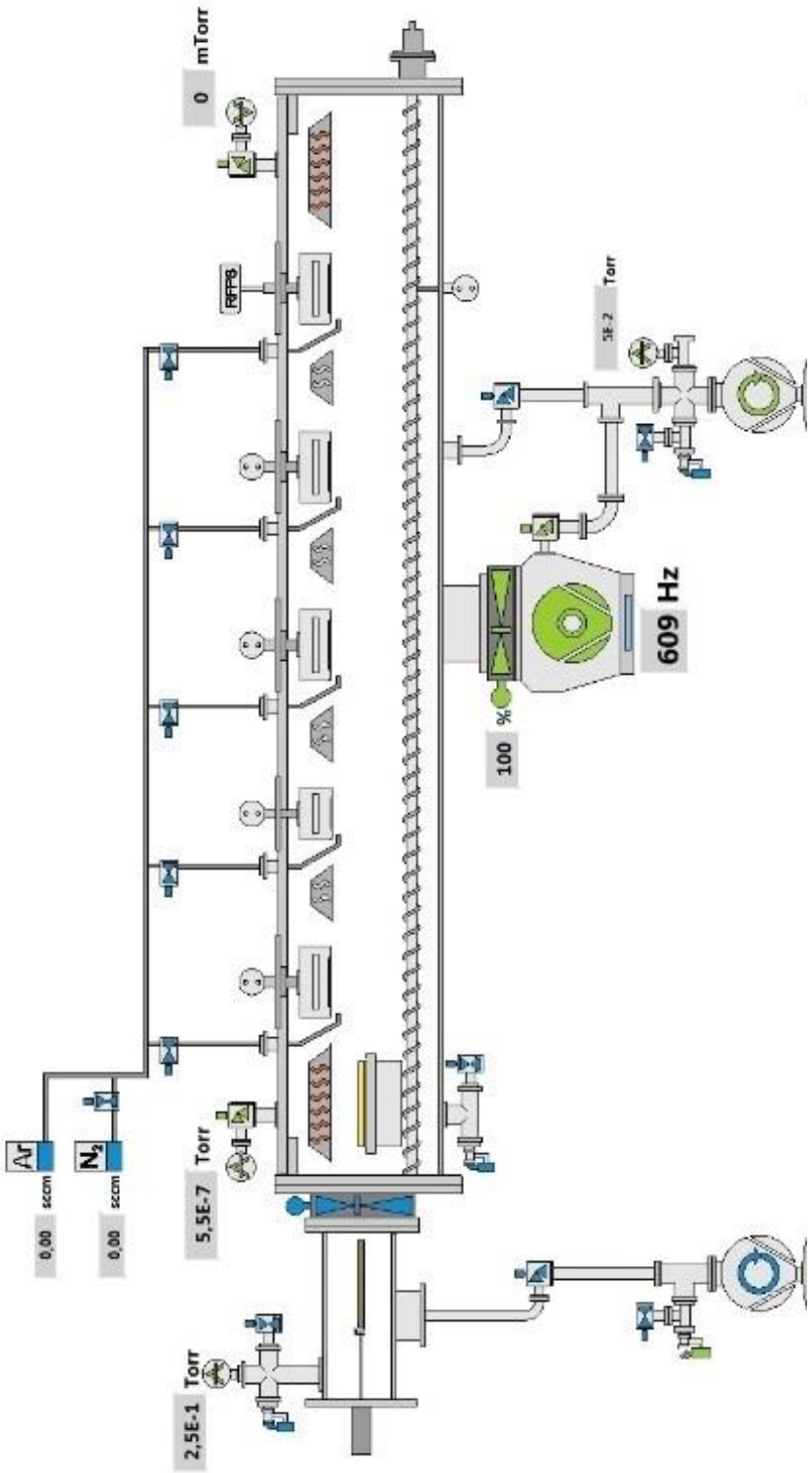

Figure 3.4 Schematic drawing of magnetron sputtering system.

The other heat source to be considered in the system is that magnetron discharge in the course of sputtering process. The heat transferred to the substrate composes of the following;

- Radiative heat source from the target surface due to collisions between the target surface and the ejected ions (Radiation Flux)
- Heat transfer from the heaters and the reflectors in the system (Radiation Flux)

The output energy to be dissipated from substrate involves the following;

- Radiation from the film surface (Radiation Flux)
- Heat transfer from thin film surface to the substrate (Conduction)
- Heat loss to substrate frame (Conduction)
- Heat loss through the chamber walls (Conduction)

Assumptions done to simplify the thermal model are listed below;

- Convection within the deposition chamber is ignored, the reason is that high vacuum environment inside the chamber. Pressure is about $5x10^{-6}$ Torr.
- Convection between room and chamber walls.
- Geometry of the system is simplified since it takes long time to solve such a large geometry in a finite element solver. Simplified geometry involves the substrate, substrate frame, heater, parabolic reflector (for large heaters) and reflector (for large and small heaters). The properties of this parts are given in Table 3.1.

Table 3.1 Material data of the parts

Part	**C_p** $(J/kg.K)$	**k** $(W/m.K)$	**ρ** (kg/m^3)	**ε**
Substrate (Alumina)	880	25	3800	0.9
Substrate Frame (Aluminum)	951	237.5	2689	0.1
Heater (Stainless Steel)	480	13.8	8055	0.4
Reflector (Aluminum)	951	237.5	2689	0.1
Target Material (Copper)	385	400	8933	0.05

Outside of the geometry of the system is given in Figure 3.5, a closer view is given in the Figure 3.6. As it is written before the system has heaters with two sizes, therefore, there are two geometry to model in ANSYS for heater analysis. Geometry of the small heaters are given in Figure 3.8 and Figure 3.9 and boundary conditions for the small heaters is given in Figure 3.10.

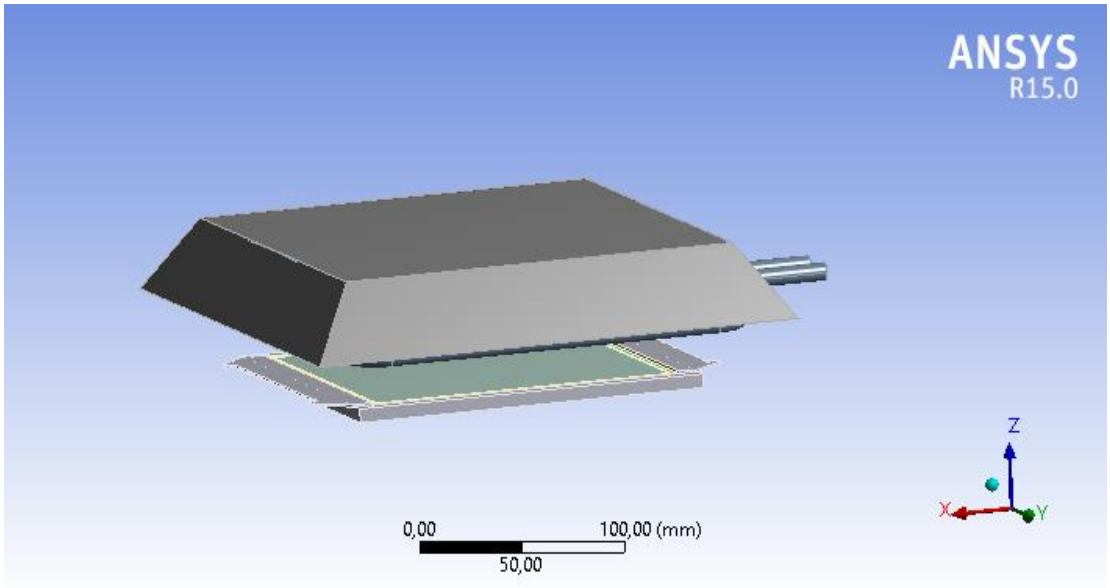

Figure 3.5 Exterior view of the system for large heater-substrate model.

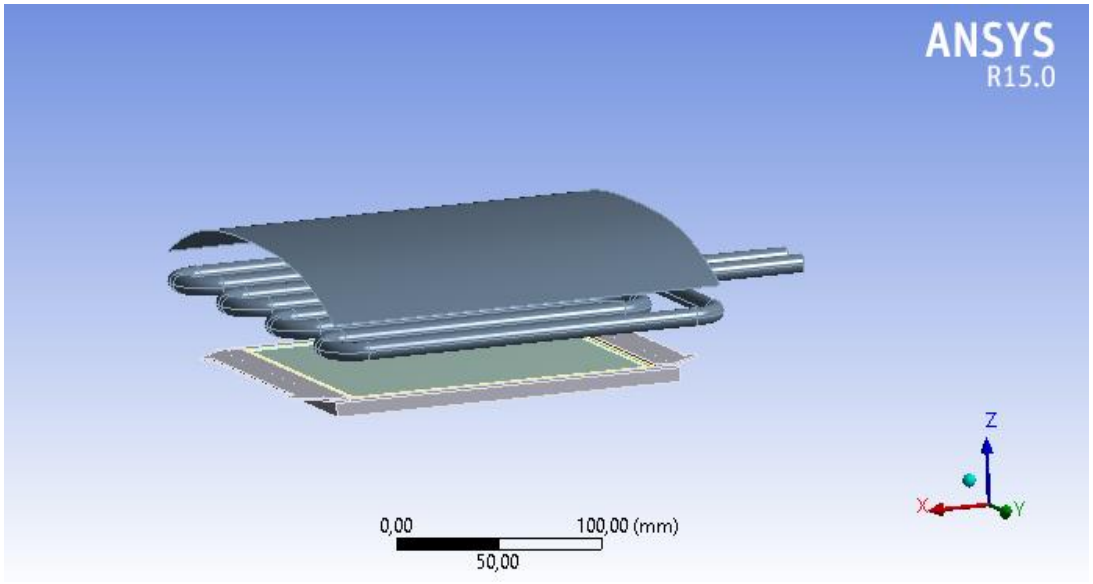

Figure 3.6 Geometry of the system revealing the large heater geometry and parabolic reflector.

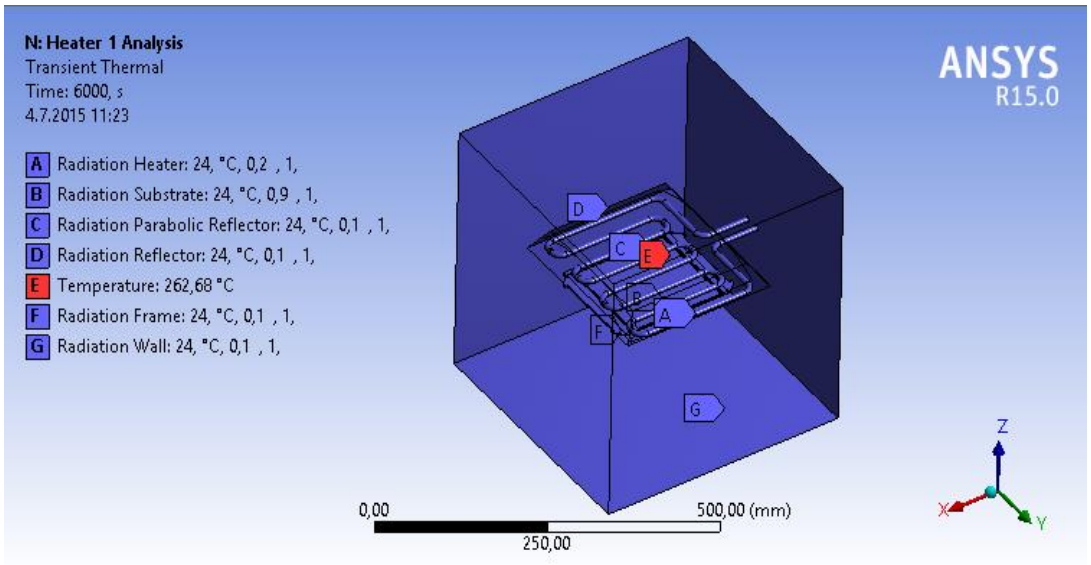

Figure 3.7 The boundary conditions for large heater system.

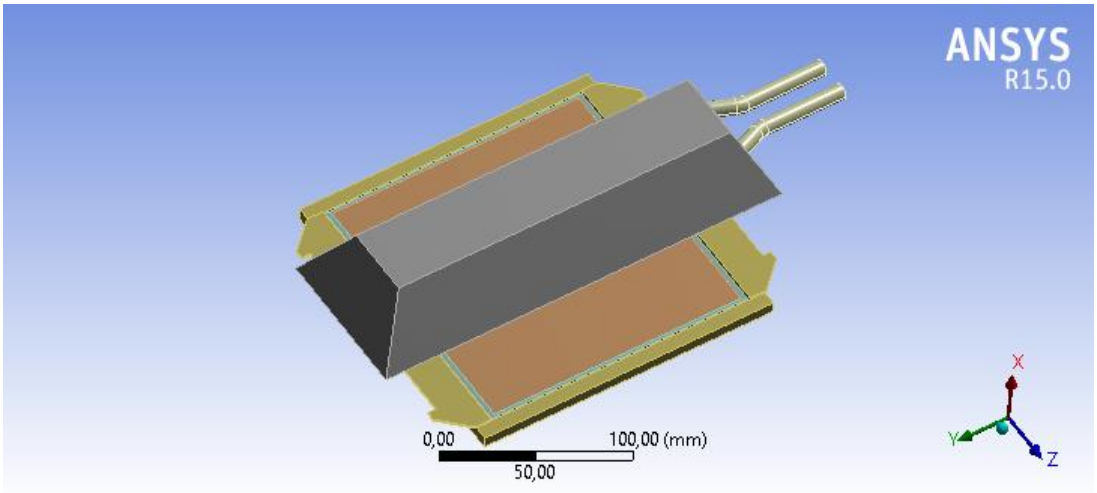

Figure 3.8 Exterior view of the system for small heater-substrate model.

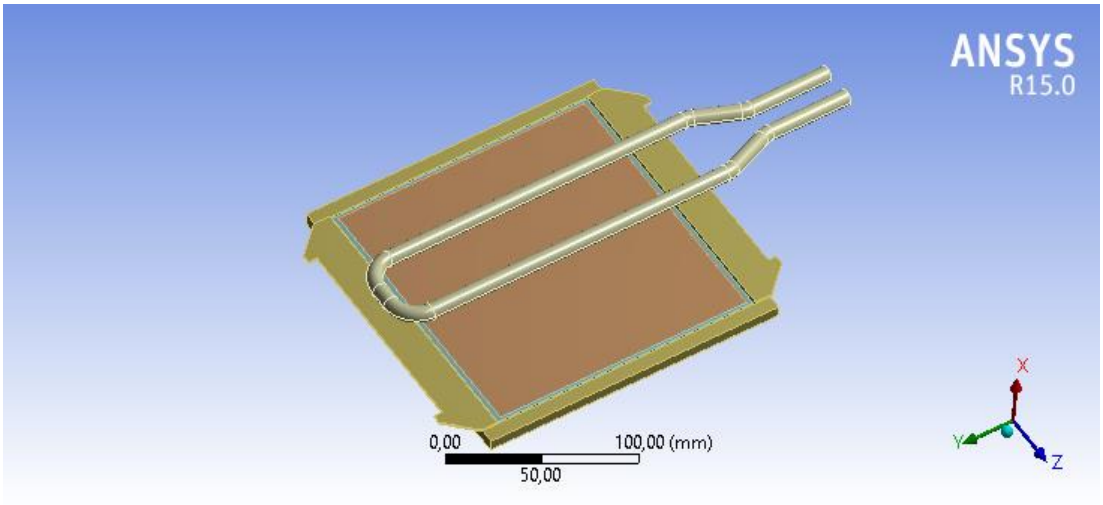

Figure 3.9 Geometry of the system revealing the small heater geometry.

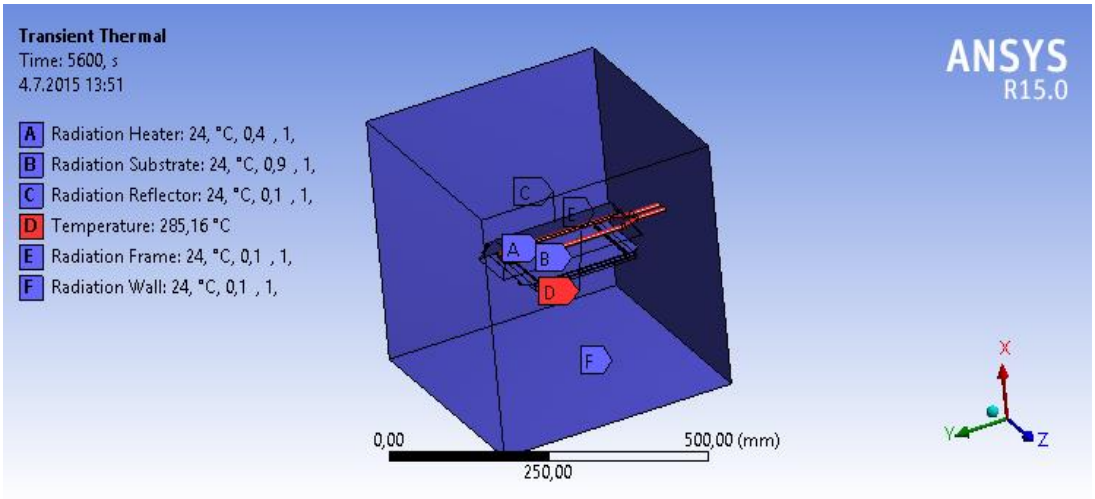

Figure 3.10 The boundary conditions for small heater system.

ANSYS gives a solution for the defined geometry and materials by solving necessary energy balance equations.

The conversation of energy statement is expressed as;

$$(Rate\ of\ energy\ in) - (Rate\ of\ energy\ out) + (Rate\ of\ energy\ generation) = (Rate\ of\ energy\ accumulation) \tag{3.10}$$

General energy balance for the substrate-heater system involving conduction and radiation mechanism for 5 radiating bodies is given as follows:

$$\frac{\partial}{\partial t}\left[\rho C_p T\right] = k\nabla^2 T + A_i\sigma\sum_{i=1}^{5}\left[F_{ij}\left(\varepsilon T_i^4 - \alpha T_j^4\right)\right] \tag{3.11}$$

The terms ε, σ, α, F_{ij} T_i and T_j are, respectively the emissivity of the material, the Stefan-Boltzmann constant (5.729×10^{-8}W/m^{2}K^4), absorptivity of the substrate,

surface view factor (view factor between reflecting surfaces) and the temperature of the reflecting surfaces.

Since conduction takes place in all dimensions and considering the complex geometry to complete the view factor calculations leads us to use finite element solver. One of resulting equations is shown below. ANSYS solves the set of equations, as a result, it is possible to have temperature of all bodies and surfaces.

$$\rho C_p \frac{\partial T}{\partial t} = -k\frac{\partial^2 T}{\partial x^2} - k\frac{\partial^2 T}{\partial y^2} + k\frac{\partial^2 T}{\partial z^2} + F_{ij}\sigma\frac{\partial}{\partial z}\left[\left(\varepsilon T_i^4 - \alpha T_j^4\right)\right] \tag{3.12}$$

3.1.2.2 MATLAB Model

In this part, energy balances were given including conduction and radiation heat transfer mechanisms. Convection within the deposition chamber was ignored, the reason is that high vacuum environment inside the chamber. Pressure is about $5x10^{-6}$ Torr.

General energy balance is given as follows:

$$\begin{aligned}[Conduction\ in\ all - directions|_{in} - Conduction\ in\ all \\ -directions|_{out}] + [Radiation|_{in} - Radiation|_{out}] \\ = Accumulation\end{aligned} \tag{3.13}$$

$$\begin{aligned}q_x|_x \Delta y\Delta z\Delta t - q_x|_{x+\Delta x}\Delta y\Delta z\Delta t + q_y|_y \Delta x\Delta z\Delta t + q_y|_{y+\Delta y}\Delta x\Delta z\Delta t \\ + q_z|_z \Delta x\Delta y\Delta t + q_z|_{z+\Delta z}\Delta x\Delta y\Delta t \\ + q_{rad-z}|_z \Delta x\Delta y\Delta t + q_{rad-z}|_{z+\Delta z}\Delta x\Delta y\Delta t \\ = \Delta x\Delta y\Delta z[\rho C_p(T|_{t+\Delta t} - T|_t]\end{aligned} \tag{3.14}$$

Then both sides divided with $\Delta x\Delta y\Delta z\Delta t$;

$$\frac{q_x|_x - q_x|_{x+\Delta x}}{\Delta x} + \frac{q_y|_y - q_y|_{y+\Delta y}}{\Delta y} + \frac{q_z|_z - q_z|_{z+\Delta z}}{\Delta z} + \frac{q_{rad-z}|_z - q_{rad-z}|_{z+\Delta z}}{\Delta z} = \frac{[\rho C_p(T|_{t+\Delta t} - T|_t]}{\Delta t} \quad (3.15)$$

where conduction and radiation terms are defined as below;

$$q_x = -kA\frac{\partial T}{\partial x} \quad (3.16)$$

$$q_y = -kA\frac{\partial T}{\partial x} \quad (3.17)$$

$$q_z = -kA\frac{\partial T}{\partial y} \quad (3.18)$$

$$q_{radz} = (\varepsilon T^4 - \alpha T_s^4)F_{ij}A\sigma \quad (3.19)$$

σ is the Stefan Boltzmann constant.

By using these equations and taking the limit of Equation 3.15 becomes as follows;

$$-\frac{\partial}{\partial x}\left[-kA\frac{\partial T}{\partial x}\right] - \frac{\partial}{\partial x}\left[-kA\frac{\partial T}{\partial x}\right] - \frac{\partial}{\partial z}\left[-kA\frac{\partial T}{\partial z}\right] - \frac{\partial}{\partial z}\left[(\varepsilon T^4 - \alpha T_s^4)F_{ij}A\sigma\right] = \frac{\partial}{\partial t}[\rho C_p T] \quad (3.20)$$

Resulting equation is represented in Equation 3.20 and this final form of the equation cannot be solved analytically. Therefore, some simplifications were done on this equation. First of all it is assumed that substrate temperature distribution does not change in the z-direction because substrate thickness is very small (0.5µm). Moreover, complex geometry of the system makes view factor calculations difficult. Actually, in order to have a complete thermal model of the system one should also model the plasma, so that just involving radiation heat transfer mechanism does not solve the thermal problem in this case. Therefore in order to complete the models experimental results of the heater and deposition experiments will be used. For this MATLAB model, radiation term will be taken in to account by considering it as heat generation term for the substrate and since is it not possible to solve the equation analytically, numerical techniques will be used. For this case finite difference method were used.

With this simplifications and assumptions the equation was reduced as given in Equation 3.21;

$$q_x|_x \Delta y h - q_x|_{x+\Delta x} \Delta y h + q_y|_y \Delta x h - q_y|_{y+\Delta y} \Delta x h + \dot{Q}_{rad} - \dot{Q}_{loss} = \Delta x \Delta y h [\rho C_p \frac{\Delta T}{\Delta t}] \quad (3.21)$$

$[\dot{Q}_{rad} - \dot{Q}_{loss}]$ term will continue as $\dot{Q}$ for the next derivations and finite difference method. For the finite difference approximation substrate is divided into meshes, and mesh size will be taken the same in both directions. Energy balance of one mesh and definition of each term can be written as below;

$$V \rho C_p \frac{dT_{m,n}}{dt} = q"_{x-\frac{dx}{2}} - q"_{x+\frac{dx}{2}} + q"_{y-\frac{dy}{2}} + q"_{y+\frac{dy}{2}} + \dot{Q} \quad (3.22)$$

$$q"_{x+\frac{dx}{2}} = -k \Delta y h \frac{T_{m,n} - T_{m-1,n}}{\Delta x} \quad (3.23)$$

$$q"_{x-\frac{dx}{2}} = -k \Delta y h \frac{T_{m,n} - T_{m-1,n}}{\Delta x} \quad (3.24)$$

$$q"_{y+\frac{dy}{2}} = -k \Delta x h \frac{T_{m,n} - T_{m,n-1}}{\Delta y} \quad (3.25)$$

$$q"_{y+\frac{dy}{2}} = -k \Delta x h \frac{T_{m,n} - T_{m,n-1}}{\Delta y} \quad (3.26)$$

where;

$$V = \Delta x \Delta y h \quad (3.27)$$

If we put this relation into Equation 3.22, resulting equation is given as following;

$$\Delta x \Delta y h \rho C_p \frac{dT_{m,n}}{dt} = kh(-4T_{m,n} + T_{m+1,n} + T_{m-1,n} + T_{m,n+1} - T_{m,n-1}) + \dot{Q} \quad (3.28)$$

Since the problem is unsteady state, $T_{m,n}$ also change with respect to time as described in Equation 3.29.

$$\frac{dT_{m,n}^{p+1}}{dt} = \frac{T_{m,n}^{p+1} - T_{m,n}^{p}}{\Delta t} \tag{3.29}$$

The final equation solved in MATLAB for the internal nodes is given in Equation 3.30 and details of the MATLAB code is given in Appendix A.2.

$$T_{m,n}^{p+1} = T_{m,n}^{p} + \frac{\Delta t}{\Delta x \Delta y \rho C_p}\left[k(-4T_{m,n}^{p} + T_{m+1,n}^{p} + T_{m-1,n}^{p} + T_{m,n+1}^{p} + T_{m,n-1}^{p}) + \frac{\dot{Q}}{h}\right] \tag{3.30}$$

Energy balance changes with respect to the position on the substrate, therefore a representative node distribution is given in Figure 3.11 . The numbers inside the nodes refers to the energy balance equation for that specific node. Nodes with the same boundary conditions are given the same number.

1	4	4	7
2	5	5	8
2	5	5	8
3	6	6	9

Figure 3.11 Representative node distribution.

Table 3.2 Energy balance terms for the representative nodes.

Node	**Energy Balance**
1	$-2T_{m,n}^{p} + T_{m+1,n}^{p} + T_{m,n-1}^{p}$
2	$-3T_{m,n}^{p} + T_{m+1,n}^{p} + T_{m,n+1}^{p} + T_{m,n-1}^{p}$
3	$-2T_{m,n}^{p} + T_{m+1,n}^{p} + +T_{m,n-1}^{p}$
4	$-3T_{m,n}^{p} + T_{m+1,n}^{p} + T_{m-1,n}^{p} + T_{m,n-1}^{p}$
5	$-4T_{m,n}^{p} + T_{m+1,n}^{p} + T_{m-1,n}^{p} + T_{m,n+1}^{p} + T_{m,n-1}^{p}$
6	$-3T_{m,n}^{p} + T_{m+1,n}^{p} + T_{m-1,n}^{p} + T_{m,n+1}^{p}$

Table 3.2 (continued)

7	$-2T_{m,n}^{p}+T_{m-1,n}^{p}+T_{m,n-1}^{p}$
8	$-3T_{m,n}^{p}+T_{m-1,n}^{p}+T_{m,n+1}^{p}+T_{m,n-1}^{p}$
9	$-2T_{m,n}^{p}+T_{m-1,n}^{p}+T_{m,n+1}^{p}$

3.2 Empirical Modeling

In this thesis study, theoretical and empirical approaches were used together since complete modeling of a sputtering chamber includes interactions of argon flow, power, pressure and the geometry of the system which is difficult to predict with the models. Therefore, this chapter involves the empirical modeling approach to complete the sputtering process model. Since carrying out experiments for all parameters at all conditions is impossible, design of experiment approach (DOE) is crucial to decrease the number of experiments. One can use DOE approach for both computer simulations and real experiments. This section will cover the DOE for computer simulations to eliminate geometrical factors with the results of the simulations and end with the experimental plan generated based on this computer simulations for real experiments.

3.2.1 Experimental Design Approach- Model Based Design-How to Eliminate Geometrical Factors

In order to develop an experimental plan for this sputtering system, a model is built by using MATLAB as outline in previous parts. As it is stated geometrical parameters (target and substrate sizes), substrate movement, substrate speed, and target-to-substrate separation are the critical parameters for this case. In addition to these parameters, affecting the performance of the sputtering process, mesh size parameters (substrate, target mesh size and time step size) are included in the code in order to find

an optimum point between the results and CPU time. Since it takes plenty of time to complete a simulation, CPU time-result relation becomes significant. Table 3.3 shows the simulation factors and levels that is determined to understand the behavior of the sputtering system.

Table 3.3 Simulation factors and levels.

Factors	**Levels**	**Value**
Target Mesh Size [mm]	1	10
	2	5.0
	3	1.0
	4	0.5
	5	0.1
Substrate Mesh Size [mm]	1	10
	2	1.0
	3	0.1
	4	0.01
Time Step Size [s]	1	5.0
	2	1.0
	3	0.1
	4	0.01
Substrate Speed [mm/s]	1	0.33
	2	0.83
	3	1.67
Substrate Movement Limit [mm]	1	10
	2	25
	3	50
	4	100
	5	150
	6	200

Table 3.3 (continued)

Target Substrate Separation [mm]	1	30
	2	50
	3	70
Target Size [mm x mm]	1	125x250 (Target 1)
	2	75x125 (Target 2)
Substrate Size [mm]	1	152.4 - square
Simulation Time [cycle]	1	1

These values are set according to the limits of the sputtering machine and known geometrical parameters of the target-substrate position. Target and substrate mesh size and time step size are the computational parameters. Critical response of the system are determined as thickness uniformity, target usage and deposition rate. Definitions of the responses are given in Equations 3.31-3.33 as follows;

$$\text{Thickness uniformity} = \frac{\text{std(deposited)}}{\text{mean(deposited)}} \times 100 \tag{3.31}$$

$$\text{Target usage} = \frac{\text{total deposited atoms}}{\text{total emitted atoms}} \times 100 \tag{3.32}$$

$$\text{Deposition rate} = \frac{\text{total deposited atoms}}{\text{total time}} \tag{3.33}$$

3.2.1.1 Effect of Geometrical Factors

These values are set according to the limits of the sputtering machine which is designed by VAKSİS. Optimization for mesh sizes was done by using the static flux distribution and the optimum size was chosen as 1mm so that for the further simulations target mesh size is set to 1 mm at this part. The reason is that as seen in Figure 3.12, from 1.0 to 0.5 mm mesh size average deposition changes 0.25 percent therefore further reduction in mesh size is not effective since simulation time increases exponentially.

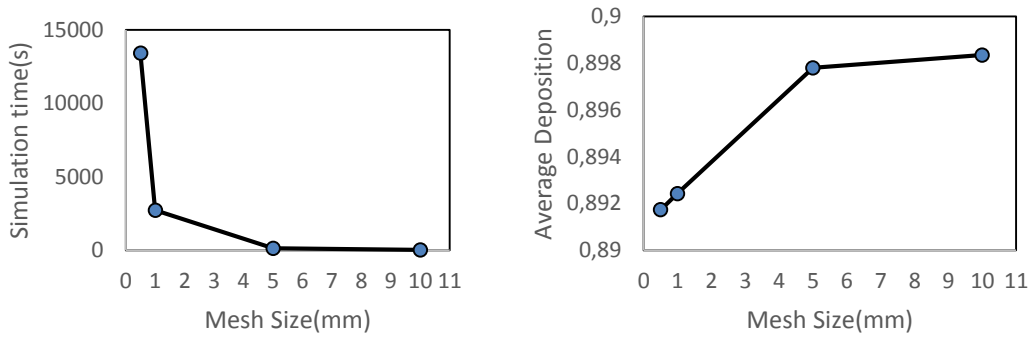

Figure 3.12 Variation of simulation time and average deposition with respect to mesh size at 30 mm target to substrate separation.

Since the substrate is moving, simulation time was taken as 1 cycle for all the simulations. Target size is considered at two levels by considering the small target and the large target. Based on these factors and levels 648 simulations were done to set substrate mesh size and time step size. According to the results of this simulations substrate mesh size is set to 1 mm and time step size was set to 0.1 seconds because decreasing mesh sizes further increased CPU time and magnitude of the MATLAB result file. Thus, analytical impact was fixed by fixing these parameters.

After setting mesh size parameters, 108 of all simulations was used to build the model which is composed of 3 level of substrate speed, 6 level of movement limit, 3 level of target-substrate separation and 2 level of target size. Factors and levels are seen in the Table 3.3. For data evaluation JMP software was used and data based on 108 simulations was analyzed. JMP is a tool for data analysis and design of experiments. Based on the regression results if individual effects of input parameters ((target-to-substrate separation (H), substrate speed (subsspeed), movement limit (movement), target dimension (Lt)) were considered, it was seen that substrate speed has no effect on thickness uniformity, target usage and deposition rate.

The significant geometrical factors for the sputtering process are target-to-substrate separation and movement limit. Since the simulations were executed at two level by considering the target 1 and 2, model is built for both targets separately. When parameters were introduced into JMP software, R squared values were examined to understand how well data points fit to the model. Thus, the best results were obtained when the target-to-substrate separation, logarithm of the movement limit and the combined effect of target-to-substrate separation and movement limit were introduced to JMP. Prediction profilers are important tool of JMP software to see the importance of the factors. Therefore prediction profilers were created for the geometrical analysis of the both targets which are shown in Figure 3.13 and 3.14.

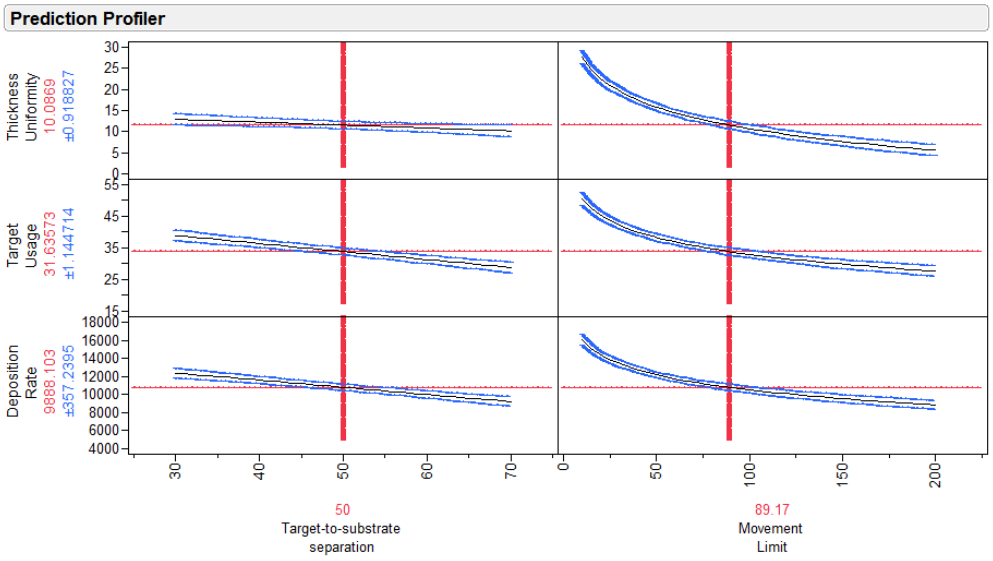

Figure 3.13 Effect of target-to-substrate separation and movement limit on thickness uniformity, target usage and deposition rate for target 1.

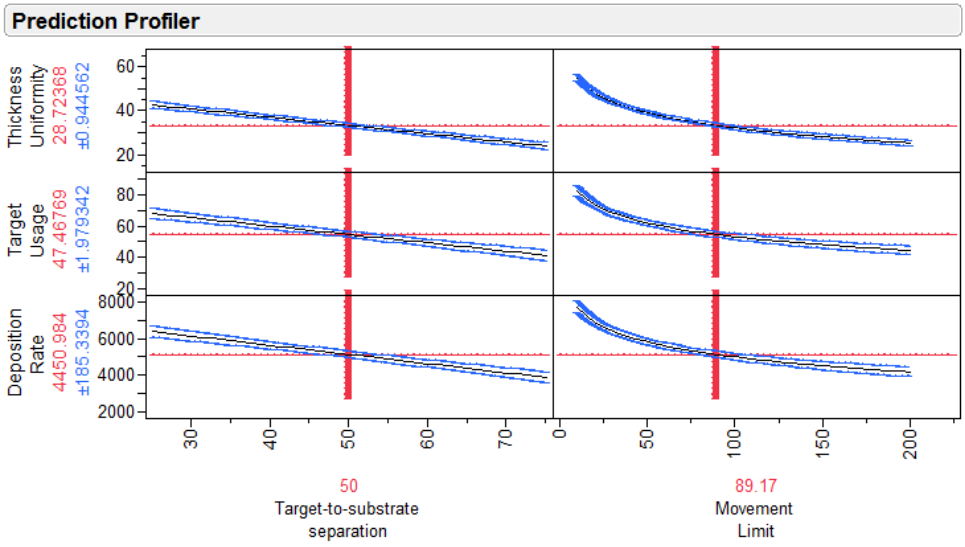

Figure 3.14 Effect of target-to-substrate separation and movement limit on thickness uniformity, target usage and deposition rate for target 2.

It is seen that increasing target-to-substrate separation decreases thickness non-uniformity which is a desired outcome, however target usage and deposition rate also decreases which is not desired. According to the results of these simulations target-to-substrate separation was chosen as 70 mm which is the maximum separation possible in this system. Moreover, it is found that movement limit is not effective after movement limit of 150 mm for both targets. However, movement limit has notable impact on critical process parameters, as the movement limit increases thickness non-uniformity decreases, on the other hand, target usage and deposition rate decreases. Therefore, real designed experiments was completed at maximum movement limit and separation. Geometrical parameters were fixed by using a model based approach. The most important result of this model based flux uniformity optimization was to decrease the number of real experiments while decreasing the time needed and cost of the experiments.

3.2.2 Experimental Plan

Properties of thin films are strongly dependent on process parameters such as sputtering power, chamber pressure, deposition temperature, argon flow rate, substrate movement, substrate-to-target distance and substrate temperature. In Table 3.4 these factors and responses are summarized. Thus, it is essential to model the sputtering process to achieve flux and thermal distributions and these models must be supported by the actual results obtained from the system.

Table 3.4 Sputtering process factors and responses.

Factors	**Responses**
Power	Growth rate
Pressure	Film uniformity
Temperature	Adhesion
Argon flow rate	Film morphology

Substrate movement	Substrate temperature
Heater temperature	
Substrate-to-target distance	Growth rate
Target usage	Thickness uniformity
Target size	
Thickness	Resistivity
Deposition time	Grain size

3.2.2.1 Flux Model Experimental Plan

Finally, based on the simulations results, experience of the manufacturer of magnetron sputtering equipment and the studies on this subject lead us to design of experiments (DOE). A viable two-staged experimental plan was built to characterize thickness and uniformity. At first stage (run order 1-12) only first order relations were considered at two level. In the second stage (Run 13-26) axial points of power, argon flow rate and pressure were taken into consideration. Baseline (BL) runs were included in order to observe the stability of the process. Details of this experimental plan for the first target (i.e. large target) as DOE1 is shown in Table 3.5. These runs were carried out on 6" substrates and copper (Cu) targets were used to deposit films. For the design of experiments (DOE) and analysis of the results JMP software was used. Other factors (morphology, adhesion etc.) will be characterized later with a different experimental design and tools.

Table 3.5 Target 1 experimental plan (DOE1).

Run Order	**DOE Pattern**	**Power (W)**	**Argon Flow (cm^3/min)**	**Pressure (mTorr)**
1	BL	300	115	6
2	DOE	500	200	10

Table 3.5 (continued)

3	DOE	500	200	2
4	BL	300	115	6
5	DOE	100	200	2
6	DOE	100	30	10
7	DOE	100	200	10
8	BL	300	115	6
9	DOE	500	30	10
10	DOE	100	30	2
11	DOE	500	30	2
12	BL	300	115	6
13	BL	300	115	6
14	DOE	300	30	6
15	DOE	300	200	6
16	DOE	500	200	6
17	DOE	500	115	6
18	BL	300	115	6
19	BL	300	115	6
20	DOE	300	115	6
21	DOE	300	115	10
22	DOE	300	200	2
23	DOE	100	115	6
24	DOE	300	115	2
25	DOE	500	115	2
26	BL	300	115	6

DOE2 plan was designed after the analysis of DOE1 results so that DOE2 included less experiments with the small target. DOE1 results showed the important interactions between power, argon flow rate and pressure. Therefore, in the design of DOE2 only the important factors, second degree interaction of power, argon flow rate and pressure

were included. Besides, BL experiments were also done to track stability as in the case of DOE1. Details of the DOE2 which was designed for the processes with target 2 (i.e. small target) is shown in Table 3.6.

Table 3.6 Target 2 experimental plan (DOE2).

Run Order	**DOE Pattern**	**Power (W)**	**Argon Flow (cm^3/min)**	**Pressure (mTorr)**
1	BL	300	115	6
2	BL	300	115	6
3	DOE	100	200	10
4	DOE	500	200	10
5	DOE	100	30	10
6	DOE	500	30	2
7	BL	300	115	6
8	DOE	300	30	10
9	DOE	100	200	2
10	DOE	500	200	2
11	DOE	210	30	2
12	BL	300	115	6

DOE1 and DOE2 experiments were carried out with the moving substrate, in addition to these experiments, 2 additional experiments, one with target 1 and the other with target 2 at baseline conditions, were done to observe the static flux distribution on substrate. Static flux experimental results were used to validate static part of the model. Experimental conditions of these experiments are given in Table 3.7.

.

Table 3.7 Runcard of stationary substrate experiments.

Target	DOE Pattern	Power (W)	Argon Flow (cm3/min)	Pressure (mTorr)	Process Time (min)
1	BL	300	115	6	6
2	BL	300	115	6	6

3.2.2.2 Thermal Model Experimental Plan

This part devoted to the experimental plans designed to be the basis of the thermal model. Substrate temperature is affected from deposition time, power, and working gas pressure during deposition processes. Heater also used in the system to increase the substrate temperature prior to deposition and during the deposition to preserve the substrate temperature when the substrate oscillates under the target. Therefore, thermal model experiments can be divided into two parts as those for characterizing substrate temperature during deposition processes and those for the heater characterization. The experiments were carried out at three power level since power is the most important parameter that affects the heating of the substrate and the details of the experiments are given in Table 3.8. The all experiments were desired to complete in a dynamic fashion that is with oscillating substrate, however, thermocouples attached to the system did not allow this. Therefore experiments were done with the fixed substrate under the target and there was also one dynamic data taken successfully which allowed us to predict the dynamic temperature profile in the substrate.

Table 3.8 Experimental conditions for the substrate temperature characterization during sputtering process.

Run Order	Target	Pass	Power (W)	Argon Flow (cm^3/min)	Pressure (mTorr)
1	1	Fixed	100	30	2
2	1	Fixed	300	115	6
3	1	Fixed	500	200	10
4	2	Fixed	100	30	2
5	2	Fixed	300	115	6
6	2	Fixed	500	200	10

For the heater characterization experiments a four-step experimental design was created, power inputs of the heaters were increased by two percent at each step. Since, there are six heaters in the system, experiments are done to for each heater. Experimental conditions is given in Table 3.9 and typical power input for the heaters is shown in Figure 3.15.

Table 3.9 Experimental conditions for the substrate temperature characterization during heating process.

Heater	Pass	Power (W)
1	Fixed	Four-stage power increase with 2% step
2		
3		
4		
5		
6		

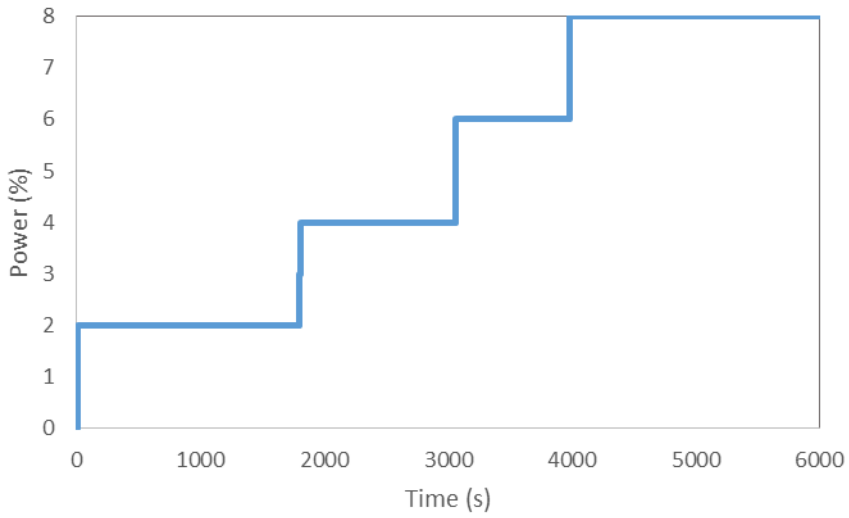

Figure 3.15 Typical power (%) input profile for the heater characterization experiments.

CHAPTER 4

RESULTS AND DISCUSSION

In this section firstly the results of the experiments described in the empirical modeling section is given since results of these experiments are to support the theoretical and empirical models of the sputtering system. Secondly, results of the modeling studies for both flux and thermal models are given. Moreover, the results of the theoretical models are discussed and compared with the experimental results.

Empirical modeling section results includes two parts, since two size Cu targets were used for the thickness uniformity optimization and stationary substrate experiments. Therefore, in the first part thickness and thickness uniformity results for the target 1 and 2 are given and then thickness profile results for the thin films sputtered at fixed position under the target are given. In the second part modeling findings are given in two parts which are flux and thermal model results. As outlined in the modeling section, there are one modeling approach to find the effect of geometrical parameters on uniformity and growth rate of the thin films namely flux model and others are thermal modeling approaches to find substrate temperature distribution during the sputtering and heating processes. Thermal model results are given and compared with the real temperature data collected from the system for both ANSYS finite element and MATLAB simplified approach.

4.1 Empirical Modeling

4.1.1 Target 1 Results

As planned, experiments outlined in Table 3.5 and Table 3.6 were carried out for both large and small targets. Critical outputs of this study was to satisfy the substrate uniformity and characterize the thickness in terms of sputtering process conditions. A typical thickness distribution and resistivity profile from the DOE1-Run3 is given in Figure 4.1. Percent standard deviation of the film was found as 1.4. Moreover, it was seen that film showed random thickness profile. Knowing the fact that resistivity of the films inversely proportional to thickness and resistivity profile of the film was consistent with the thickness profile.

Thickness profile	Resistivity profile
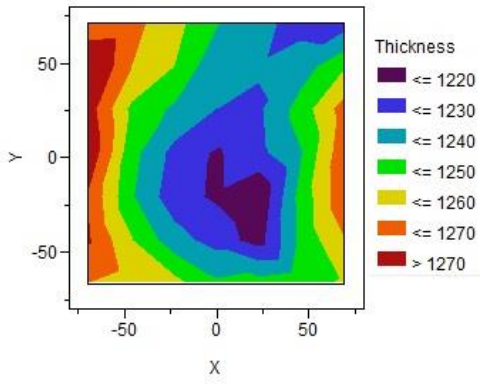	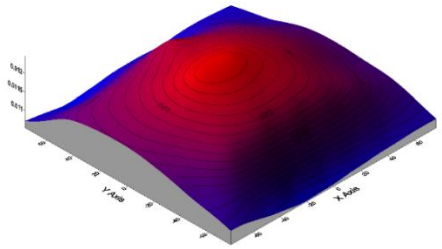

Figure 4.1 Thickness and resistivity profile for DOE1-Run3.

DOE1-Run3 showed the best results in DOE1 experiments and thickness results of the other executed experiments are given in Figure 4.2 and uniformity results of the experiments, defined with % standard deviation are given in Figure 4.3. In order to track the stability of the experiments, experiments with the baseline condition were

also planned in DOE1. According to the results it was found that stability of the system, except one of the experiments, was satisfactory. This means thickness of the films was in the range of 100 - 125 nm. Difference found in DOE1-Run13 was related to the warm-up problem of the system, after analyzing the log data of the sputtering chamber, it was seen that during process power was inadequate.

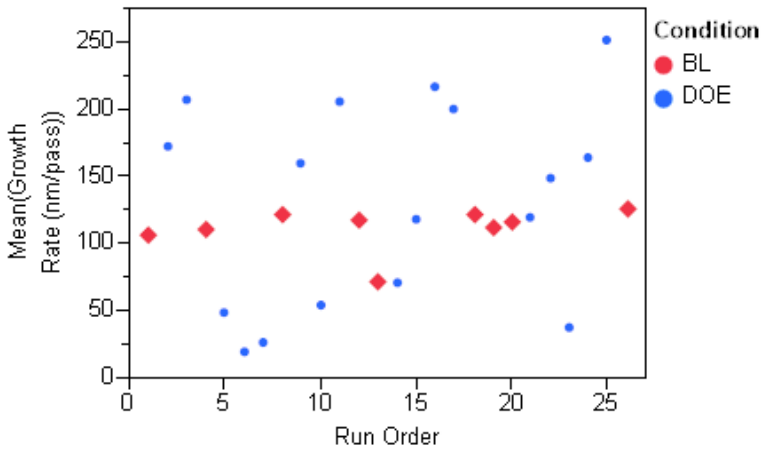

Figure 4.2 Change of growth rate (nm/pass) of films sputtered with large Cu target for different experimental conditions.

In Figure 4.3, it is seen that uniformity is improving with the experiments according to the results of the time paired baseline runs. This improvement was related to the race track formation on the targets. In magnetron sputtering method, race track like shape is formed on target as a result of magnets used behind the targets. Magnets tracks electron near the target surface, therefore targets are mostly diminished from these regions. The effect of race track is similar to target to substrate separation, improvement in the race track results in more uniform films on substrate. Therefore, trend in percent standard deviation was agreeable.

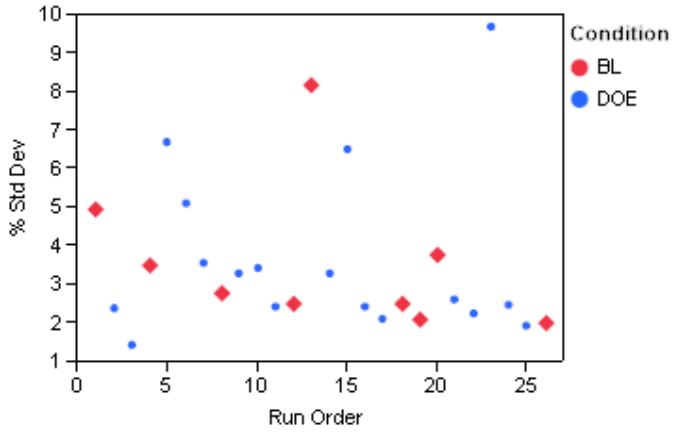

Figure 4.3 %Standard deviation of films sputtered with large Cu target for different experimental conditions.

After completing DOE1 and obtaining the results multiple regression analysis with the argon flow rate, power and pressure was examined so results of the experiments were introduced into the regression model by using JMP software. Based on the analysis for the thickness of the films, actual versus predicted plot was created which is shown in Figure 4.4 and R squared value of mean thickness is found as 0.93, which means data points fit to the model well. Parameters estimates given in Table 4.1, analysis showed that power and pressure are the most important parameters of sputtering process when mean thickness is considered prediction formula of mean thickness based on the important parameters are given in Equation 4.1 for target 1.

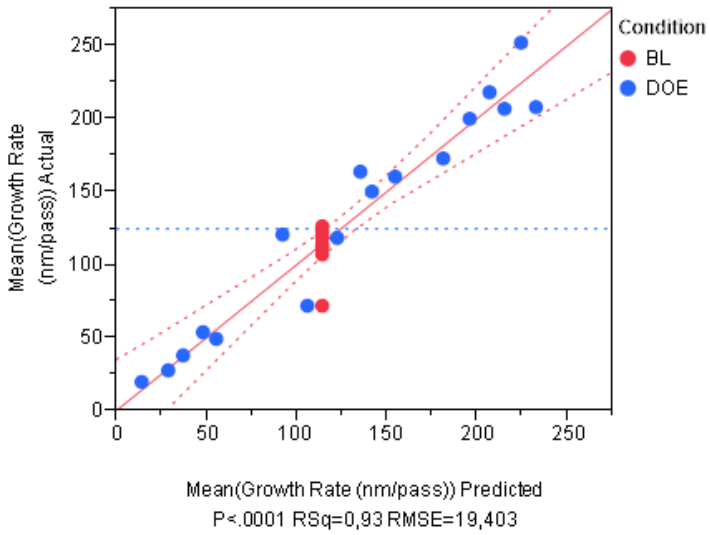

Figure 4.4 Actual by predicted plot of mean growth rate for large Cu target

Table 4.1 Parameter estimates - Growth rate

Sorted Parameter Estimates

Term	Estimate	Std Error	t Ratio		Prob>|t|
Power	0,4029285	0,028435	14,17		<,0001*
Pressure	-5,469206	1,416419	-3,86		0,0011*
Argon Flow	0,0962951	0,066655	1,44		0,1657
(Power-315,385)*(Pressure-5,69231)	-0,00814	0,008181	-0,99		0,3329
(Power-315,385)*(Argon Flow-121,538)	0,0001566	0,000385	0,41		0,6889
(Argon Flow-121,538)*(Pressure-5,69231)	0,0061763	0,019248	0,32		0,7520
(Power-315,385)*(Power-315,385)	0,000056	0,000193	0,29		0,7754

Prediction formula for the mean growth rate of the film is given below;

$$\text{Mean Growth Rate}: 15.25 + 0.4 \times \text{Power} + 0.096 \times \text{Argon Flow} - 5.47 \times \text{Pressure} \quad (4.1)$$

Regression analysis for uniformity of the films was also executed with the parameters argon flow rate, power and pressure. Based on the analysis for the uniformity, actual versus predicted plot was created which is shown in Figure 4.5 and R squared value of % standard deviation regression was found as 0.62, which means predicting the

uniformity is difficult compared to predicting the thickness of the films. Parameters estimates are given in Table 4.4 and results showed that power is the most critical parameter for the thickness uniformity of the films. Prediction formula for the % standard deviation is given in Equation 4.2.

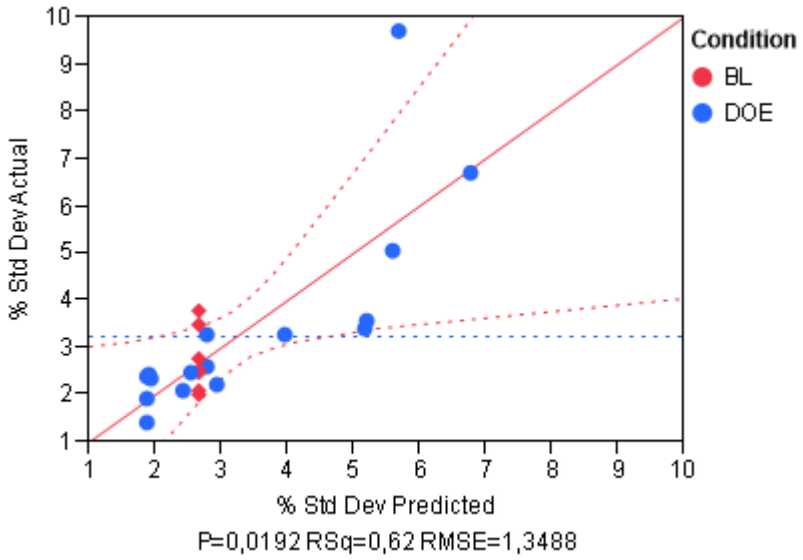

Figure 4.5 Actual by predicted plot of % standard deviation for large Cu target

Table 4.2 Parameter Estimates - % Standard deviation

Sorted Parameter Estimates

Term	Estimate	Std Error	t Ratio	Prob>|t|
Power	-0,007225	0,001992	-3,63	0,0025*
(Power-317,391)*(Power-317,391)	0,0000346	1,428e-5	2,42	0,0285*
(Argon Flow-118,696)*(Pressure-5,65217)	-0,001483	0,001341	-1,11	0,2860
(Power-317,391)*(Pressure-5,65217)	0,0005138	0,000569	0,90	0,3805
(Power-317,391)*(Argon Flow-118,696)	-2,346e-5	2,677e-5	-0,88	0,3947
Pressure	0,0337436	0,098665	0,34	0,7371
Argon Flow	-0,001114	0,004831	-0,23	0,8207

Prediction formula for the % standard deviation of film thickness is given below;

$$\%\ \text{Standard Deviation} = 4.75 - 0.007 \times \text{Power} + (\text{Power} - 317.4)^2 \times 0.000035 \quad (4.2)$$

Prediction profiler of the JMP was used to understand the effect of argon flow, power and pressure on mean growth rate and % standard deviation. Prediction profiler plots for the mean thickness and % standard deviation are given in Figure 4.6 and these results indicated that for the thickness and uniformity purposes one should use maximum power, minimum pressure and a moderate argon flow rate for optimum film thickness and uniformity. Moreover, mean growth rate is directly related with power and argon flow, however it is inversely proportional with the pressure. On the other hand, % standard deviation showed different characteristics compared to mean growth rate. It was found that uniformity decreases with increase in power and slightly increases with decrease in argon flow rate and pressure.

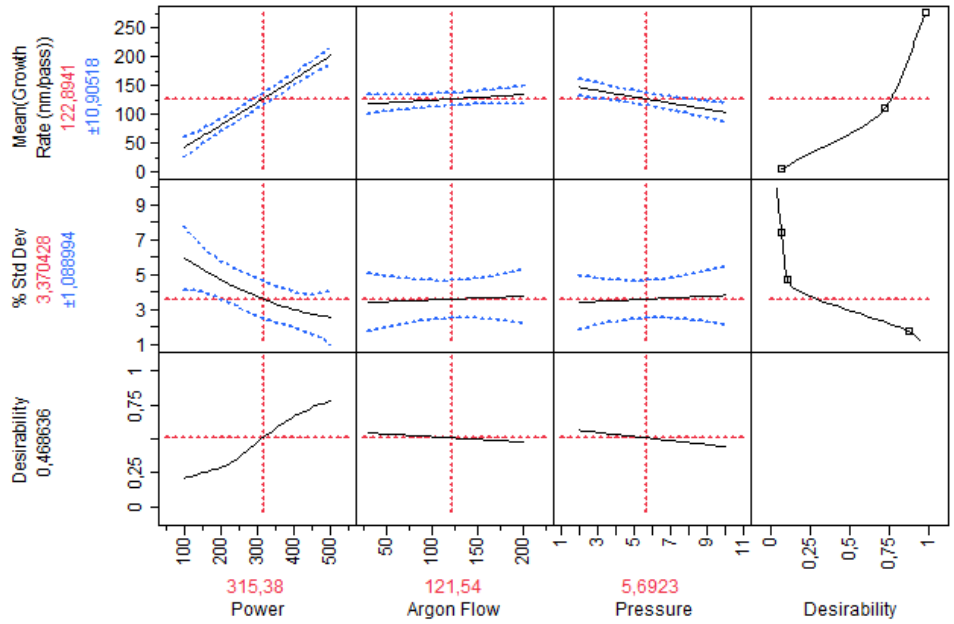

Figure 4.6 Prediction profiler to estimate the mean thickness and % standard deviation for films sputtered with large Cu targets

4.1.2 Target 2 Results

Small Cu target (target 2) with a mask were used to predict the behavior of the gold (Au) target. This mask was specially designed by VAKSİS in order to increase the uniformity in the films coated with the small target. A smaller target with a mask was designed for gold since gold is a very expensive material the aim was to decrease the target usage in other words decrease the cost of the target by decreasing the size of the target. Therefore, Cu targets were used to characterize the behavior of the Au target since their sputtering yields are very close, using Cu as substitute for gold was feasible. In the design of second experimental plan, experience from the DOE1 was used since target 1 and target 2 were both composed of Cu. Important factors was determined by analyzing the DOE1 results. Therefore, for DOE2 one stage experiment with important factors, second-order relations of power, pressure and argon flow rate, was designed which means target 2 was characterized by performing less experiments.

As seen in Figure 4.7 , thickness profile was different for the films sputtered with the small target. It was expected that uniformity will be lower for these coatings due to use of small size target and mask. However, for the region between -50 mm and 50 mm on the wafer results indicated that presence of mask enhances thickness uniformity in this region. Percent standard deviation of the films sputtered with target 2 was for DOE1-Run1 case was found as 30 %. Since DOE2 experiments were carried out with a smaller target, thickness non-uniformity was expected to be higher when compared to large target. Although uniformity was low for the target 2, it can still be used to deposit thin films. Because experiments were carried out with 6" substrates, however the primary substrate size in this laboratory is 4". This means using target 2 for the deposition of 4" substrates was feasible, because thickness non-uniformity was smaller for a 4" square region.

Thickness profile	Resistivity profile
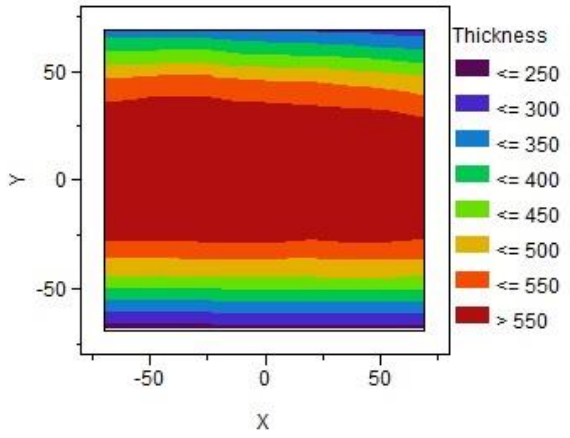	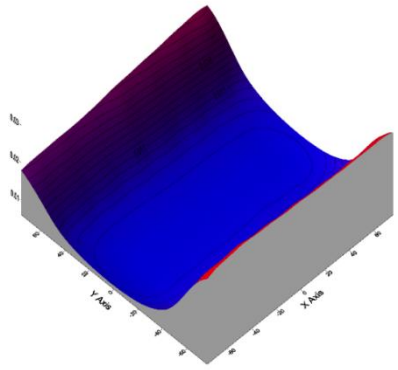

Figure 4.7 Thickness and resistivity profile for DOE2-Run1.

DOE2 experiments was designed as 12 run experiment with 4 run at baseline conditions. Results of all DOE2 experiments are given in Figure 4.8 and uniformity results of the experiments, defined with % standard deviation are given in Figure 4.9. According to the results, it was seen that sputtering system was stable during sputtering experiments so that a regression analysis was done using these results.

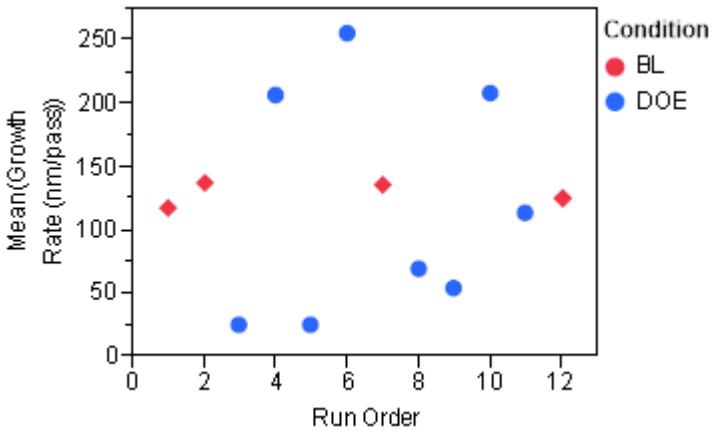

Figure 4.8 Change of growth rate (nm/pass) of films sputtered with target 2 for different experimental conditions.

In Figure 4.9, it is seen that uniformity changes with the experiments according to the results of the time paired baseline runs. The uniformity improvement in target 1 was related to the race track formation on the targets, however in target 2 race track formation was not distinct so clear trend of improvement was not seen in DOE2 uniformity results.

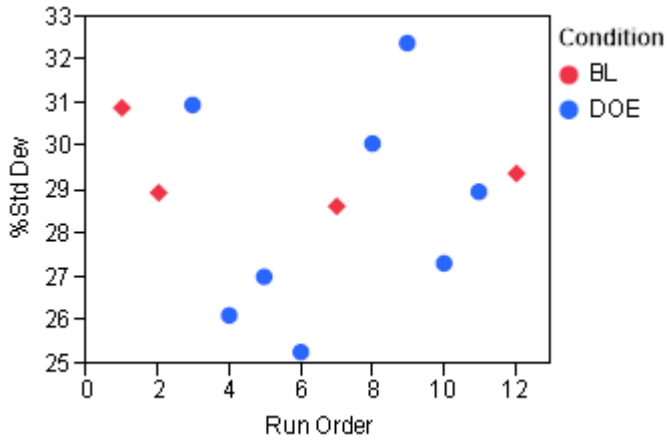

Figure 4.9 Change of percent standard deviation of thickness of the films.

After completing DOE2, multiple regression analysis with the argon flow rate, power and pressure was studied so thickness measurements and % standard deviation of these measurements were introduced into the regression model by using JMP software. Based on the analysis for the thickness of the films, actual versus predicted plot was created which is shown in Figure 4.10 and R squared value of mean thickness is found as 0.98, which means thickness can be predicted well with this prediction formula given in Equation 4.3. Parameters estimates given in Table 4.3, analysis showed that power and pressure are the most important parameters of sputtering process when mean thickness is considered.

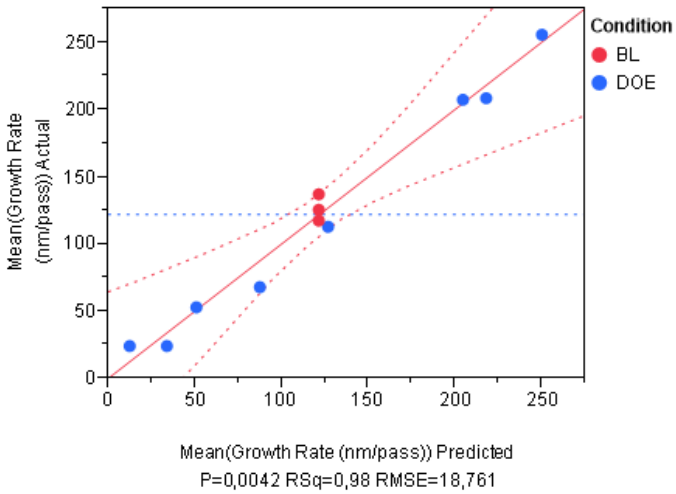

Figure 4.10 Actual by predicted plot of mean growth rate (nm/pass) for the films sputtered with target 2.

Table 4.3 Parameter estimates - Growth rate.

Sorted Parameter Estimates

Term	Estimate	Std Error	t Ratio	Prob>|t|
Power	0,4125065	0,044797	9,21	0,0008*
Pressure	-5,55589	1,827002	-3,04	0,0384*
(Argon Flow-115)*(Pressure-6)	0,0430622	0,021635	1,99	0,1174
(Power-292,5)*(Power-292,5)	0,000193	0,000331	0,58	0,5907
Argon Flow	-0,031967	0,091856	-0,35	0,7454
(Power-292,5)*(Argon Flow-115)	7,8719e-5	0,000529	0,15	0,8889
(Power-292,5)*(Pressure-6)	0,0010903	0,010986	0,10	0,9257

Prediction formula for the mean growth rate of the film is given below;

$$\text{Mean Growth Rate} = 34.95 + 0.41 \times \text{Power} - 5.55 \times \text{Pressure} \qquad (4.3)$$

In addition to the regression analysis for thickness was also performed to predict uniformity of the films with the parameters argon flow rate, power and pressure. Based on the analysis for the uniformity, actual versus predicted plot was created which is shown in Figure 4.11 and R squared value of % standard deviation was found as 0.89, which means predicting the uniformity is easier compared to predicting the thickness

of the films. Parameters estimates are given in Table 4.4 and results showed that power is the most critical parameter for the thickness uniformity of the films. Prediction formula for the % standard deviation is given in Equation 4.4.

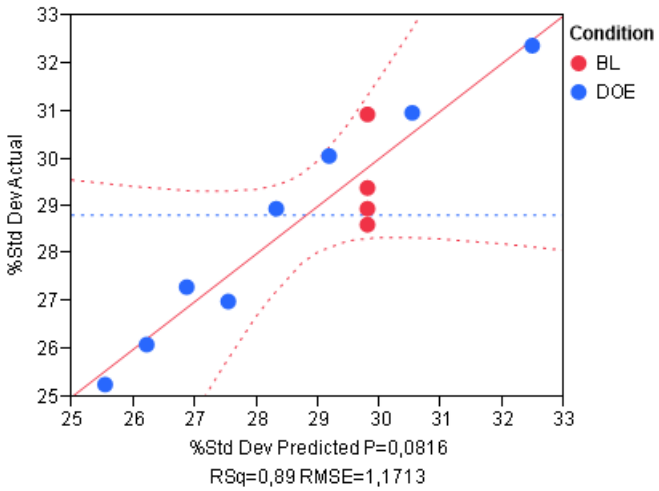

Figure 4.11 Actual by predicted plot of %standard deviation for target 2.

Table 4.4 Parameter estimates- % standard deviation.

Sorted Parameter Estimates

Term	Estimate	Std Error	t Ratio	Prob>|t|
Power	-0,006891	0,002797	-2,46	0,0694
Argon Flow	0,013077	0,005735	2,28	0,0848
(Power-292,5)*(Power-292,5)	-4,682e-5	2,064e-5	-2,27	0,0858
(Power-292,5)*(Argon Flow-115)	-5,632e-5	0,000033	-1,71	0,1632
(Argon Flow-115)*(Pressure-6)	-0,001602	0,001351	-1,19	0,3011
(Power-292,5)*(Pressure-6)	0,0004022	0,000686	0,59	0,5891
Pressure	-0,030164	0,114068	-0,26	0,8045

Prediction formula for the % standard deviation of the film thickness is given below;

$$\%\ \text{Standard Deviation} = 30.56 - 0.007 \times \text{Power} + 0.013 \times \text{Argon Flow} - (\text{Power} - 292.5)^2 \times 0.00005 \qquad (4.4)$$

Prediction profiler of the JMP was again used to understand the effect of argon flow, power and pressure on mean growth rate and % standard deviation for the analysis of DOE2 experiments. Prediction profiler plots for the mean thickness and % standard deviation are given in Figure 4.12 and these results indicated that for the thickness and uniformity purposes one should use maximum power, because it was seen that for lower power values % standard deviation of the thickness was high so power must be kept above 300 watts while sputtering with target 2. Moreover, low argon flow rate would be useful for optimum film thickness and uniformity. It was also found that pressure of the chamber was less critical on thickness uniformity than as in the case of target 1.

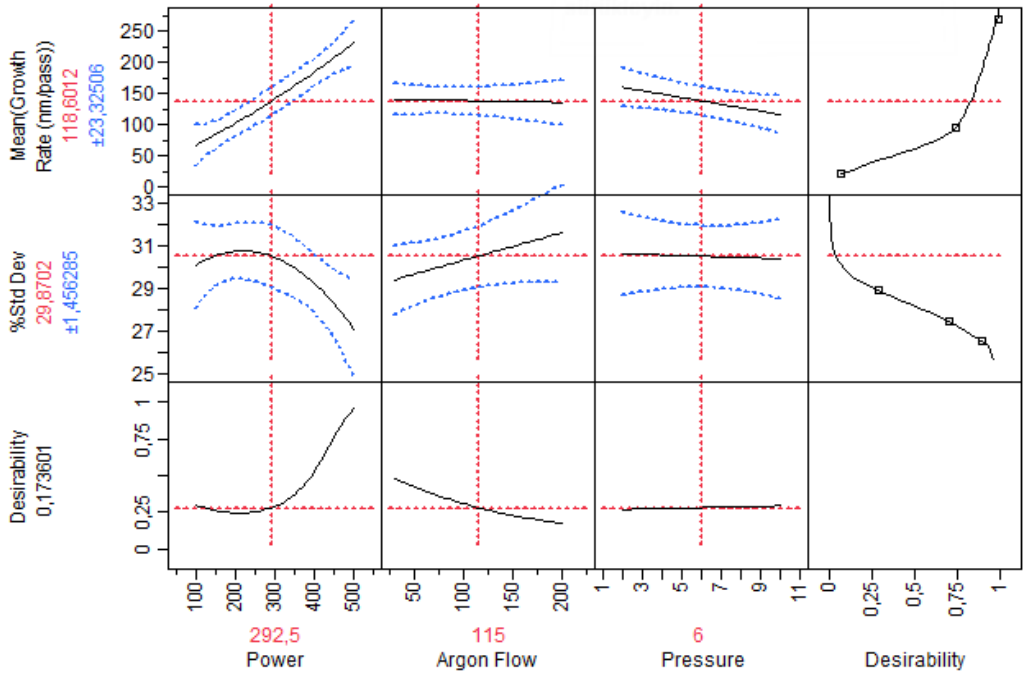

Figure 4.12 Prediction profiler to estimate the mean thickness and % standard deviation for films sputtered with target 2.

4.1.3 Stationary Substrate Experiments

This section describes the results of the stationary substrate experiments which aims to find out the thickness distribution of the film when there is no substrate movement. Thickness profile of the film sputtered with target 1 at the baseline conditions are shown in Figure 4.13. When the race track formation on target 1 surface which can be seen in Figure 4.15, thickness distribution of the film was consistent. The reason was targets were highly utilized from race track regions so thickness was higher closer to these regions of the target 1. Since more experiments were performed with target 1 and target 1 was larger than target 1, race track area was larger and more effective on the sputtered films.

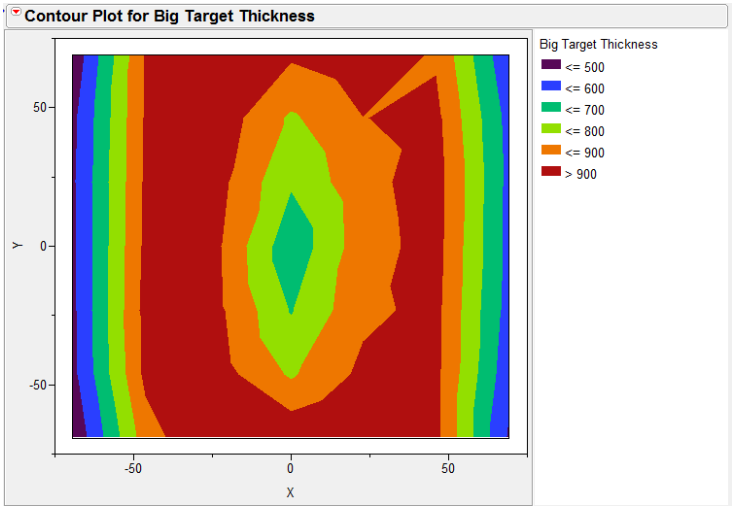

Figure 4.13 Thickness profile for films coated with target 1 at baseline conditions

In Figure 4.14 thickness distribution for target 2 is given, and it was seen that effect of race track on thickness profile of the films was not clearly observed. This can be explained by two reason, first of all, race track area was small with the target 2 and secondly mask eliminates the effect of race track on the thickness distribution of the

films. The results of these two experiments were used to support the flux model for target 1 in order to include the effect of race track.

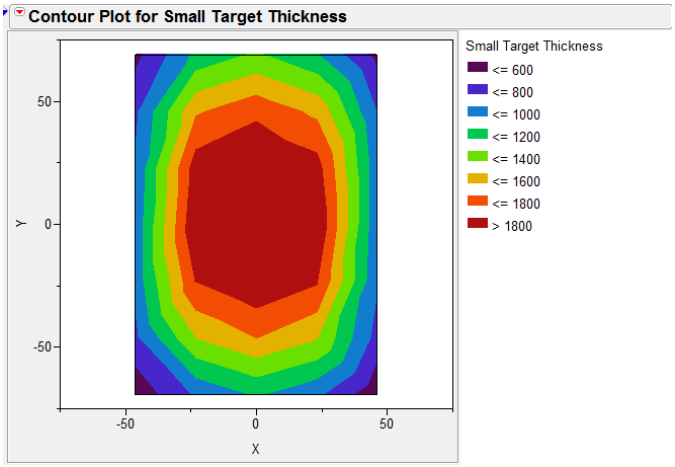

Figure 4.14 Thickness profile for the films coated with target 2 at baseline conditions.

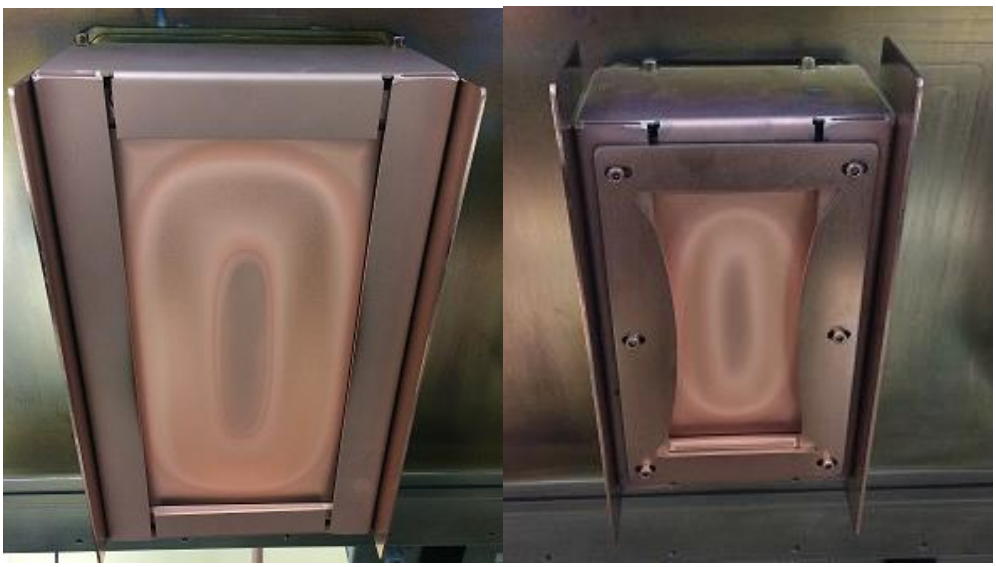

Figure 4.15 Race track formation on the target 1 (left) and target 2 (right) surface.

4.1.4 Thermal Analysis-Substrate Temperature Measurements

Substrate surface temperatures are obtained while coating under target 1 and 2. The plan is shown in Table 3.8. The experiments were carried out at three power level since power is the most important parameter that affects the heating of the substrate. As expected before conducting the experiments temperature increase of substrate surface was directly related to the power input. Slopes were calculated by using the temperature profile of the substrate surface in order to observe the power-temperature relation.

Figure 4.16 and Figure 4.17 shows the temperature profile at baseline conditions for the deposition under target 1 and target 2 and summary of the all results are given in Table 4.5. As it is seen from the temperature profiles and temperature uniformity calculations small target has large deviations under the target. The reason is that substrate width is larger than the small target so that some part of the substrates were not coated while experimenting with the small target. Therefore, heat flux was variable on top of the substrate, however for the large target, temperature non-uniformity was small.

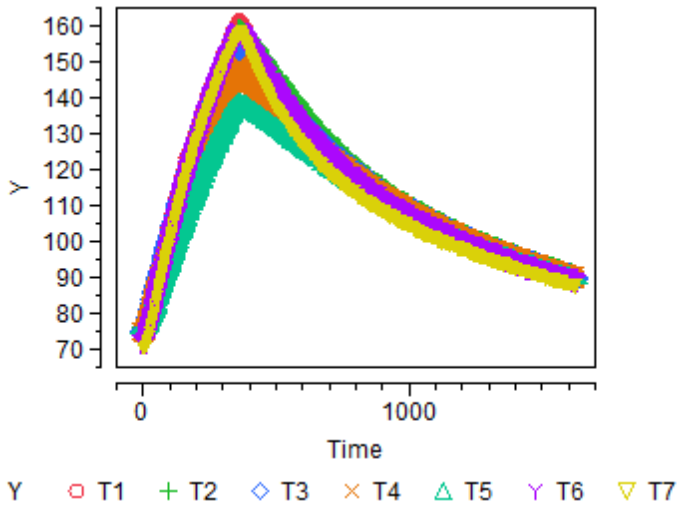

Figure 4.16 Temperature profile during deposition under target 1 at baseline conditions.

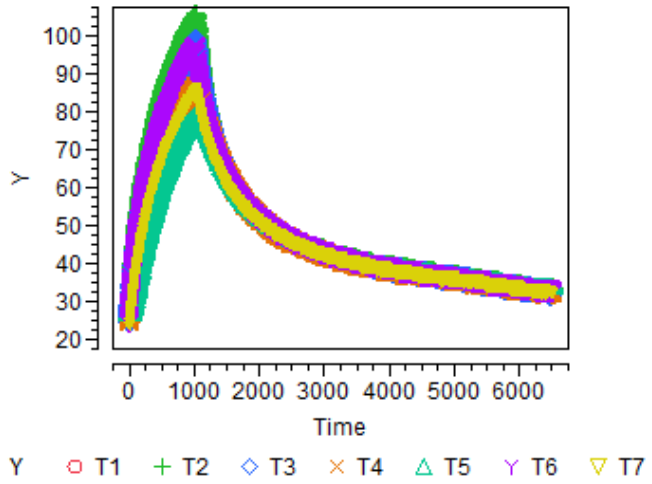

Figure 4.17 Temperature profile during deposition under target 2 at baseline conditions.

Table 4.5 Results of substrate surface temperature experiments.

Run Order	**Average Temperature**	**Temperature Uniformity**	**Slope($\frac{\Delta T}{\Delta t}$)**	**q" (W/cm^2)**
1	112.1	9.5	0.10	0.017
2	154.55	14.99	0.24	0.040
3	164.86	16.17	0.41	0.069
4	91.23	29.28	0.11	0.018
5	141.33	44.56	0.28	0.047
6	142.94	52.86	0.57	0.095

4.2 Modeling Results

In previous chapters, details of the MATLAB and ANSYS models are shared. In this final result part, model results is compared with experimental results and contribution of experimental findings on modeling is explained. Firstly results of the flux model is given for target 1 and target 2. Secondly results of thermal models created to characterize the substrate temperature distribution is given.

4.2.1 Flux Model

4.2.1.1 Target 1 Modeling Results

In this part experimental and real thickness distribution is compared for target 1. Static flux distribution from target 1 is given in Figure 4.18. This distribution was obtained from the MATLAB by using the stationary substrate experiment results. Experimental results were used because use of cosine law was not proper for target 1. The reason of this was effective race track formation on target 1, however cosine law was used for the ideal case of deposition from a clean, uniformly emitting point source on to a substrate. Therefore, experimental findings were used to consider the effect of non-uniform emitting target. In Figure 4.19 experimental thickness profile and thickness profile obtained from the MATLAB code are given in the same plot. The plot shows the normalized center thicknesses of the films for comparison purposes.

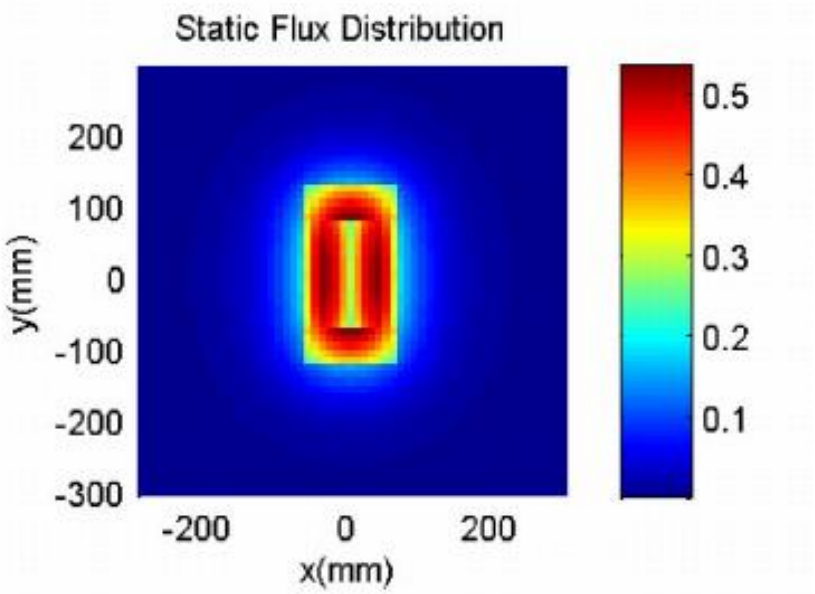

Figure 4.18 Static flux distribution from the target 1.

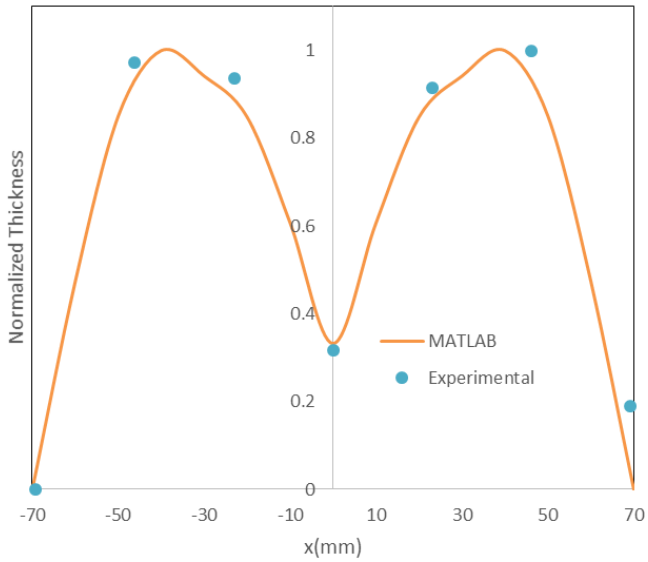

Figure 4.19 Comparison of normalized experimental and MATLAB thickness distribution.

In Figure 4.20, predicted contour plot for the deposition under target 1 is given. Experimental results was showed that there is random distribution of thickness while sputtering with the target 1, however according to the MATLAB results based on cosine law, thickness of the films thicker on the center and thinner at the edge of the substrate.

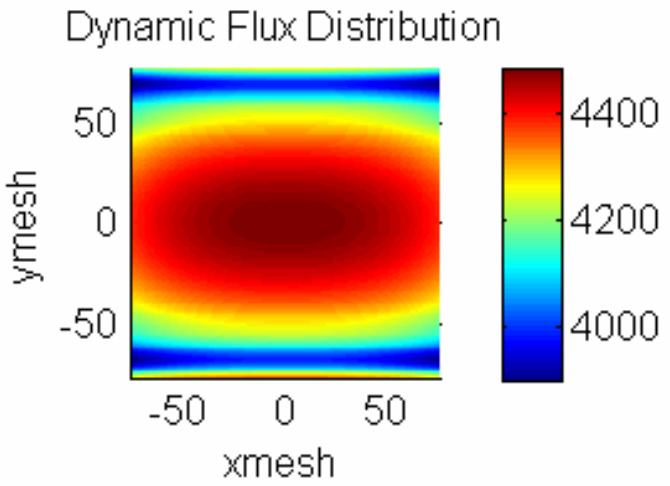

Figure 4.20 Predicted contour plot for the deposition under target 1.

Predicted values of thickness uniformity and target usage and important parameters used in simulations are summarized in Table 4.6. When experimental and theoretical findings was compared for target 1, it was found that theoretical approach was not good at predicting the thickness distribution for large target (target 1). Moreover, percent uniformity value which is % 3.6 also highly deviates from the real uniformity value of % 5.7.

Table 4.6 MATLAB Simulation parameters and outputs for target 1

Parameters\Outputs	Value
Target Usage (%)	13.4
Thickness Uniformity (%)	3.6
Substrate Velocity[mm/s]	3.33
Target Size [mm]	125 by 250
Target to Substrate Distance [mm]	70
Movement Limit [mm]	200

4.2.1.2 Target 2 Modeling Results

In this part experimental and real thickness distribution is compared for target 2. Static flux distribution from target 1 is given in Figure 4.21. Since race track formation was not effective on the target 2, static flux distribution was changed by using the experimental results. In Figure 4.20 contour plot based on the MATLAB simulations is given for target 2 which shows good agreement with the experimental contour plot.

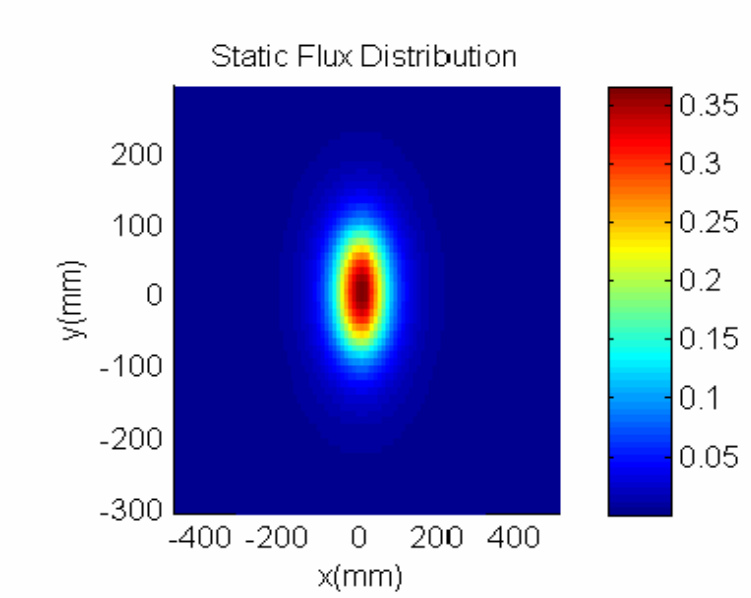

Figure 4.21 Static flux distribution from the target 2.

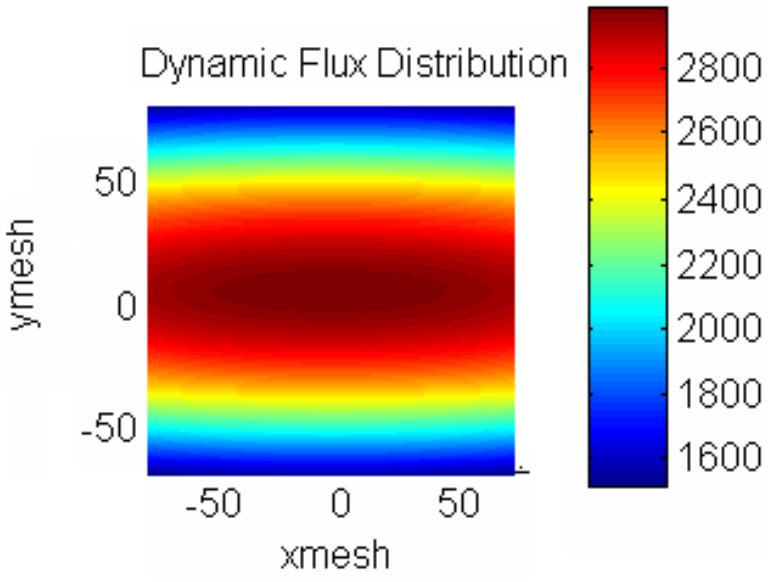

Figure 4.22 Predicted contour plot for the deposition under target 2.

Predicted values of thickness uniformity and target usage and important parameters in simulations for target 2 used are summarized in Table 4.7. Although, model for target 2 was better for predicting thickness distribution, percent thickness uniformity value of % 18.1 deviates from the real value of % 29.

Table 4.7 MATLAB Simulation parameters and outputs for target 2.

Simulation Parameters\Outputs	**Value**
Target Usage (%)	25.3
Thickness Uniformity (%)	18.1
Substrate Velocity[mm/s]	3.33
Target Size [mm]	125 by 75
Target to Substrate Distance [mm]	70
Movement Limit [mm]	200

According to the result of experiments, it was found that at all conditions thickness distribution was the same for the small target and uniformity is low. On the other hand, for the large target (target 1) random distribution was observed which is shown in Figure 4.23. The reason of this that the presence of mask influences the plasma distribution while depositing with the small target (target 1). After completing experiments, it was found out that the model was capable of predicting thickness distribution better for small target. One of many results can be seen in Figure 4.24 for target 2. However, model created for target 1 and target 2 was not good at predicting the thickness uniformity of the films. For this purpose, this model was mainly used to understand the effect of geometrical parameters on thickness uniformity and target usage. Therefore model was used to design experiments and to support empirical modeling. Details of this study are given in how to eliminate geometrical factors section in Chapter 3. Comparison between empirical and theoretical studies showed that model should be improved for better estimations of thickness uniformity for both target 1 and target 2.

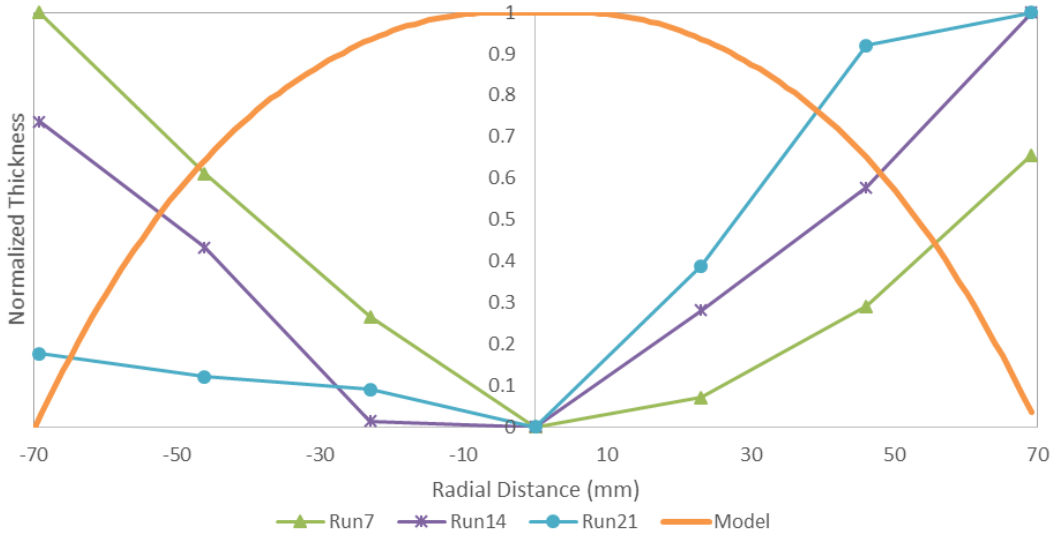

Figure 4.23 Comparison of normalized experimental thickness with model predictions for target 1.

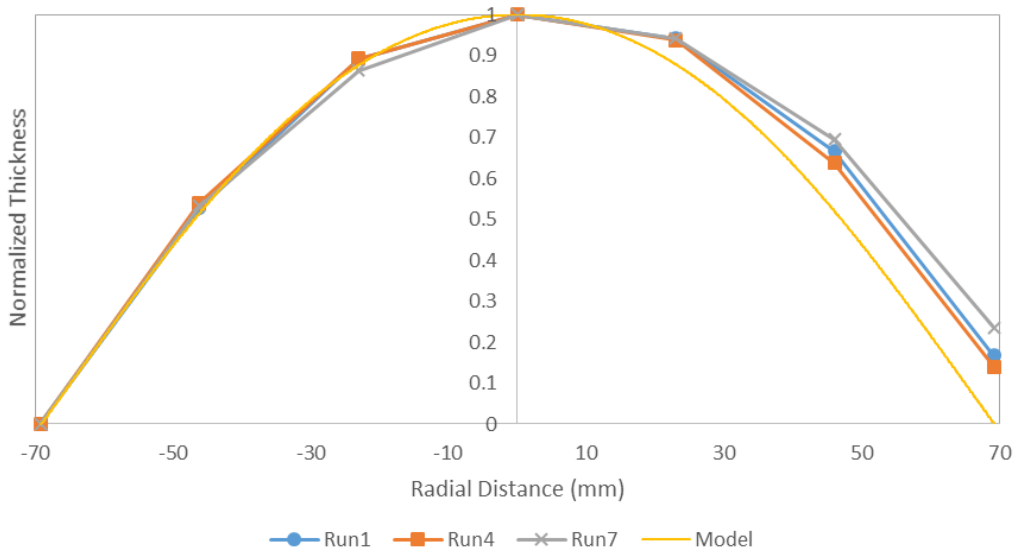

Figure 4.24 Comparison of normalized experimental thickness with model predictions for target 2.

4.2.2 Thermal Model

4.2.2.1 ANSYS Heater Results

Finite element model in the ANSYS is defined with some geometrical simplifications of the chamber and the parts inside the chamber. Figure 4.25 below shows the comparison of model predictions vs real experimental for the substrate temperature with respect to time.

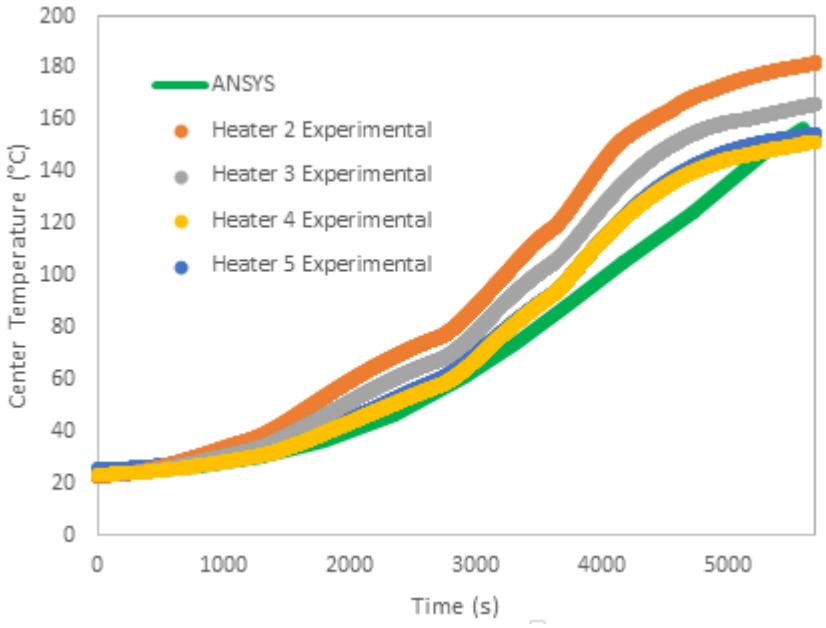

Figure 4.25 ANSYS vs experiments (small heaters).

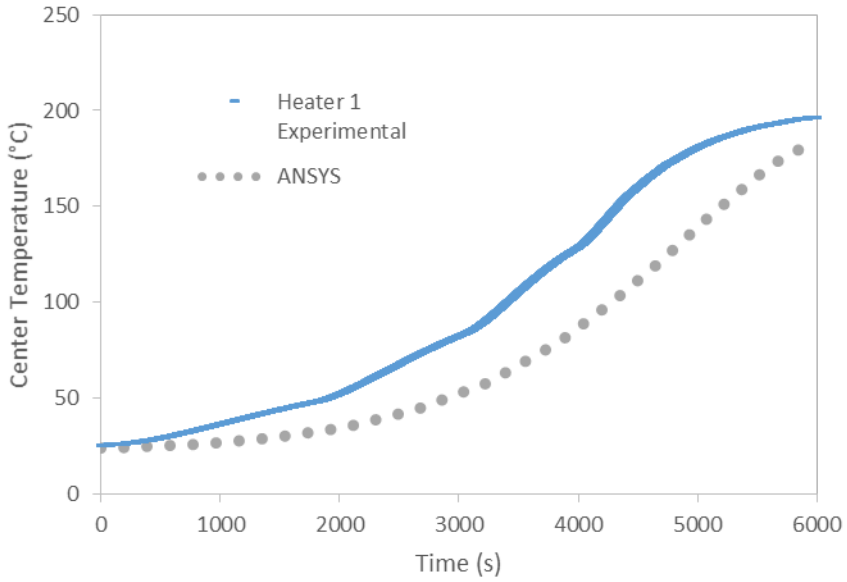

Figure 4.26 ANSYS vs experiments (large heater 1).

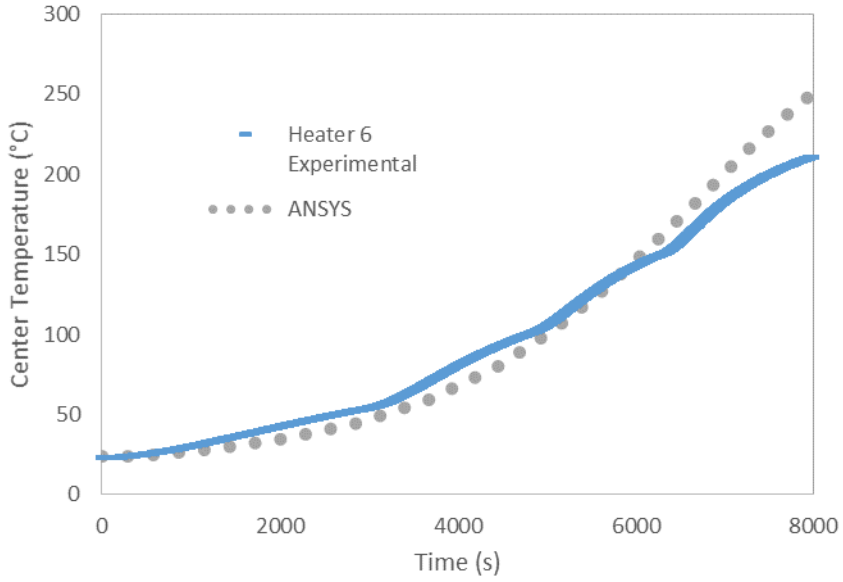

Figure 4.27 ANSYS vs experiments (large heater 6).

Even heater 2, 3, 4 and 5 are identical and experimental conditions for these heaters are the same, their temperature dynamics are expected to be the same. However, substrate temperature changes heater to heater. In order to explain this situation,

surface temperature of heaters were measured by using an external thermocouple and it was seen that the temperatures taken from the surface by the thermocouple embedded in the system and the external one showed different surface temperatures which is shown in Table 4.8. Measurements were taken from 7 points on the heater surface. Difference in surface temperature of large heaters was nearly 50° C, therefore time to reach maximum substrate temperature for the heater 1 was nearly 6000 seconds while with the heater 6 it was 8000 seconds. Therefore, for the same power input, heaters output can be different. The reason behind that heaters properties are not completely the same although aiming to manufacture identically. They are composed of special materials and the surface of the heater is stainless steel so after performing experiments the surface changes. Another problem with the thermocouple embedded in the system may be that it is calibrated by the manufacturer of the chamber. Therefore their thermocouples may not be temperature sensitive at desired level. ANSYS model need to be fined tuned for all heaters separately. Since emissivity of the heaters changes with respect to temperature and material surface, emissivity of the parts can be adjusted to capture the temperature profile better. Output of ANSYS simulations are given in Appendix B for large and small heaters.

Table 4.8 Surface temperature of small heaters.

Heater No.	**P1**	**P2**	**P3**	**P4**	**P5**	**P6**	**P7**
2	198	205	219	198	226	210	185
3	218	208	226	226	221	218	205
4	206	199	198	184	210	185	203
5	205	203	200	220	193	195	201

Table 4.9 Surface temperatures of large heaters.

Heater No.	P1	P2	P3	P4	P5	P6	P7	P8
1	260	260	258	256	278	288	308	295
6	210	208	205	212	205	196	210	207

4.2.2.2 MATLAB Dynamic Simulation Results

Figure 4.28 below shows the comparison of simplified MATLAB approach and actual center temperature. Model predictions for the substrate temperature is reasonably fit to the experimental results. Therefore, at a later stage of film characterization studies this model can be used to get approximate results for the substrate temperature during deposition. Since there is only one dynamic data of the system at the baseline conditions, flux calculated at baseline conditions is used for the MATLAB simulations. The calculated flux was 0.04 W/cm^2, in order to have a better fit with the experimental results, for the code flux was used as 0.048 W/cm^2.

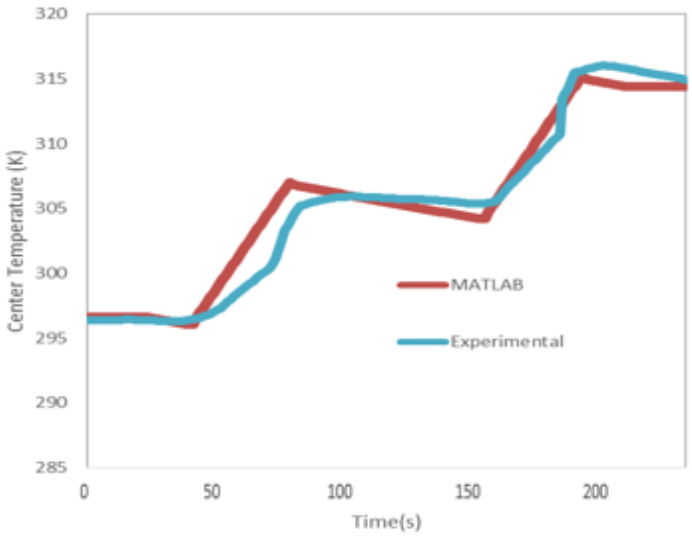

Figure 4.28 MATLAB vs experiments.

CHAPTER 5

CONCLUSIONS AND FUTURE WORK

5.1 Conclusion

In this thesis study, experimental and modeling work was implemented for the magnetron sputtering system. Since the first step of thin film manufacturing line is the PVD process, it is the most critical process. The modeling and experimental study of this thesis can be divided in to two parts as thermal and flux study. The main reason of the modeling studies was to decrease the number of experiments and to predict process conditions and outcomes at an early stage. Cosine law model built in MATLAB combined with the experimental studies allowed to eliminate some geometrical factors and reveal the critical parameters of the sputtering process.

ANSYS finite element, MATLAB simplified approach and the temperature characterization of experiments were convenient to predict the substrate temperature during deposition and prior to deposition. Thermal part of this study will be helpful when the properties of the film needed to optimized or improved for a specific process. Moreover, these experiments and modeling studies showed that although heaters are seemed to be identical, they give different results and stability of the system may change over time and needs to be tracked to have films that satisfies the requirements.

In addition to the modeling efforts, resistivity characterization study will be useful for the ease of thickness measurements during manufacturing operations.

5.2 Future Work

Further study will be carried on the modeling approach, model predictions will be improved for better agreement of modeling and experimental results. MATLAB model that predicts the substrate temperature will be developed to become more efficient so that it will be possible to obtain quick predictions of the thermal behavior of the substrate for real time applications. In addition, empirical modeling range can be expanded for power, argon flow rate and pressure. Then, process development for the other metal targets can be done based on the findings of the Cu target. Finally, prototype products will be produced with the completion of individual unit operations.

REFERENCES

[1] R. Thiyagarajan, M. Anusuya and M. M. Beevi, "Study of Structural and Mechanical properties of Zirconium Doped Cadmium Sulphide Thin Films", *J. Am Sci.*, vol. 5, no. 3, pp. 26–30, 2009.

[2] W. Kiyotaka, M. Kitabatake and H. Adachi, "Thin Film Materials Technology," 1st Ed., *William Andrew Publishing*, Heidelberg, 2004.

[3] M. Henini, " Book Review: Handbook of Thin-Film Deposition Processes and Techniques", *Microelectr J.*, vol. 31, no. 3., 2000.

[4] E. Fortunato, P. Barquinha and R. Martins, "Oxide semiconductor thin-film transistors: A review of recent advances", *Adv. Mater.*, vol. 24, no. 22, pp. 2945–2986, 2012.

[5] D. M. Mattox, "Handbook of Physical Vapor Deposition (PVD) Processing", 2nd Ed., *William Andrew Publishing*, United Kingdom, 2010.

[6] M. J. Madou, "Fundamentals of Microfabrication and Nanotechnology", 2nd Ed., *CRC Press*, USA, 2011.

[7] S. A. Campbell, "The Science and Engineering of Microelectronic Fabrication", 2nd Ed., *Oxford University Press*, USA, 2001.

[8] J. D. Plummer, M. D. Deal and P. B. Griffin, "Silicon VLSI Technology: Fundamentals, Practice and Modeling" 1st Ed., *Prentice Hall*, USA, 2000.

[9] K. Wasa, I. Kanno and H. Kotera, "Handbook of Sputter Deposition Technology: Fundamentals and Applications for Functional Thin Films, Nanomaterials, and MEMS", 2nd Ed., Elsevier, USA, 2012.

[10] Y. Kuzminykh, A. Dabirian, M. Reinke and P. Hoffmann, "High vacuum chemical vapour deposition of oxides: A review of technique development and precursor selection", *Surf. Coatings Technol.*, vol. 230, pp. 13–21, 2013.

[11] M. Ohring, "Materials Science of Thin Films", 2nd Ed., *Academic Press*, San Diego, CA, 2002.

[12] U. Helmersson, M. Lattemann, J. Bohlmark, A. P. Ehiasarian and J. T. Gudmundsson, "Ionized physical vapor deposition (IPVD): A review of technology and applications" *Thin Solid Films*, vol. 513, no. 1–2, pp. 1–24, 2006.

[13] J. Sarkar, "Sputtering Materials for VLSI and Thin Film Devices", 1st Ed., *Elsevier/William Andrew*, Amsterdam, 2014.

[14] S. Berg and T. Nyberg, "Fundamental understanding and modeling of reactive sputtering processes", *Thin Solid Films*, vol. 476, no. 2, pp. 215–230, 2005.

[15] C. Mack, "Fundamental Principles of Optical Lithography: The Science of Microfabrication", *Wiley*, USA, 2007.

[16] R. G. Polcawich and J. S. Pulskamp, "MEMS Materials and Processes Handbook: Additive Processes for Piezoelectric Materials: Piezoelectric MEMS", *Springer*, New York. 2011.

[17] G. Bräuer, B. Szyszka, M. Vergöhl and R. Bandorf, "Magnetron sputtering - Milestones of 30 years", *Vacuum*, vol. 84, no. 12, pp. 1354–1359, 2010.

[18] K. Ellmer, "Magnetron sputtering of transparent conductive zinc oxide: relation between the sputtering parameters and the electronic properties", *J. Phys. D. Appl. Phys.*, vol. 33, no. 4, pp. R17–R32, 2000.

[19] J. A. Thornton, "The microstructure of sputter-deposited coatings", *J. Vac. Sci. Technol. A Vacuum, Surfaces, Film.*, vol. 4, no. 6, pp. 3059, 1986.

[20] J. Stache, "Hybrid modeling of deposition profiles in magnetron sputtering systems", *J. Vac. Sci. Technol. A Vacuum, Surfaces, Film.*, vol. 12, no. 5, pp. 2867, 1994.

[21] K.Y. Chan and B. S. Teo, "Effect of Ar Pressure on grain size of magnetron sputter-deposited Cu thin films", *Sci. Meas. Technol. IET*, vol. 1, no. 2, pp. 87–90, 2007.

[22] K.-Y. Chan, T.-Y. Tou and B.-S. Teo, "Effects of substrate temperature on electrical and structural properties of copper thin films", *Microelectronics J.*, vol. 37, no. 9, pp. 930–937, 2006.

[23] S. Ayoub and L. Y. Beaulieu, "The surface morphology of thin Au films deposited on Si(001) substrates by sputter deposition", *Thin Solid Films*, vol. 534, pp. 54–61, 2013.

[24] M. T. Le, Y.-U. Sohn, J.-W. Lim and G.-S. Choi, "Effect of Sputtering Power on the Nucleation and Growth of Cu Films Deposited by Magnetron Sputtering," *Mater. Trans.*, vol. 51, no. 1, pp. 116–120, 2010.

[25] J. Krishnasamy, K. Y. Chan and T. Y. Tou, "Influence of process parameters on the substrate heating in direct current plasma magnetron sputtering deposition process", *Microelectron. Int.*, vol. 27, no. 2, pp. 75–78, 2010.

[26] K.-Y. Chan, T.-Y. Tou and B.-S. Teo, “Thickness dependence of the structural and electrical properties of copper films deposited by dc magnetron sputtering technique,” *Microelectronics J.*, vol. 37, no. 7, pp. 608–612, 2006.

[27] K. Y. Chan, P. Q. Luo, Z. Bin Zhou, T. Y. Tou and B. S. Teo, "Influence of direct current plasma magnetron sputtering parameters on the material characteristics of polycrystalline copper films", *Appl. Surf. Sci.*, vol. 255, no. 10, pp. 5186–5190, 2009.

[28] W. L. Prater, E. L. Allen, W. Y. Lee, M. F. Toney, A. Kellock, J. S. Daniels, J. A. Hedstrom and T. Harrell, "Microstructural comparisons of ultrathin Cu films deposited by ion-beam and dc-magnetron sputtering", *J. Appl. Phys.*, vol. 97, no. 9, 2005.

[29] A. F. Mayadas, M. Shatzkes and J. F. Janak, "Electrical-resistivity model for polycrystalline films the case of arbitary reflection at external surfaces", J.Appl. Phys. Letters, vol. 14, no. 11, 1969.

[30] S. Ghosal, R. L. Kosut, J. L. Ebert and L. L. Porter, "Multiscale modeling and control of RF diode sputter deposition for GMR thin films", Proc. ACC, vol.5, pp. 3930-3941, 2004.

APPENDICES

APPENDIX A MATLAB CODES

A.1 Flux Model M-Files

A.1.1 Main Program

```
clc;
clear all;
close all;


% Parameters
parameter = simulationinput;
H = parameter(1);
f = parameter(2);
Lt = parameter(3);
Wt = parameter(4);
delxt = parameter(5);
Ls = parameter(6);
Ws = parameter(7);
delxs = parameter(8);

subsspeed = 3.33; % Substrate velocity [mm/s];
delt = 0.1 ; % Time step size [s]
%movement = 100 ; %Movement extent in [mm];

x = (-Ws:delxs:Ws) ; %x and y for Static Flux Distribution Plot
y = (-Ls:delxs:Ls) ;

% Calculating Flux Distribution
fluxdist = Flux(Lt,Wt,delxt,Ls,Ws,delxs,H,f) ;

for delxs = [0.1]
    for movement = [10,25,50,100,150,200,300]
```

```
tic ;
% Substrate Movement

tfinal = 4*movement/subsspeed ;
xsubs = (-76.2:delxs:76.2) ;
ysubs = (-76.2:delxs:76.2) ;
tflux = zeros(length(xsubs),length(ysubs));
%XSUBS=[] ;
emitted=0 ;
deposited=0;

for t = 0:delt:tfinal;

    if  t<tfinal/4

        xsubs = xsubs + delt*subsspeed ;

    elseif t<tfinal*3/4

        xsubs = xsubs - delt*subsspeed ;

    else

        xsubs = xsubs + delt*subsspeed ;

    end

    [xmesh,ymesh] = meshgrid(xsubs,ysubs) ;
    flux = (interp2(x,y,fluxdist,xmesh,ymesh,'spline'));
    tflux = tflux + flux/delt ;

    emitted = emitted + parameter(3)*parameter(4)*4*delt ;
    deposited = deposited+flux*(delxs*delxs)*delt ;

    %XSUBS = [XSUBS; xsubs] ;
end
%Results
totalfluxdeposited = sum(sum(deposited)) ;
targetusage =(sum(sum(deposited))/emitted*100) ;
thicknessuniformity = std2(deposited)/mean2(deposited)*100 ;

tm = toc;
% Figure 1
% Ploting The Static Flux Distribution
subplot(2,2,1);
surf(x,y,fluxdist);
colorbar;
title('Static Flux Distribution');
xlabel ('x(mm)');
ylabel('y(mm)');

% Figure 2;
```

```
subplot(2,2,3);
surf(xmesh,ymesh,tflux);
colorbar;
xlabel ('xmesh');
ylabel ('ymesh');
title ('Dynamic Flux Distribution');

%Figure 3
%subplot(2,2,3);
%plot(XSUBS,'.');
%title ('Substrate Movement');
%ylabel('xsubs');
%xlabel('t(s)');

%Information
subplot(2,2,4);
axis 'off' ;
cla;
%msg = ['CPU time: ' num2str(tm,'%20.0f') 's' ];
%text(0,1,msg);

%Information
subplot(2,2,2);
axis 'off' ;
cla;
msg = ['Total flux emitted: ' num2str(emitted,'%20.0f')];
text(0,1,msg)
msg = ['Total film deposited: '
num2str(sum(sum(deposited)),'%20.0f')];
text(0,0.9,msg)
msg = ['Target usage (%): '
num2str(sum(sum(deposited))/emitted*100,'%20.1f')];
text(0,0.8,msg)
msg = ['Thickness uniformity (%): '
num2str(std2(deposited)/mean2(deposited)*100,'%20.1f')];
text(0,0.7,msg)
msg = ['Target is rectangular ' num2str(Lt*2,'%20.0f') ' by '
num2str(Wt*2,'%20.0f') ];
text(0,0.6,msg)
msg = ['Substrate velocity is ' num2str(subsspeed,'%20.2f')
'mm/s.'];
text(0,0.5,msg)
msg = ['Substrate mesh size is ' num2str(delxs,'%20.2f') ' mm.'];
text(0,0.4,msg)
msg = ['Target to substrate distance is ' num2str(H,'%20.0f') '
mm.'];
text(0,0.3,msg)
msg = ['Movement limit is ' num2str(movement,'%20.0f') ' mm.'];
text(0,0.2,msg)
msg = ['Time step size is ' num2str(delt,'%20.2f') ' s.'];
text(0,0.1,msg)

pause(0.5);
```

```
time = clock;
hold all
flname = [date '~' num2str(time(4)) '-' num2str(time(5)) '-'
num2str(time(6), '%20.0f')] ;
text(0,0,flname)
save(flname)
saveas(gcf,flname,'jpg')
    end
end
```

A.1.2 Function Flux

```
function F = Flux(Lt,Wt,delxt,Ls,Ws,delxs,H,f)
%Function calculates the flux distribution based on cosine law
nt = [0 0 -1];
ns = [0 0 1];
da = delxt*delxt;
F = zeros(Ws*2/delxs +1,Ws*2/delxs +1);
j = 0;
for q = -Lt:delxt:Lt
    j = j+1;
    i = 0;
    for p = -Wt:delxt:Wt
        i = i+1;
        k = 0;
        for y = -Ls:delxs:Ls
            k = k + 1;
            n = 0;
               for x = -Ws:delxs:Ws
                n = n + 1;
                Pt = [p q H];
                Ps = [x y 0];
                v = Ps-Pt;
                F(k,n) = F(k,n) + ((f*dot(nt,v))*dot(-
ns,v)*da)./(pi*dot(v,v).^(2));
               end
        end
    end
end
end
```

A.2 Thermal Dynamic Model M-Files

A.2.1 Main Program

```
clc;
clear all;
```

```
close all;
%input parameters
Li=16; %dimension in x direction cm
Lj=16; %dimension in y direction cm
deli=1; % mesh size in x direction cm
delj=1; % mesh size in y direction
ni=Li/deli; %number of mesh in x direction
nj=Lj/delj; %number of mesh in y direction
delt=1; % in seconds
Tin=23.5+273.15 ;%K%
%q=1; %J/s delt=1s
cp=0.880; % J/g.K
r=3.9; %g/cm^3
l=0.05; % dimension in z direction-substrate thickness
%initializing temperature on nodes!
k=0 ;
T(1:ni,1:nj)=Tin ;
tc=0.3; %W/cm.K thermal conductivity
%initializing loop
k=1;
t(k)=0;
tic;
while t<240
for i=1:ni ;
    for j=1:nj ;
        q=qflux(i,j,k);
        %left
       if i==1 && j==1 ;
            T(i,j,k+1)=T(i,j,k)+(tc*((T(i+1,j,k)+T(i,j+1,k)-
2*T(i,j,k)))+q(i,j,k)/l)*delt/(deli*delj*r*cp);
        elseif i==1 && j<nj ;
         T(i,j,k+1)=T(i,j,k)+(tc*((T(i+1,j,k)+T(i,j+1,k)+T(i,j-1,k)-
3*T(i,j,k)))+q(i,j,k)/l)*delt/(deli*delj*r*cp);
        elseif i==1 && j==nj ,
             T(i,j,k+1)=T(i,j,k)+(tc*((T(i+1,j,k)+T(i,j-1,k)-
2*T(i,j,k)))+q(i,j,k)/l)*delt/(deli*delj*r*cp) ;
        %top
        elseif j==nj && i<ni ;
             T(i,j,k+1)=T(i,j,k)+(tc*((T(i+1,j,k)+T(i-1,j,k)+T(i,j-
1,k)-3*T(i,j,k)))+q(i,j,k)/l)*delt/(deli*delj*r*cp);
        elseif j==nj && i==ni;
            T(i,j,k+1)=T(i,j,k)+(tc*((T(i-1,j,k)+T(i,j-1,k)-
2*T(i,j,k)))+q(i,j,k)/l)*delt/(deli*delj*r*cp);
        elseif i==ni && j>1 ;
            T(i,j,k+1)=T(i,j,k)+(tc*((T(i-1,j,k)+T(i,j+1,k)+T(i,j-
1,k)-3*T(i,j,k)))+q(i,j,k)/l)*delt/(deli*delj*r*cp) ;
        %bottom
        elseif i==ni && j==1 ;
            T(i,j,k+1)=T(i,j,k)+(tc*((T(i-1,j,k)+T(i,j+1,k)-
2*T(i,j,k)))+q(i,j,k)/l)*delt/(deli*delj*r*cp) ;
        elseif j==1 && i>1;
            T(i,j,k+1)=T(i,j,k)+(tc*((T(i+1,j,k)+T(i-
1,j,k)+T(i,j+1,k)-3*T(i,j,k)))+q(i,j,k)/l)*delt/(deli*delj*r*cp);
        else
```

```
            T(i,j,k+1)=T(i,j,k)+(tc*((T(i+1,j,k)+T(i-
1,j,k)+T(i,j+1,k)+T(i,j-1,k)-
4*T(i,j,k)))+q(i,j,k)/l)*delt/(deli*delj*r*cp);
        end
     end
end

for p=1:nj
z(p,k) = (T(1,p,k)) ; %First row
end
zb(k)= T(1,1,k);
zc(k) = T(1,16,k);
t(k+1)=t(k)+delt;
k=k+1;
end
Temp(1:ni,1:nj)= T(1:ni,1:nj,k-1) ;
%Creating x direction position matrix
for i = 1:ni;
    x(i)= deli*(i-1) ;
end
%Creating y direction position matrix
for j = 1:nj;
    y(j)= delj*(j-1) ;
end

surf(y,x,Temp(:,:))
tm=toc;
```

A.2.2 Function qflux

```
function q = qflux(i,j,k)
q=zeros(250,250,250) ;
tinit=0;
if (k>=tinit+(j-1)*3 && k<=tinit+18+(j-1)*3);
            q(i,j,k)=-0.02 ;
elseif (k>tinit+18+(j-1)*3 && k<= tinit+57+(j-1)*3);
                q(i,j,k)=0.048;
elseif (k> tinit+57+(j-1)*3 && k<= 120+tinit);
                    q(i,j,k)=-0.02;
elseif (k> 120+tinit && k<= 183+tinit-(j-1)*3);
                        q(i,j,k)=-0.02;
elseif (k> 183+tinit-(j-1)*3 && k<= 222+tinit-(j-1)*3);
                            q(i,j,k)=0.048;
elseif (k> 222+tinit-(j-1)*3 && k<= 240+tinit-(j-1)*3) ;
                                q(i,j,k)=-0.02;
end
```

APPENDIX B OUTPUT OF ANSYS SIMULATIONS

B.1 Large Heater Result

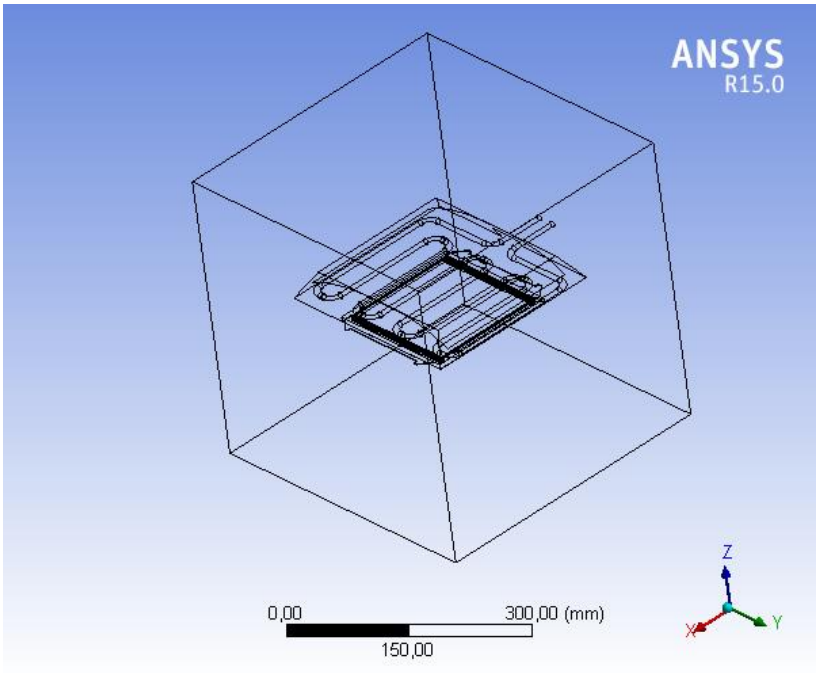

Contents

- **Units**
- **Model (N4)**
  - Geometry
    - Parts
  - Coordinate Systems
  - Connections
    - Contacts
      - Contact Regions
  - Mesh
    - Mapped Face Meshing
  - **Transient Thermal (N5)**
    - Initial Temperature
    - Analysis Settings
    - Loads
    - Solution (N6)
      - Solution Information
        - Result Charts
      - Results
      - Temperature Probe
- **Material Data**
  - Aluminum
  - Copper
  - Alumina 96%
  - Steel Stainless

Units

TABLE 1

Unit System	Metric (mm, kg, N, s, mV, mA) Degrees rad/s Celsius
Angle	Degrees
Rotational Velocity	rad/s
Temperature	Celsius

TABLE 2
Model (N4) > Geometry

Object Name	*Geometry*
State	Fully Defined
Definition	
Source	C:\Users\User\Desktop\ansys part2\ozge fea\fea v6\ozge_v6_files\dp0\Geom-2\DM\Geom-2.agdb
Type	DesignModeler
Length Unit	Meters
Element Control	Program Controlled
Display Style	Body Color
Bounding Box	
Length X	400, mm
Length Y	400, mm
Length Z	400, mm
Properties	
Volume	2,3647e+006 mm³
Mass	7,5098 kg
Scale Factor Value	1,
Statistics	
Bodies	11
Active Bodies	7
Nodes	30239
Elements	26096
Mesh Metric	None
Basic Geometry Options	
Parameters	Yes
Parameter Key	DS
Attributes	No
Named Selections	No
Material Properties	No
Advanced Geometry Options	
Use Associativity	Yes
Coordinate Systems	No
Reader Mode Saves Updated File	No
Use Instances	Yes
Smart CAD Update	No
Compare Parts On Update	No
Attach File Via Temp File	Yes
Temporary Directory	C:\Users\User\AppData\Roaming\Ansys\v150
Analysis Type	3-D
Decompose Disjoint Geometry	Yes
Enclosure and Symmetry Processing	Yes

TABLE 3
Model (N4) > Geometry > Parts

Object Name	*Dummy holder*	*Coating*	*Substrate*	*Support*	*Frame*	*Dummy heater*	*Reflector*	*Parabolic reflector*	*Dummy mass*	*Heater*	*Chamber*
State	Suppressed		Meshed			Suppressed	Meshed		Suppressed	Meshed	
Graphics Properties											
Visible	No		Yes			No	Yes		No	Yes	
Transparency			1				1			1	
Definition											
Suppressed	Yes		No			Yes	No		Yes	No	
Stiffness Behavior	Flexible										
Coordinate System	Default Coordinate System										
Reference Temperature	By Environment										
Thickness		0,5 mm					1, mm			4, mm	2, mm
Thickness Mode		Manual					Manual			Manual	
Offset Type		Middle					Middle			Top	Middle
Material											
Assignment	Aluminum	Copper	Alumina 96%	Aluminum		Steel Stainless	Aluminum			Steel Stainless	Aluminum
Nonlinear Effects	Yes										
Thermal Strain Effects	Yes										
Bounding Box											
Length X	155, mm	152,4 mm		158, mm	212, mm	284,3 mm	248, mm	200, mm	300, mm	284,3 mm	400, mm
Length Y	155, mm	152,4 mm		156, mm	174, mm	254,6 mm	260, mm	240, mm	300, mm	254,6 mm	400, mm
Length Z	20, mm	0, mm	0,5 mm	2,24 mm	7,6 mm	8,6 mm	35, mm	22,026 mm	1, mm	8,6 mm	400, mm
Properties											
Volume	4,805e+005 mm³	11613 mm³		43583 mm³	47599 mm³	1,1401e+005 mm³	80473 mm³	49315 mm³	90000 mm³	2,1211e+005 mm³	1,92e+006 mm³
Mass	1,2921 kg	0,10374 kg	4,4129e-002 kg	0,1172 kg	0,12799 kg	0,91835 kg	0,21639 kg	0,13261 kg	0,24201 kg	1,7086 kg	5,1629 kg
Centroid X	-9,4017e-015 mm	0, mm	-4,8626e-014 mm	1,073e-014 mm	0, mm	-12,791 mm	1,412 mm	-9,3473e-015 mm	1,0039e-013 mm	-12,783 mm	1,807e-015 mm
Centroid Y	-1,1752e-014 mm	0, mm	4,8626e-014 mm	2,652e-014 mm	-1,3346e-014 mm	-3,4447e-003 mm	1,8862e-014 mm	-0,86607 mm	-1,0039e-013 mm	-1,0336e-003 mm	0, mm
Centroid Z	-43,94 mm	-29,5 mm	-29,75 mm	-30,852 mm	-32,28 mm	-5,3169e-004 mm	26,516 mm	28,571 mm	-54,44 mm	-3,9485e-004 mm	-15, mm
Moment of Inertia Ip1	2629,9 kg·mm²	200,78 kg·mm²	85,411 kg·mm²	240,52 kg·mm²	508,7 kg·mm²	5429,2 kg·mm²	1426,5 kg·mm²	659,06 kg·mm²	1815,1 kg·mm²	10159 kg·mm²	2,2946e+005 kg·mm²
Moment of Inertia Ip2	2629,9 kg·mm²	200,78 kg·mm²	85,411 kg·mm²	248,29 kg·mm²	696,17 kg·mm²	4785,8 kg·mm²	1271, kg·mm²	447,37 kg·mm²	1815,1 kg·mm²	8961,1 kg·mm²	2,2946e+005 kg·mm²
Moment of Inertia Ip3	5173,6 kg·mm²	401,57 kg·mm²	170,82 kg·mm²	488,74 kg·mm²	1203,7 kg·mm²	10207 kg·mm²	2641,9 kg·mm²	1095,4 kg·mm²	3630,2 kg·mm²	19089 kg·mm²	2,2946e+005 kg·mm²
Surface Area(approx.)		23226 mm²					80473 mm²	49315 mm²		53028 mm²	9,6e+005 mm²
Statistics											
Nodes	0		1728	3705	3812	0	994	500	0	10367	9133
Elements	0		225	1780	1794	0	1892	912	0	10361	9132
Mesh Metric	None										

TABLE 4
Model (N4) > Coordinate Systems > Coordinate System

Object Name	*Global Coordinate System*
State	Fully Defined
Definition	
Type	Cartesian
Coordinate System ID	0,
Origin	
Origin X	0, mm
Origin Y	0, mm
Origin Z	0, mm
Directional Vectors	
X Axis Data	[1, 0, 0,]
Y Axis Data	[0, 1, 0,]
Z Axis Data	[0, 0, 1,]

TABLE 5
Model (N4) > Connections

Object Name	*Connections*
State	Fully Defined
Auto Detection	
Generate Automatic Connection On Refresh	Yes
Transparency	
Enabled	Yes

TABLE 6
Model (N4) > Connections > Contacts

Object Name	*Contacts*
State	Fully Defined
Definition	
Connection Type	Contact
Scope	
Scoping Method	Geometry Selection
Geometry	All Bodies
Auto Detection	
Tolerance Type	Slider
Tolerance Slider	0,
Tolerance Value	1,7321 mm
Use Range	No
Face/Face	Yes
Face/Edge	No
Edge/Edge	No
Priority	Include All
Group By	Bodies
Search Across	Bodies

TABLE 7
Model (N4) > Connections > Contacts > Contact Regions

Object Name	*No Separation - Substrate To Support*	*No Separation - Support To Frame*	*No Separation - Reflector To heater-surface*	*No Separation - Reflector To Parabolic reflector*
State	Fully Defined			
Scope				
Scoping Method	Geometry Selection			
Contact	5 Faces		2 Faces	1 Face
Target	5 Faces	6 Faces		1 Face
Contact Bodies	Substrate	Support	Reflector	
Target Bodies	Support	Frame	Heater	Parabolic reflector
Contact Shell Face			Program Controlled	
Target Shell Face			Program Controlled	
Shell Thickness Effect			No	
Definition				
Type	No Separation			
Scope Mode	Automatic			
Behavior	Program Controlled			
Trim Contact	Program Controlled			
Trim Tolerance	1,7321 mm			
Suppressed	No			
Advanced				
Formulation	Program Controlled			
Detection Method	Program Controlled			
Thermal Conductance	Program Controlled			
Pinball Region	Program Controlled			
Geometric Modification				
Contact Geometry Correction	None			

TABLE 8
Model (N4) > Mesh

Object Name	*Mesh*
State	Solved
Defaults	
Physics Preference	Mechanical
Relevance	0
Sizing	
Use Advanced Size Function	On: Curvature
Relevance Center	Coarse
Initial Size Seed	Active Assembly
Smoothing	Medium
Transition	Fast
Span Angle Center	Coarse
Curvature Normal Angle	Default (30,0 °)
Min Size	Default (2,06510 mm)
Max Face Size	Default (10,3260 mm)
Max Size	Default (10,3260 mm)
Growth Rate	Default
Minimum Edge Length	0,50 mm
Inflation	
Use Automatic Inflation	None
Inflation Option	Smooth Transition
Transition Ratio	0,272
Maximum Layers	5
Growth Rate	1,2
Inflation Algorithm	Pre
View Advanced Options	No
Patch Conforming Options	
Triangle Surface Mesher	Program Controlled
Patch Independent Options	
Topology Checking	Yes
Advanced	
Number of CPUs for Parallel Part Meshing	Program Controlled
Shape Checking	Standard Mechanical
Element Midside Nodes	Program Controlled
Straight Sided Elements	No
Number of Retries	Default (4)
Extra Retries For Assembly	Yes
Rigid Body Behavior	Dimensionally Reduced
Mesh Morphing	Disabled
Defeaturing	
Pinch Tolerance	Default (1,85860 mm)
Generate Pinch on Refresh	No
Sheet Loop Removal	No
Automatic Mesh Based Defeaturing	On
Defeaturing Tolerance	Default (1,54880 mm)
Statistics	
Nodes	30239
Elements	26096
Mesh Metric	None

TABLE 9
Model (N4) > Mesh > Mesh Controls

Object Name	*Mapped Face Meshing*
State	Fully Defined
Scope	
Scoping Method	Geometry Selection
Geometry	62 Faces
Definition	
Suppressed	No
Constrain Boundary	No
Advanced	
Specified Sides	No Selection
Specified Corners	No Selection
Specified Ends	No Selection

TABLE 10
Model (N4) > Analysis

Object Name	*Transient Thermal (N5)*
State	Solved
Definition	
Physics Type	Thermal
Analysis Type	Transient
Solver Target	Mechanical APDL
Options	
Generate Input Only	No

TABLE 11
Model (N4) > Transient Thermal (N5) > Initial Condition

Object Name	*Initial Temperature*
State	Fully Defined
Definition	
Initial Temperature	Uniform Temperature
Initial Temperature Value	24, °C

TABLE 12
Model (N4) > Transient Thermal (N5) > Analysis Settings

Object Name	*Analysis Settings*
State	Fully Defined
Step Controls	
Number Of Steps	1,
Current Step Number	1,
Step End Time	6000, s
Auto Time Stepping	Program Controlled
Initial Time Step	60, s
Minimum Time Step	6, s
Maximum Time Step	600, s
Time Integration	On
Solver Controls	
Solver Type	Program Controlled
Radiosity Controls	
Radiosity Solver	Program Controlled
Flux Convergence	1,e-004
Maximum Iteration	1000,
Solver Tolerance	1,e-007 W/mm²
Over Relaxation	0,1
Hemicube Resolution	10,
Nonlinear Controls	
Heat Convergence	Program Controlled
Temperature Convergence	Program Controlled
Line Search	Program Controlled
Nonlinear Formulation	Program Controlled
Output Controls	
Calculate Thermal Flux	Yes
General Miscellaneous	No
Store Results At	All Time Points
Analysis Data Management	
Solver Files Directory	C:\Users\User\Desktop\ansys part2\ozge fea\fea v6\ozge_v6_files\dp0\SYS-16\MECH\
Future Analysis	None
Scratch Solver Files Directory	
Save MAPDL db	No
Delete Unneeded Files	Yes
Nonlinear Solution	Yes
Solver Units	Active System
Solver Unit System	nmm

TABLE 13
Model (N4) > Transient Thermal (N5) > Loads

Object Name	*Radiation Heater*	*Radiation Substrate*	*Radiation Parabolic Reflector*	*Radiation Reflector*	*Temperature*	*Radiation Frame*	*Radiation Wall*
State	Fully Defined						
Scope							
Scoping Method	Geometry Selection						
Geometry	74 Faces	1 Face		5 Faces	1 Body	4 Faces	6 Faces
Shell Face	Both		Bottom	Top			Bottom
Apply To					Entire Body		
Definition							
Type	Radiation				Temperature	Radiation	
Correlation	Surface to Surface					Surface to Surface	
Emissivity	0,4 (step applied)	0,9 (step applied)	0,1 (step applied)			0,1 (step applied)	
Ambient Temperature	24, °C (step applied)					24, °C (step applied)	
Enclosure	1,					1,	
Enclosure Type	Open					Open	
Suppressed	No						
Magnitude					= -7,2206429*10^-13*time^4 + 6,851077*10^-9*time^3 - 1,369867*10^-5*time^2 + 0,031465369*time + 23		
Function							
Unit System	Metric (mm, kg, N, s, mV, mA) Degrees rad/s Celsius						
Angular Measure	Degrees						
Graph Controls							
Number Of Segments	200,						

TABLE 15
Model (N4) > Transient Thermal (N5) > Solution (N6) > Solution Information

Object Name	*Solution Information*
State	Solved
Solution Information	
Solution Output	Solver Output
Update Interval	2,5 s
Display Points	All
FE Connection Visibility	
Activate Visibility	Yes
Display	All FE Connectors
Draw Connections Attached To	All Nodes
Line Color	Connection Type
Visible on Results	No
Line Thickness	Single
Display Type	Lines

TABLE 16
Model (N4) > Transient Thermal (N5) > Solution (N6) > Solution Information > Result Charts

Object Name	*Temperature - Global Maximum*	*Temperature - Global Minimum*
State	Solved	
Definition		
Type	Temperature	
Suppressed	No	
Scope		
Scoping Method	Global Maximum	Global Minimum
Results		
Minimum	24,869 °C	23,996 °C
Maximum	264,66 °C	85,659 °C

TABLE 17
Model (N4) > Transient Thermal (N5) > Solution (N6) > Results

Object Name	*Temperature*	*Temperature 2*	*Temperature 3*	*Temperature 4*
State	Solved			
Scope				
Scoping Method	Geometry Selection			
Geometry	1 Body	All Bodies	1 Body	1 Face
Definition				
Type	Temperature			
By	Time			
Display Time	Last			
Calculate Time History	Yes			
Identifier				
Suppressed	No			
Results				
Minimum	192,61 °C	85,659 °C	249,13 °C	247,78 °C
Maximum	193,75 °C	263,11 °C		250,04 °C
Minimum Occurs On		Chamber		
Maximum Occurs On		Reflector		
Minimum Value Over Time				
Minimum	23,999 °C	23,996 °C	24,135 °C	24,099 °C
Maximum	192,61 °C	85,659 °C	249,13 °C	247,78 °C
Maximum Value Over Time				
Minimum	24, °C	24,869 °C		24,166 °C
Maximum	193,75 °C	264,66 °C		250,04 °C
Information				
Time	6000, s			
Load Step	1			
Substep	14			
Iteration Number	98			

Model (N4) > Transient Thermal (N5) > Solution (N6) > Temperature

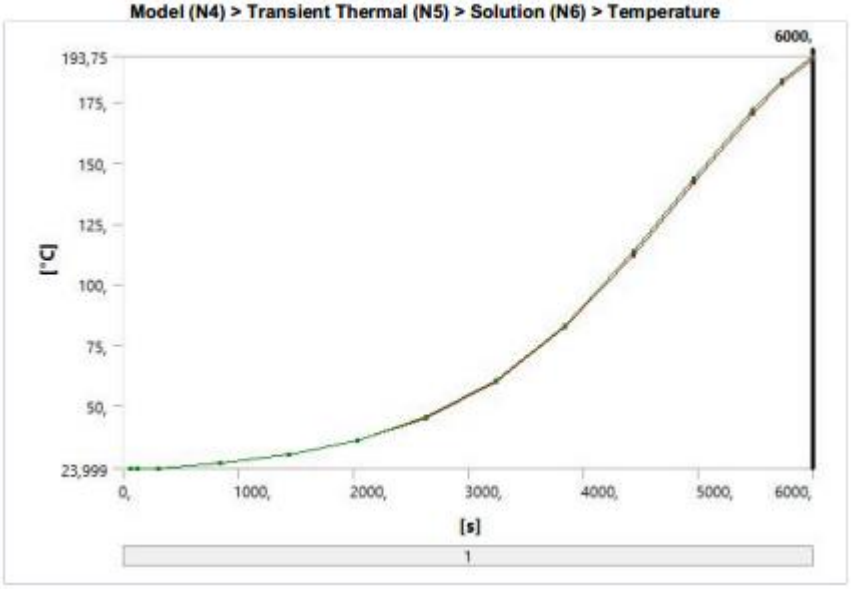

Material Data

TABLE 24
Aluminum > Constants

Thermal Conductivity	0,2375 W mm^-1 C^-1
Density	2,689e-006 kg mm^-3
Specific Heat	9,51e+005 mJ kg^-1 C^-1

TABLE 25
Copper > Constants

Thermal Conductivity	0,4 W mm^-1 C^-1
Density	8,933e-006 kg mm^-3
Specific Heat	3,85e+005 mJ kg^-1 C^-1

TABLE 26
Alumina 96% > Constants

Thermal Conductivity	2,5e-002 W mm^-1 C^-1
Density	3,8e-006 kg mm^-3
Specific Heat	8,8e+005 mJ kg^-1 C^-1

TABLE 27
Steel Stainless > Constants

Thermal Conductivity	1,38e-002 W mm^-1 C^-1
Density	8,055e-006 kg mm^-3
Specific Heat	4,8e+005 mJ kg^-1 C^-1

B.2 Small Heater Results

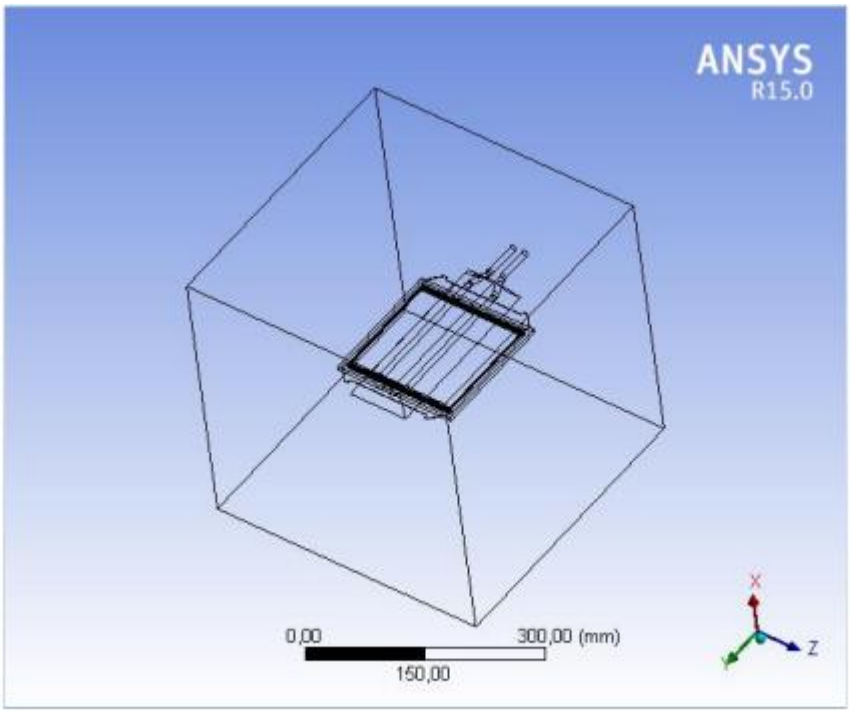

Contents

- Units
- Model (U4)
  - Geometry
    - Parts
  - Coordinate Systems
  - Connections
    - Contacts
      - Contact Regions
  - Mesh
    - Mapped Face Meshing
  - Named Selections
  - Transient Thermal (U5)
    - Initial Temperature
    - Analysis Settings
    - Loads
    - Solution (U6)
      - Solution Information
        - Result Charts
      - Results
- Material Data
  - Steel Stainless
  - Aluminum
  - Copper
  - Alumina 96%

Units

TABLE 1

Unit System	Metric (mm, kg, N, s, mV, mA) Degrees rad/s Celsius
Angle	Degrees
Rotational Velocity	rad/s
Temperature	Celsius

TABLE 2
Model (U4) > Geometry

Object Name	*Geometry*
State	Fully Defined
Definition	
Source	C:\Users\User\Desktop\ansys part2\ozge fea\fea v6\ozge_v6_files\dp0\Geom-1\DM\Geom-1.agdb
Type	DesignModeler
Length Unit	Meters
Element Control	Program Controlled
Display Style	Body Color
Bounding Box	
Length X	400, mm
Length Y	400, mm
Length Z	400, mm
Properties	
Volume	2,1177e+006 mm³
Mass	16,353 kg
Scale Factor Value	1,
Statistics	
Bodies	9
Active Bodies	6
Nodes	16994
Elements	15564
Mesh Metric	None
Basic Geometry Options	
Parameters	Yes
Parameter Key	DS
Attributes	No
Named Selections	No
Material Properties	No
Advanced Geometry Options	
Use Associativity	Yes
Coordinate Systems	No
Reader Mode Saves Updated File	No
Use Instances	Yes
Smart CAD Update	No
Compare Parts On Update	No
Attach File Via Temp File	Yes
Temporary Directory	C:\Users\User\AppData\Roaming\Ansys\v150
Analysis Type	3-D
Decompose Disjoint Geometry	Yes
Enclosure and Symmetry Processing	Yes

TABLE 3
Model (U4) > Geometry > Parts

Object Name	*Dummy Heater*	*Reflector*	*Dummy Holder*	*Coating*	*Substrate*	*Support*	*Frame*	*Heater*	*Chamber*
State	Suppressed	Meshed	Suppressed		Meshed				
Graphics Properties									
Visible	No	Yes	No		Yes				
Transparency		1			1				
Definition									
Suppressed	Yes	No	Yes		No				
Stiffness Behavior	Flexible								
Coordinate System	Default Coordinate System								
Reference Temperature	By Environment								
Thickness		1, mm		5,e-004 mm				4, mm	2, mm
Thickness Mode		Manual		Manual				Manual	
Offset Type		Middle		Bottom				Top	Middle
Material									
Assignment	Steel Stainless	Aluminum		Copper	Alumina 96%	Aluminum		Steel Stainless	
Nonlinear Effects	Yes								
Thermal Strain Effects	Yes								
Bounding Box									
Length X	8,6 mm	35, mm	20, mm	0, mm	0,5 mm	2,24 mm	7,6 mm	8,6 mm	400, mm
Length Y	284,3 mm	245, mm	155, mm	152,4 mm		158, mm	212, mm	284,3 mm	400, mm
Length Z	48,91 mm	85, mm	155, mm	152,4 mm		156, mm	174, mm	48,91 mm	400, mm
Properties									
Volume	34350 mm³	31041 mm³	4,805e+005 mm³	11,613 mm³	11613 mm³	43583 mm³	47599 mm³	63907 mm³	1,92e+006 mm³
Mass	0,27669 kg	8,347e-002 kg	1,2921 kg	1,0374e-004 kg	4,4129e-002 kg	0,1172 kg	0,12799 kg	0,51477 kg	15,466 kg
Centroid X	-4,0459e-004 mm	10,772 mm	-28,94 mm	-29,5 mm	-14,75 mm	-15,852 mm	-17,28 mm	-2,6356e-004 mm	-15, mm
Centroid Y	-54,089 mm	-16,533 mm	-20, mm	-9,3362e-015 mm	-20, mm			-54,054 mm	-9,035e-015 mm
Centroid Z	-538,36 mm								-540, mm
Moment of Inertia Ip1	2036,8 kg·mm²	492,04 kg·mm²	5173,6 kg·mm²	0,40157 kg·mm²	170,82 kg·mm²	488,74 kg·mm²	1203,7 kg·mm²	3809, kg·mm²	6,8736e+005 kg·mm²
Moment of Inertia Ip2	88,29 kg·mm²	71,492 kg·mm²	2629,9 kg·mm²	0,20078 kg·mm²	85,412 kg·mm²	240,52 kg·mm²	508,7 kg·mm²	169,75 kg·mm²	6,8736e+005 kg·mm²
Moment of Inertia Ip3	1951,1 kg·mm²	443,67 kg·mm²	2629,9 kg·mm²	0,20078 kg·mm²	85,412 kg·mm²	248,29 kg·mm²	696,17 kg·mm²	3648,7 kg·mm²	6,8736e+005 kg·mm²
Surface Area(approx.)		31041 mm²		23226 mm²				15977 mm²	9,6e+005 mm²
Statistics									
Nodes	0	310	0		1316	2927	3169	2736	6536
Elements	0	566	0		169	1404	1443	5448	6534
Mesh Metric	None								

TABLE 4
Model (U4) > Coordinate Systems > Coordinate System

Object Name	*Global Coordinate System*
State	Fully Defined
Definition	
Type	Cartesian
Coordinate System ID	0,
Origin	
Origin X	0, mm
Origin Y	0, mm
Origin Z	0, mm
Directional Vectors	
X Axis Data	[1, 0, 0,]
Y Axis Data	[0, 1, 0,]
Z Axis Data	[0, 0, 1,]

TABLE 5
Model (U4) > Connections

Object Name	*Connections*
State	Fully Defined
Auto Detection	
Generate Automatic Connection On Refresh	Yes
Transparency	
Enabled	Yes

TABLE 6
Model (U4) > Connections > Contacts

Object Name	*Contacts*
State	Fully Defined
Definition	
Connection Type	Contact
Scope	
Scoping Method	Geometry Selection
Geometry	All Bodies
Auto Detection	
Tolerance Type	Slider
Tolerance Slider	0,
Tolerance Value	1,7321 mm
Use Range	No
Face/Face	Yes
Face/Edge	No
Edge/Edge	No
Priority	Include All
Group By	Bodies
Search Across	Bodies

TABLE 7
Model (U4) > Connections > Contacts > Contact Regions

Object Name	*No Separation - Substrate To Support*	*No Separation - Support To Frame*	*Bonded - Heater Surface To box*
State	Fully Defined		
Scope			
Scoping Method	Geometry Selection		
Contact	5 Faces		4 Edges
Target	5 Faces	6 Faces	1 Face
Contact Bodies	Substrate	Support	Heater Surface
Target Bodies	Support	Frame	box
Target Shell Face			Program Controlled
Shell Thickness Effect			No
Definition			
Type	No Separation		Bonded
Scope Mode	Automatic		Manual
Behavior	Program Controlled		
Trim Contact	Program Controlled		
Trim Tolerance	1,7321 mm		
Suppressed	No		
Advanced			
Formulation	Program Controlled		
Detection Method	Program Controlled		
Thermal Conductance	Program Controlled		
Pinball Region	Program Controlled		
Elastic Slip Tolerance			Program Controlled
Geometric Modification			
Contact Geometry Correction	None		

TABLE 8
Model (U4) > Mesh

Object Name	*Mesh*
State	Solved
Defaults	
Physics Preference	Mechanical
Relevance	0
Sizing	
Use Advanced Size Function	On: Curvature
Relevance Center	Coarse
Initial Size Seed	Active Assembly
Smoothing	Medium
Transition	Fast
Span Angle Center	Coarse
Curvature Normal Angle	Default (30,0 °)
Min Size	Default (2,43770 mm)
Max Face Size	Default (12,1880 mm)
Max Size	Default (12,1880 mm)
Growth Rate	Default
Minimum Edge Length	0,50 mm
Inflation	
Use Automatic Inflation	None
Inflation Option	Smooth Transition
Transition Ratio	0,272
Maximum Layers	5
Growth Rate	1,2
Inflation Algorithm	Pre
View Advanced Options	No
Patch Conforming Options	
Triangle Surface Mesher	Program Controlled
Patch Independent Options	
Topology Checking	Yes
Advanced	
Number of CPUs for Parallel Part Meshing	Program Controlled
Shape Checking	Standard Mechanical
Element Midside Nodes	Program Controlled
Straight Sided Elements	No
Number of Retries	Default (4)
Extra Retries For Assembly	Yes
Rigid Body Behavior	Dimensionally Reduced
Mesh Morphing	Disabled
Defeaturing	
Pinch Tolerance	Default (2,19390 mm)
Generate Pinch on Refresh	No
Sheet Loop Removal	No
Automatic Mesh Based Defeaturing	On
Defeaturing Tolerance	Default (1,82830 mm)
Statistics	
Nodes	16994
Elements	15564
Mesh Metric	None

TABLE 9
Model (U4) > Mesh > Mesh Controls

Object Name	*Mapped Face Meshing*
State	Fully Defined
Scope	
Scoping Method	Geometry Selection
Geometry	87 Faces
Definition	
Suppressed	No
Constrain Boundary	No
Advanced	
Specified Sides	No Selection
Specified Corners	No Selection
Specified Ends	No Selection

TABLE 10
Model (U4) > Named Selections > Named Selections

Object Name	*Radiation Heater*
State	Suppressed
Scope	
Scoping Method	Geometry Selection
Geometry	No Selection
Definition	
Send to Solver	Yes
Visible	Yes
Program Controlled Inflation	Exclude
Statistics	
Type	Manual
Total Selection	No Selection
Suppressed	0
Used by Mesh Worksheet	No

TABLE 11
Model (U4) > Analysis

Object Name	*Transient Thermal (U5)*
State	Solved
Definition	
Physics Type	Thermal
Analysis Type	Transient
Solver Target	Mechanical APDL
Options	
Generate Input Only	No

TABLE 12
Model (U4) > Transient Thermal (U5) > Initial Condition

Object Name	*Initial Temperature*
State	Fully Defined
Definition	
Initial Temperature	Uniform Temperature
Initial Temperature Value	24, °C

TABLE 13
Model (U4) > Transient Thermal (U5) > Analysis Settings

Object Name	*Analysis Settings*
State	Fully Defined
Step Controls	
Number Of Steps	1,
Current Step Number	1,
Step End Time	5600, s
Auto Time Stepping	Program Controlled
Initial Time Step	56, s
Minimum Time Step	5,6 s
Maximum Time Step	560, s
Time Integration	On
Solver Controls	
Solver Type	Program Controlled
Radiosity Controls	
Radiosity Solver	Program Controlled
Flux Convergence	1,e-004
Maximum Iteration	1000,
Solver Tolerance	1,e-007 W/mm²
Over Relaxation	0,1
Hemicube Resolution	10,
Nonlinear Controls	
Heat Convergence	Program Controlled
Temperature Convergence	Program Controlled
Line Search	Program Controlled
Nonlinear Formulation	Program Controlled
Output Controls	
Calculate Thermal Flux	Yes
General Miscellaneous	No
Store Results At	All Time Points
Analysis Data Management	
Solver Files Directory	C:\Users\User\Desktop\ansys part2\ozge fea\fea v6\ozge_v6_files\dp0\SYS-1\MECH\
Future Analysis	None
Scratch Solver Files Directory	
Save MAPDL db	No
Delete Unneeded Files	Yes
Nonlinear Solution	Yes
Solver Units	Active System
Solver Unit System	nmm

TABLE 14
Model (U4) > Transient Thermal (U5) > Loads

Object Name	*Radiation Heater*	*Radiation Substrate*	*Radiation Reflector*	*Temperature*	*Radiation Frame*	*Radiation Wall*
State	Fully Defined					
Scope						
Scoping Method	Geometry Selection					
Geometry	26 Faces	1 Face	5 Faces	1 Body	4 Faces	6 Faces
Shell Face	Both		Top			Bottom
Apply To				Entire Body		
Definition						
Type	Radiation			Temperature	Radiation	
Correlation	Surface to Surface				Surface to Surface	
Emissivity	0,5 (step applied)	0,9 (step applied)	0,1 (step applied)		0,1 (step applied)	
Ambient Temperature	24, °C (step applied)				24, °C (step applied)	
Enclosure	1,				1,	
Enclosure Type	Open				Open	
Suppressed	No					
Magnitude				= -1,735978*10^-9*time^3 + 1,1110292214*10^-5*time^2 + 0,038859*time + 24		
Function						
Unit System				Metric (mm, kg, N, s, mV, mA) Degrees rad/s Celsius		
Angular Measure				Degrees		
Graph Controls						
Number Of Segments				200,		

TABLE 15
Model (U4) > Transient Thermal (U5) > Solution

Object Name	*Solution (U6)*
State	Solved
Adaptive Mesh Refinement	
Max Refinement Loops	1,
Refinement Depth	2,
Information	
Status	Done

TABLE 16
Model (U4) > Transient Thermal (U5) > Solution (U6) > Solution Information

Object Name	*Solution Information*
State	Solved
Solution Information	
Solution Output	Solver Output
Update Interval	2,5 s
Display Points	All
FE Connection Visibility	
Activate Visibility	Yes
Display	All FE Connectors
Draw Connections Attached To	All Nodes
Line Color	Connection Type
Visible on Results	No
Line Thickness	Single
Display Type	Lines

TABLE 18
Model (U4) > Transient Thermal (U5) > Solution (U6) > Results

Object Name	*Temperature*	*Temperature 2*	*Temperature 3*	*Temperature 4*	*Temperature 5*	*Temperature 6*
State	Solved					
Scope						
Scoping Method	Geometry Selection					
Geometry	All Bodies	1 Face				All Bodies
Definition						
Type	Temperature					
By	Time					
Display Time	Last					
Calculate Time History	Yes					
Identifier						
Suppressed	No					
Results						
Minimum	49,712 °C	153,13 °C	140,35 °C	153,17 °C	153,13 °C	49,712 °C
Maximum	285,16 °C	155,34 °C	140,63 °C	154,06 °C	154,15 °C	285,16 °C
Minimum Occurs On	box					box
Maximum Occurs On	box					box
Minimum Value Over Time						
Minimum	23,998 °C	24,002 °C	24,009 °C	24,002 °C		23,998 °C
Maximum	49,712 °C	153,13 °C	140,35 °C	153,17 °C	153,13 °C	49,712 °C
Maximum Value Over Time						
Minimum	26,211 °C	24,008 °C	24,009 °C	24,005 °C		26,211 °C
Maximum	285,16 °C	155,34 °C	140,63 °C	154,06 °C	154,15 °C	285,16 °C
Information						
Time	5600, s					
Load Step	1					
Substep	16					
Iteration Number	54					

Model (U4) > Transient Thermal (U5) > Solution (U6) > Temperature 5

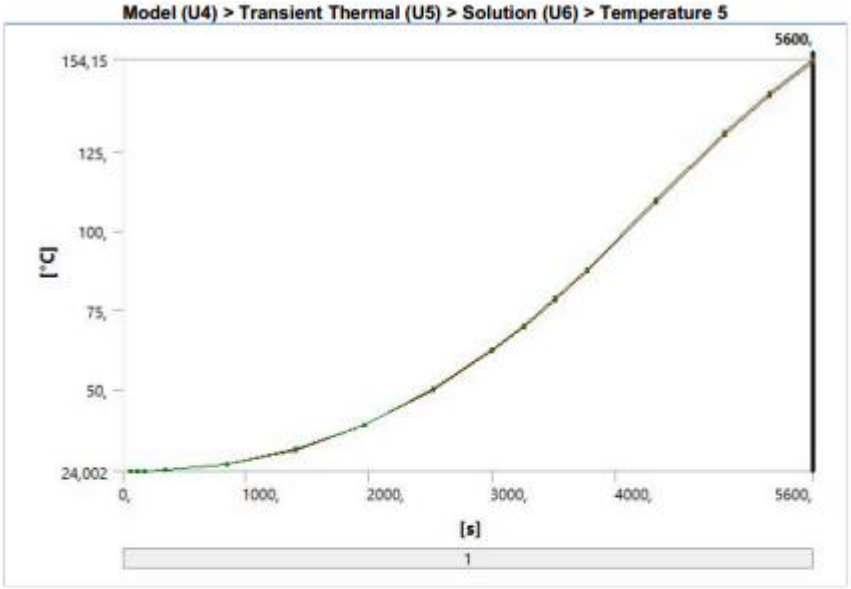

TABLE 23
Model (U4) > Transient Thermal (U5) > Solution (U6) > Temperature 5

Time [s]	Minimum [°C]	Maximum [°C]
56,	24,002	24,005
112,	24,02	24,025
168,	24,051	24,06
336,	24,274	24,292
840,	26,254	26,312
1400,	30,848	30,969
1960,	38,504	38,714
2520,	49,732	50,056
2993,9	62,253	62,697
3251,7	69,721	70,227
3509,5	78,149	78,733
3767,3	87,256	87,912
4327,3	108,93	109,73
4887,3	130,1	131,03
5243,7	142,47	143,46
5600,	153,13	154,15

Material Data

TABLE 24
Aluminum > Constants

Thermal Conductivity	0,2375 W mm^-1 C^-1
Density	2,689e-006 kg mm^-3
Specific Heat	9,51e+005 mJ kg^-1 C^-1

TABLE 25
Copper > Constants

Thermal Conductivity	0,4 W mm^-1 C^-1
Density	8,933e-006 kg mm^-3
Specific Heat	3,85e+005 mJ kg^-1 C^-1

TABLE 26
Alumina 96% > Constants

Thermal Conductivity	2,5e-002 W mm^-1 C^-1
Density	3,8e-006 kg mm^-3
Specific Heat	8,8e+005 mJ kg^-1 C^-1

TABLE 27
Steel Stainless > Constants

Thermal Conductivity	1,38e-002 W mm^-1 C^-1
Density	8,055e-006 kg mm^-3
Specific Heat	4,8e+005 mJ kg^-1 C^-1